Model-based image reconstruction in X-ray Computed Tomography

Wojciech Zbijewski

The work described in this thesis was carried out at Image Sciences Institute, Department of Nuclear Medicine and Rudolf Magnus Institute of Neuroscience, UMC Utrecht.

ISBN-10: 90-393-4264-4
ISBN-13: 978-90-393-4264-0

Printed by Wöhrman Print Service, Zutphen, The Netherlands

...For my Mom
In loving memory...

Model-based image reconstruction in X-ray Computed Tomography

Model gebaseerde beeldreconstructie in Röntgen computer-tomografie

(met een samenvatting in het Nederlands)

Proefschrift ter verkrijging van de graad van doctor
aan de Universiteit Utrecht
op gezag van de rector magnificus, prof. dr. W.H. Gispen,
ingevolge het besluit van het college voor promoties in het
openbaar te verdedigen
op maandag 19 juni 2006 des middags te 2.30 uur

door

Wojciech Bartosz Zbijewski

geboren op 10 december 1976
te Warschau, Polen

Promotor:

Prof. Dr. Ir. Max A. Viergever

Co-promotor:

Dr. Freek J. Beekman

This research was financially supported by the Dutch Technology Foundation STW (project UPG5544).

Contents

Chapter 1

Introduction

In this chapter, the physics of X-ray imaging will be briefly discussed. The principles of X-ray Computed Tomography (CT) will be outlined and the major image-degrading factors in X-ray CT will be explained. Both analytical and statistical image reconstruction algorithms applicable to X-ray CT will be reviewed and their advantages and disadvantages will be discussed. It will be explained how the effects of image degrading factors in X-ray CT can be reduced by means of statistical reconstruction methods. Finally, a brief outline of the thesis will be presented.

A wealth of literature exists on the subjects covered in this introduction. The author would like to direct readers interested in a more in-depth coverage of matters such as the design and evolution of CT scanners or theory of image reconstruction to books and review papers by J. Fessler (Fessler 2001), J. Hsieh (Hsieh 2003), W. Kalender (Kalender 2000), A. Kak and M. Slaney (Kak & Slaney 1988) and S. Webb (Webb 1990).

1.1 The basics of X-ray imaging

The term X-rays is typically used to denote the region of the electromagnetic spectrum located between approximately 10 nm and 0.01 nm and corresponding to photons having energies between approximately 124 eV and 124 keV. The wavelengths of X-rays commonly used in diagnostic imaging lie within a narrower range: from 0.1 nm (12.4 keV) to 0.01 nm (124 keV). X-rays are generated when a target substance is bombarded with high-speed charged particles. Electrons are commonly used for this task because of their high efficiency. When a fast electron interacts with the target medium, most of its energy is converted to heat through ionisation of the target atoms. Production of X-ray photons occurs through three other types of interactions: (i) rapid deceleration of electrons in the electric field of target nuclei, (ii) direct collisions of electrons with target nuclei and (iii) liberation of an inner-shell electron of one of the target-atoms by a high-speed electron; the hole left by the liberated electron is filled by an electron from an outer shell, which results in emission of an X-ray. Fig. 1.1 demonstrates a typical spectrum produced by X-ray tubes used in Computed Tomography. The continuous background of the spectrum is generated through the process (i) from the list presented above and is referred to as

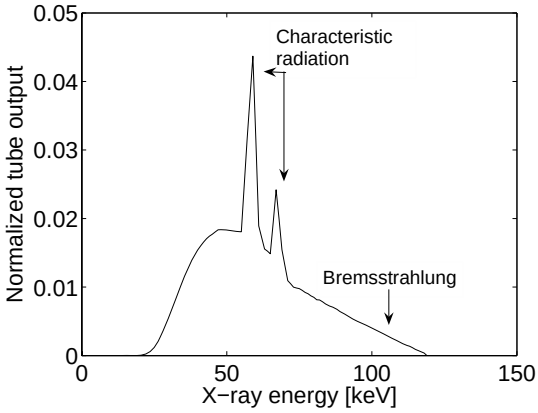

Figure 1.1: Energy spectrum of an X-ray tube with a tungsten anode. The tube voltage was 120 kVp, the beam was filtered through 7 mm of Al-equivalent material. Values of both parameters were based on those encountered in clinical CT scanners. Pre-filtering of the beam is used to reduce the contribution of low-energy X-rays. Such X-rays have no imaging capability, but would increase the patient exposure. The spectrum was obtained using the software provided in Siewardsen et al. (2004).

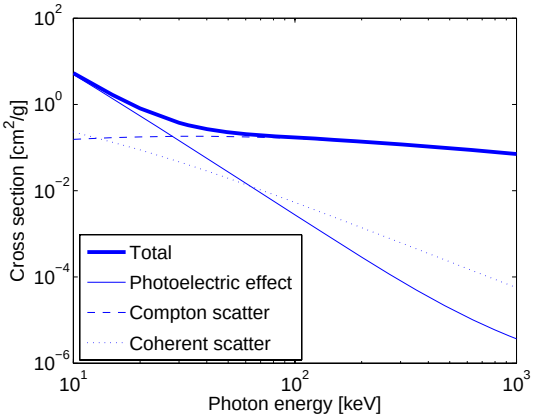

Figure 1.2: Cross-sections for various types of photon-matter interactions in water. The data for this plot was obtained from the XCOM database (Berger et al. 1999).

the bremsstrahlung radiation. An electron-nucleus collision can be treated as an extreme case of bremsstrahlung where all the electron's energy is emitted as X-rays. Such an interaction determines the upper energy limit of the spectrum. Finally, the fine peaks in the spectrum represent the so-called characteristic X-rays created as a result of the process (iii).

Fig. 1.2 displays cross-sections for various types of interactions that may occur between photons and water atoms. In the energy range covered by diagnostic X-rays, the most prominent interaction mechanisms are: (i) the photoelectric effect, in which an X-ray is absorbed while liberating an electron from an atom, (ii) Compton scattering, in which a photon is deflected and loses energy through a collision with an outer-shell atomic electron and (iii) coherent, or Rayleigh scattering, where a change of photon direction occurs without any energy loss. The combined effects of these three interactions is that some of the photons are removed from the beam, i.e. the X-ray radiation is attenuated as it passes through matter. Total attenuation caused by the photoelectric effect and scattering can be summarised in one, energy dependent **attenuation coefficient** $\mu(E)$. For an X-ray beam that has travelled through an attenuator along a line L, the transmitted intensity is given by the Lambert-Beer law:

$$I(E) = I_0(E)e^{-\int_L \mu(E;\vec{x})\mathrm{d}\ell} \tag{1.1}$$

where E is the beam energy, I_0 is the incident intensity, and $\mu(E;\vec{x})$ is the spatial distribution of the attenuation coefficient in the object. The quantity $\int_L \mu(E;x)\mathrm{d}\ell$ will be referred to as the **line integral** of the attenuation coefficient along line L. Biological tissues are **semi-opaque** to photons coming from the energy regions of diagnostic X-rays, i.e. X-ray beams are only partially absorbed by objects like the human body. The transmitted intensity is high enough to be recorded and the differences in the value of $\mu(E)$ between different tissues, especially between bone and soft-tissue, are high enough to yield a sufficient contrast in the detected images. Fig. 1.3 *a* shows a typical radiograph obtained when a broad beam of X-rays is transmitted through a human skull. There is no doubt that the discovery of X-rays by Röntgen and his first observations of their imaging capabilities in 1895 amounted to a revolution in medicine. For the first time in history, it became possible to look inside a living human body without the need to open it surgically. Revolutionary as it was, X-ray radiography has one obvious disadvantage: all the body structures traversed by the X-ray beam are superimposed in the resulting images. This reduces the visibility of the organs of interest, leading to poor low-contrast resolution. The next revolution in medical imaging, the development of Computed Tomography, came about as a response to this limitation of conventional radiography.

1.2 X-ray Computed Tomography

1.2.1 The concept of tomographic imaging. History of and current trends in X-ray Computed Tomography

In **tomography**, images of a selected **cross-section** taken through the object are generated. In the case of X-ray tomography, similarly to X-ray radiography, the quantity being imaged is the distribution of the attenuation coefficient $\mu(\vec{x})$ within the object of interest. In Fig. 1.3 *b*, a tomographic image of a slice through a human skull is shown. For an in-depth survey of the history of

(a) X-ray radiography (b) X-ray CT

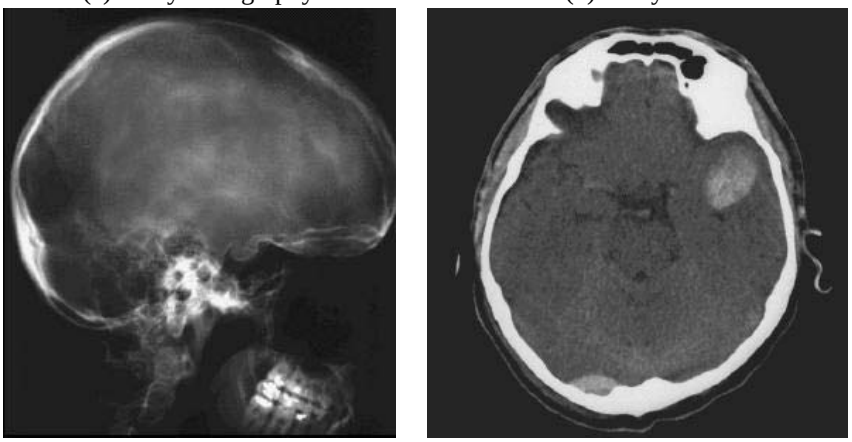

Figure 1.3: Comparison of a conventional radiograph of a skull (panel *a*) with a cross-sectional image of the same area obtained with X-ray Computed Tomography (panel *b*). Images courtesy of W. Kalender.

tomographic imaging, the reader is referred to the excellent book by Steve Webb (Webb 1990). Here, only a very brief summary of the most important developments will be presented.

The earliest systems allowing some sort of cross-sectional imaging date back to the early twenties of the 20th century. The basic concept employed in those early setups was to combine the movements of an X-ray source and detector in such a way that only the cross-section of interest would remain in focus throughout the whole acquisition. The other areas of the volume being imaged would appear blurred in the resulting radiograph. It is obvious that the performance of such a system is far from ideal, as the removal of the structures lying outside the plane of interest from the final image could never be complete. However, already in 1940, the first patent was granted to G. Frank in Hungary for a design very much resembling the more successful modern X-ray tomographs. A simple everyday life observation explains the idea behind current day tomography: one can infer a lot about the internal structure of a semi-opaque object by just looking at it from different angles. Similarly, in X-ray tomography numerous radiographic images of an object are collected from many locations around it, and a final cross-sectional image is **reconstructed** from these radiographs. The rotation of the X-ray source-detector pair is usually executed around the patient's long body axis and therefore the sectional images obtained represent **trans-axial slices** through the body. The radiographic images recorded at each angular location of the detector will be further referred to as **projection views**. One crucial problem emerges: how can one reconstruct the cross-sectional images from the projection views collected? In the early setups, analogue optical methods were used for this task. As will be explained later, the methodology employed was incorrect from a mathematical point of view and yielded significantly blurred images. Two developments were still needed in order to ascertain the widespread use of X-ray tomographic systems: derivation of mathematically correct reconstruction methods and the emergence of computers capable of handling huge amounts of projection and image data, thus facilitating high-resolution imaging. The design of the first truly successful medical X-ray **Computed Tomograph (CT)** is mainly ascribed to two

researchers: Allan M. Cormack and Godfrey N. Hounsfield. The former developed in 1956 a mathematical theory of image reconstruction. In 1963 and 1964 he published some experimental results obtained with a simple scanner. His results did not attract widespread attention due to prohibitive computation times required to perform the calculations necessary for the reconstruction. Surprisingly, while pursuing his research, Cormack remained unaware of earlier, purely mathematical work (Radon 1917) on the reconstruction of objects from their line integrals.

G. N. Hounsfield is credited with the development, in the period between 1967 and 1971, of a first clinical computer-based X-ray tomographic scanner. It is interesting to note that, similarly to Cormack who did not capitalise on Radon's work, Hounsfield was working completely independently from Cormack, using, for example, a different reconstruction method.

Further development of X-ray CT was spurred by two factors: one of them was the obvious need to improve image quality, which required amendments in X-ray sources and X-ray detectors, but also an increase in the number of projection views taken and number of samples recorded per view. Another important factor in the development of CT was the need to reduce the acquisition time required to generate the projection data. Fig. 1.4 summarises the

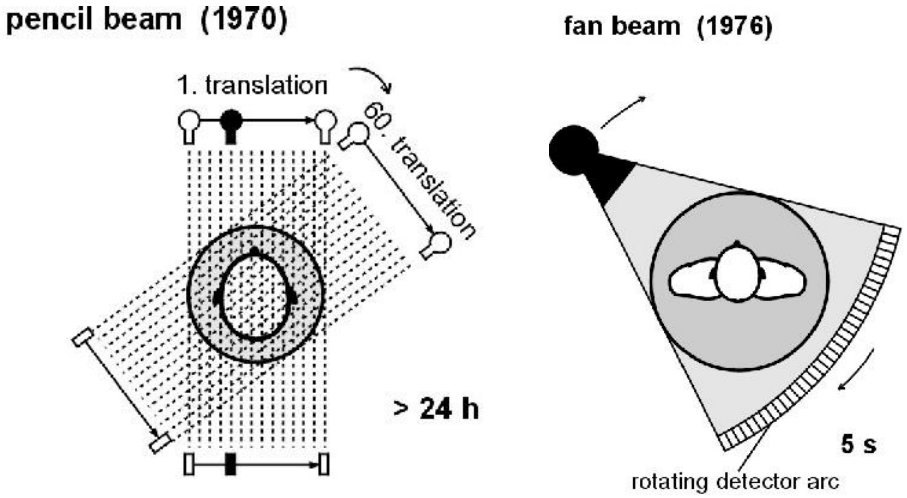

Figure 1.4: Left panel: the first clinical CT scanners were acquiring data in the so-called translate-rotate mode, which leads to long scanning times. Right panel: Most of the currently used X-ray CT scanners are based on this fan-beam design. The X-ray beam completely covers the region of interest, the detector is broad enough to collect a whole projection view during a single read-out. Helical acquisition is a further modification of this setup, where the patient is continously translated in the axial direction during the scan. Helical multi-slice scanners and cone-beam systems employ more than one row of detector cells. Images courtesy of W. Kalender.

early evolution of CT scanners. In first generation systems, each projection view was collected by scanning a pencil X-ray beam along the direction of the view. A single detector was used to record the transmitted intensity for each scanning point. The source-detector pair was then rotated to a new viewing angle and a new linear scanning process was commenced. This was very time-consuming: the total acquisition time in the earliest clinical CT scanners was approx-

imately 5 minutes for a single slice, which resulted in degradation of image quality induced by patient motion. Efforts undertaken to reduce the scanning time resulted in the introduction of the so-called fan-beam systems. In such scanners, an entire region of interest falls within a fan shaped beam of X-rays and the transmitted intensities of these X-rays are recorded by a large number of detector cells located at the base of the fan. The setup of a fan-beam scanner forms the basis for further developments that were targeted at providing capabilities for rapid, volumetric imaging. If the acquisition of more than one slice was desired, these fan-beam systems worked in the so-called step-and-shoot mode. Once the data acquisition for one slice was finished, the source-detector pair was stopped and the patient was translated along its long axis. Such inter-scan delays made it impossible to acquire a set of slices covering entire organs within a single breath-hold. A natural progression in the evolution of X-ray CT scanners, realised in late 1980s (Kalender et al. 1990, Crawford & King 1990), was to combine continuous patient translation in the axial direction with continuous circular movement of the source-detector pair. In such a **helical scanning mode**, the inter-scan delays are eliminated. This allows for complete organ coverage during a single breath-hold. Moreover, uniform sampling in the direction of the long body axis is ascertained, giving the ability to reconstruct images at any axial location. The next breakthrough in CT technology was achieved when helical scanning was combined with the use of detectors containing more than one row of detector elements. In a **multi-slice CT**, introduced around 1998 (Taguchi & Aradate 1998, Hu 1999), the data for multiple cross-sections is collected simultaneously at every projection view by a multi-row detector. Since the thickness of image slices depends now on the width of a single detector row and not on the width of the X-ray beam, wide X-ray beams can be used. This leads to better X-ray source utilisation and larger volume coverage. The latter allows to collect data for larger body areas in shorter time, reducing problems with issues such as the wash-out of imaging contrast agent during large area angiographic studies. The detectors used in helical multi-slice CT are usually based on blocks of solid-state scintillators, such as gadolinium-oxy-sulfide Gd_2O_2S, coupled with photodiodes that read out the light photons generated by the X-rays absorbed in the scintillators. Systems having up to 64 rows of detector cells, covering an axial range of approximately 40 mm are currently available (Platten et al. 2005).

The evolution of CT from simple, parallel-beam systems to multi-slice, helical scanners currently in use is marked by a tremendous decrease of the time required to acquire a single image slice. According to Hsieh (2003), the scan time per slice had been decreasing exponentially over the 30 years of X-ray CT development between 1970 and 2000; the scan time reduction factor per year was approximately 1.34.

With the advent of helical and multi-slice helical acquisition, X-ray CT became a truly volumetric imaging modality. What is reconstructed and later viewed by a radiologist are not single slices anymore, but whole volumes representing details of the anatomy. Volumetric data can now even be collected without translational patient motion. If the detector extent along the long patient axis is large enough, a single rotation of the source-detector pair without any patient translation may be sufficient to acquire data required for reconstructing an extended volume. One application area where such circular orbit **cone-beam** systems are used is so-called **micro-CT** imaging. In this modality, X-ray sources with extremely small focal spots are combined with two-dimensional, high-resolution scintillation detectors to enable almost microscopic, volumetric imaging of, for example, small laboratory rodents, biological and geological samples,

or electronic circuits. The SkyScan1076 scanner used in the research described in this thesis employs scintillation detectors coupled with CCD cameras and can achieve isotropic resolution down to 9 μm in-vivo.

In human applications, cone-beam scanning can be realised by means of a **C-arm** system. Such system consists of a two-dimensional, wide field-of-view X-ray detector mounted together with the source on a rotating C-shaped arm. C-arm scanners were constructed mainly for performing digital radiographic imaging during angiovascular interventions. Since they have the capability to rotate around the patient, many radiographs can be collected at different viewing angles and the data obtained can be tomographically reconstructed. In this way, three-dimensional images of human vasculature or other organs can be obtained. Such reconstructions may have great value in planning and guiding minimally invasive surgical procedures (Wiesent et al. 2000, Siewerdsen et al. 2005). C-arm systems equipped with flat-panel X-ray detectors are especially promising for this type of applications. Flat-panel detectors offer the capabilities for distortion-less, real-time imaging with isotropic, sub-mm resolution. Systems having field-of-view of approximately 20(trans-axial)x15(axial) cm are available (Bertram et al. 2005, Siewerdsen et al. 2005). Since the arc covered in rotational motion by a C-arm is usually shorter than the minimal requirement for complete object coverage and because the movement of the source-detector setup in a C-arm system is often irregular, extensive research is currently being pursued on the development of accurate reconstruction methods for C-arm tomography.

1.2.2 Image reconstruction in X-ray CT - analytical methods

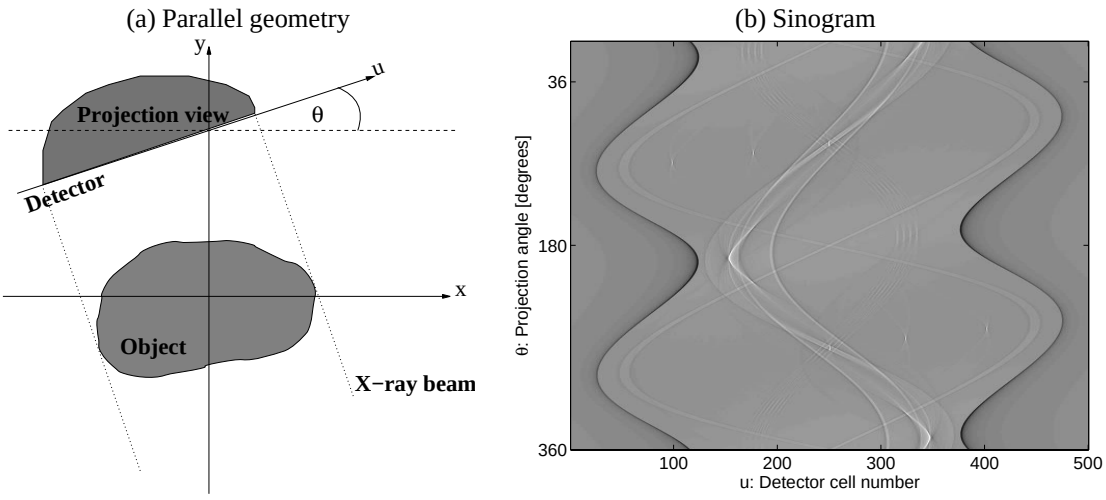

Figure 1.5: Left panel: object and its projection view obtained at angle θ in parallel beam geometry. Right panel: an example of a sinogram.

Let us reconsider the parallel-beam geometry of the first generation X-ray CT scanners. Fig. 1.5 *a* depicts such a configuration and defines all the relevant quantities. For a projection angle θ, the intensity of a mono-energetic X-ray beam measured at detector location u is given

by the Lambert-Beer law formulated in Eq. 1.1. Here we rewrite this equation by explicitly expressing the line integral in terms of spatial coordinates x, y and u:

$$I(u,\theta) = I_0(u,\theta)e^{\int_{-\infty}^{\infty}\int_{-\infty}^{\infty}\mu(x,y)\delta(x\cos(\theta)+y\sin(\theta)-u)\mathrm{d}x\,\mathrm{d}y} \tag{1.2}$$

where we dropped the energy variable E from the notation. By dividing the measured intensity $I(u,\theta)$ by the beam intensity at the entrance to the object $I_0(u,\theta)$ (the so-called **blank scan value**) and taking the negative logarithm of the result, one can extract the line integral value $P(u,\theta)$ from the measured X-ray projection data:

$$P(u,\theta) = -\log\frac{I(u,\theta)}{I_0(u,\theta)} \tag{1.3}$$

The set of line integrals $P(u,\theta)$ defines the **Radon transform** of the attenuation coefficient distribution $\mu(x,y)$. Analytical reconstruction methods are based on explicit formulas for inversion of Radon transforms. Before we proceed to show how such an inversion can be achieved in a parallel-beam configuration, one more term will be defined: **the sinogram**. This term denotes an image obtained by displaying the projection data in a coordinate system spanned by the projection angle θ on the vertical axis and the detector coordinate u on the horizontal axis. An example of a sinogram is shown in Fig. 1.5 *b*. It can easily be shown that a projection of a single point in image space follows a sinusoidal curve in the sinogram domain, hence the name. A naive approach to image reconstruction would be to take all the line integral data collected in a sinogram and simply "smear" them back over the image plane along the corresponding projection lines. Mathematically, in the parallel-beam geometry, the resulting image would be given by the following **back-projection** formula:

$$\mu_{BP}(x,y) = \int_0^{\pi} P(x\cos(\theta)+y\sin(\theta),\theta)\mathrm{d}\theta \tag{1.4}$$

The angular integration range in Eq. 1.4 has been limited to a half-circle, because, as can be readily seen, the projection data collected over the range $(\pi, 2\pi)$ is redundant with the data collected over the $(0,\pi)$ range. For an object consisting of a single point, simple back-projection of its projections results in a set of lines traversing through the image plane and crossing at the location of this point. One line is generated for each viewing angle θ. Such a situation is depicted in the left panel of Fig. 1.6. It is obvious that the resulting reconstruction will be significantly blurred. One can observe that the number of back-projection lines of a single point per unit of arc decreases as $1/r$, where r is the distance from the point. Hence the resulting blurring of the reconstructions obtained with simple back-projection is often referred to as $1/r$ blurring. The earliest tomographic devices described in the preceeding chapter, such as the one proposed by G. Frank, used analogue, optical implementations of precisely this simple back-projection algorithm. In order to achieve better image quality, one has to prevent the $1/r$ blurring, which can be done by pre-filtering the projections. In this way, "dips" are introduced in the projections which cancel out the back-projection lines of each image point outside the location of this point. This process is illustrated in the right panel of Fig. 1.6. Mathematically, the derivation of this reconstruction method is based on the **central-slice theorem**, also known as the Fourier slice theorem:

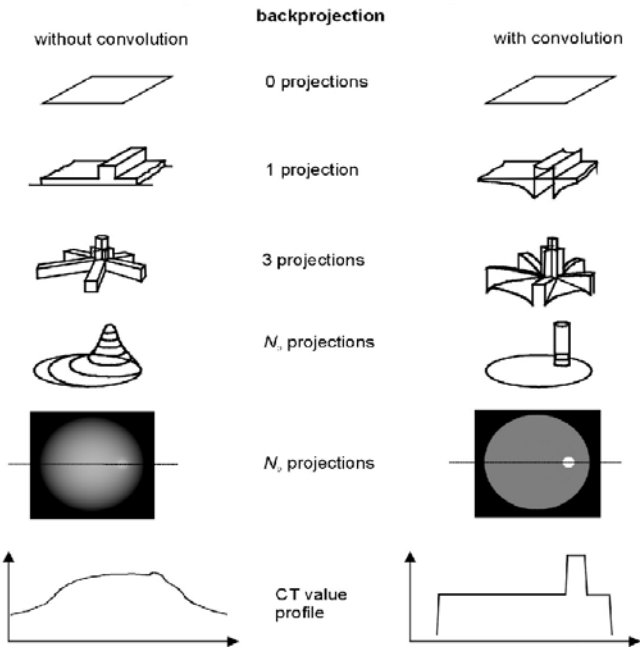

Figure 1.6: The flowchart on the left explains image reconstruction through simple back-projection. Projection views are "smeared back" over the image plane along their viewing direction; the resulting image is significantly blurred. In Filtered Back-Projection (flowchart on the right), projection views are first filtered so that the blurring effect of the back-projection process is eliminated. Figure courtesy of W. Kalender.

Fourier slice theorem*: The Fourier transform of a parallel projection of an object $\mathcal{FT}(P(u,\theta))$ at angle θ is equal to a cross section taken at the same angle through a two-dimensional Fourier transform of the object $\mathcal{FT}(\mu(x,y))$.*

The Fourier slice theorem provides a way to construct a Fourier transform of an object from the Fourier transforms of its line integrals. If one now applies inverse Fourier transform to recover $\mu(x,y)$ from $\mathcal{FT}(\mu(x,y))$ and performs the necessary changes of variables, the following **Filtered Back-projection (FBP)** formula is obtained:

$$\mu_{FBP}(x,y) = \int_0^{\pi} g(x\cos(\theta) + y\sin(\theta),\theta)\mathrm{d}\theta \tag{1.5}$$

$$g(u,\theta) = \int_{-\infty}^{\infty} \mathcal{FT}(P(u,\theta))|\omega| e^{2\pi\, i\omega}\mathrm{d}\omega$$

First, a Fourier transform of a projection $P(u,\theta)$ is filtered by multiplication with the so-called ramp filter $|\omega|$, where ω is the frequency variable. The result undergoes an inverse Fourier transform and a filtered projection $g(u,\theta)$ is obtained. The filtered projection is then back-projected to yield the final image estimate $\mu_{FBP}(x,y)$. Although the filtering step can also be executed by performing convolutions in the projection domain, efficiency calls for first transforming the projections into the frequency domain using a Fast Fourier Transform (FFT). The work-flow described above therefore corresponds to how FBP is typically implemented. The ramp filter that is used enhances the contribution of high frequencies. This has the adverse effect that the noise in the projections is also magnified, as the relative contribution of noise to the signal usually increases with the frequency. In order to suppress this effect, the ramp filter is generally multiplied by a window function providing smooth damping at high values of ω. Depending on the choice of the window function and the cut-off of the filter with respect to the Nyquist frequency of the detector setup, reconstructions with a different resolution-noise trade-offs can be obtained.

The FBP formula of Eq. 1.5 can be generalised to other imaging geometries. In the case of fan-beam acquisitions, additional weighting factors are introduced prior to back-projection of filtered projections and the back-projection is preformed along fans of X-rays. A similar modification of FBP was heuristically derived for circular cone-beam orbits and is known as the Feldkamp algorithm (Feldkamp et al. 1984). In general, however, every new imaging geometry makes it necessary to develop a tailored analytical reconstruction formula. This effort is often undertaken because, once available, analytical reconstruction methods offer a significant advantage over other possible solutions in terms of computation speed. For complex scanning trajectories and detector setups, such as those encountered in volumetric imaging, significant research may be necessary to discover, implement and test relevant analytical reconstruction algorithms. For example, many different solutions have been proposed for helical multi-slice scanning (overview: Wang et al. (2000) and Noo et al. (2003)). One of the recent breakthroughs was the derivation of a filtered back-projection type reconstruction formula involving only a shift-invariant one-dimensional filtering (Katsevich 2002, Noo et al. 2003).

Besides problems with generalisation to new imaging geometries, analytical reconstruction methods suffer from being based on idealised models of CT data. It is assumed that noise-free line integrals can be extracted from projection views measured with a CT scanner and that these line integrals will provide sufficient coverage of the object to allow its reconstruction. As will be shown in the next section, these assumptions are not strictly fulfilled by real CT data.

As a result, significant artefacts emerge in images reconstructed with analytical methods. This fact is the main motivation behind the ongoing development of non-analytical, iterative model-based reconstruction algorithms. Such algorithms and the improvements they bring are the main subject of this thesis.

1.2.3 Image degrading effects in X-ray CT

In this subsection, various sources of artefacts in X-ray CT images will be briefly reviewed. The list of image degrading effects presented below is by no means exhaustive; the discussion has been limited to effects that are addressed in the research presented in this thesis.

- **Beam Hardening.** In Eq. 1.3, a negative logarithm of the normalised detected intensity is taken in order to determine the value of a line integral of the attenuation coefficient $P(u,\theta)$. For an object consisting of a single material, a linear relationship should hold between the value of a line integral and the amount of material crossed by the beam. This is unfortunately not the case for data measured with CT because: (i) the X-ray beams used are not mono-energetic, as shown in Fig. 1.1; (ii) the attenuation coefficients of tissues depend on energy; and (iii) the detectors employed integrate the signals over the whole spectrum of the impinging X-ray beam. As a result, the approximation of line integrals obtained in X-ray CT is given by:

$$P_{POLY}(u,\theta) = -\log \frac{\int I_0(E) e^{-\int_L \mu(E;\vec{x})\mathrm{d}\ell}\mathrm{d}E}{\int I_0(E)\mathrm{d}E} \tag{1.6}$$

  where the term in the denominator represents the signal measured with no object. In

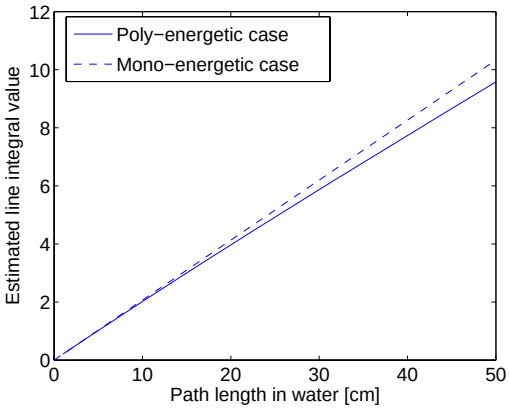

Figure 1.7: Difference between mono-energetic (dashed line) and poly-energetic measurements of line integrals through different thicknesses of water. For the poly-energetic case, the same spectrum as in Fig. 1.1 was used.

Fig. 1.7, P_{POLY} obtained for a water phantom is compared with idealised, monoenergetic value of P, as assumed by analytical reconstruction algorithms. The larger the amount of material traversed, the larger the discrepancy between the mono-energetic and the measured values of line integrals. This is the so-called **beam hardening** effect: since the linear attenuation coefficient decreases with increasing photon energy, the beam is depleted of low-energy X-rays as it passes through the object. The mean energy of X-ray photons therefore shifts upward and the more material is traversed, the less prone to attenuation the beam becomes. As a result, X-ray CT measurements underestimate the monoenergetic values of the line integrals. In consequence, underestimation also occurs in the analytically reconstructed values of attenuation coefficient. The error is most pronounced for central areas of the body, where the ray paths are the longest. The related artefact thus appears as cupping, or as a decrease of image values towards the object's centre. This phenomenon can be observed in Fig. 1.8 *a*. Since most biological tissues have attenuation properties similar to water, human bodies can be treated as relatively homogenous objects and cupping is therefore expected to be the dominant form of poly-energetic artefact. The presence of materials such as bones, which have attenuation properties significantly different from that of other tissues, results in additional streaks in the reconstructions. The streaks are caused by inconsistencies introduced into the set of projections. These inconsistencies emerge due to the fact that the amount of error introduced by beam hardening in bones depends on the orientation of the bony structures with respect to the viewing direction. The streaks usually connect image regions containing bones, as marked by arrows in Fig. 1.8 *a*. In order to reduce the artefacts caused by beam hardening, software preprocessing of projection data is necessary. If a set of measurements with water phantoms of varying thickness is performed, a unique mapping can be found between the measured value of line integral P_{POLY} and the mono-energetic path length through water. Such a mapping can then be reversed in order to estimate the value of mono-energetic projection P from the measured P_{POLY}. This observation forms the basis of the so-called **water correction** method. When bones form a significant portion of the object under investigation, more sophisticated correction methods are needed. Usually, variants of the approach proposed by Joseph and Spital are used (Joseph & Spital 1982): initial reconstruction is first computed from water corrected data, bones are segmented from the image and based on their locations new correction factors are computed and applied to the sinogram.

- **Scatter.** According to Fig. 1.2, scattering is the most probable interaction between diagnostic X-rays and matter. As a result of a scatter event, an X-ray photon is deflected and leaves the beam. It may happen, however, that it will still hit the detector. As a result, the recorded signal is a superposition of **primary radiation** that traversed through the object along straight lines and a relatively smooth (and in most cases less intense) background of **scattered photons**. The presence of scatter increases the number of X-ray photons detected compared to what would have been expected based only on the attenuation in the object. Similarly to the case of beam-hardening, the relative error introduced by the addition of scattered photons is larger for highly attenuated rays than for rays that experienced less attenuation. Resulting artefacts are thus also similar to disturbances introduced by beam-hardening: scatter causes a global cupping distortion and introduces streaking patterns between high-contrast objects (Glover (1982), Fig. 1.8 *a*).

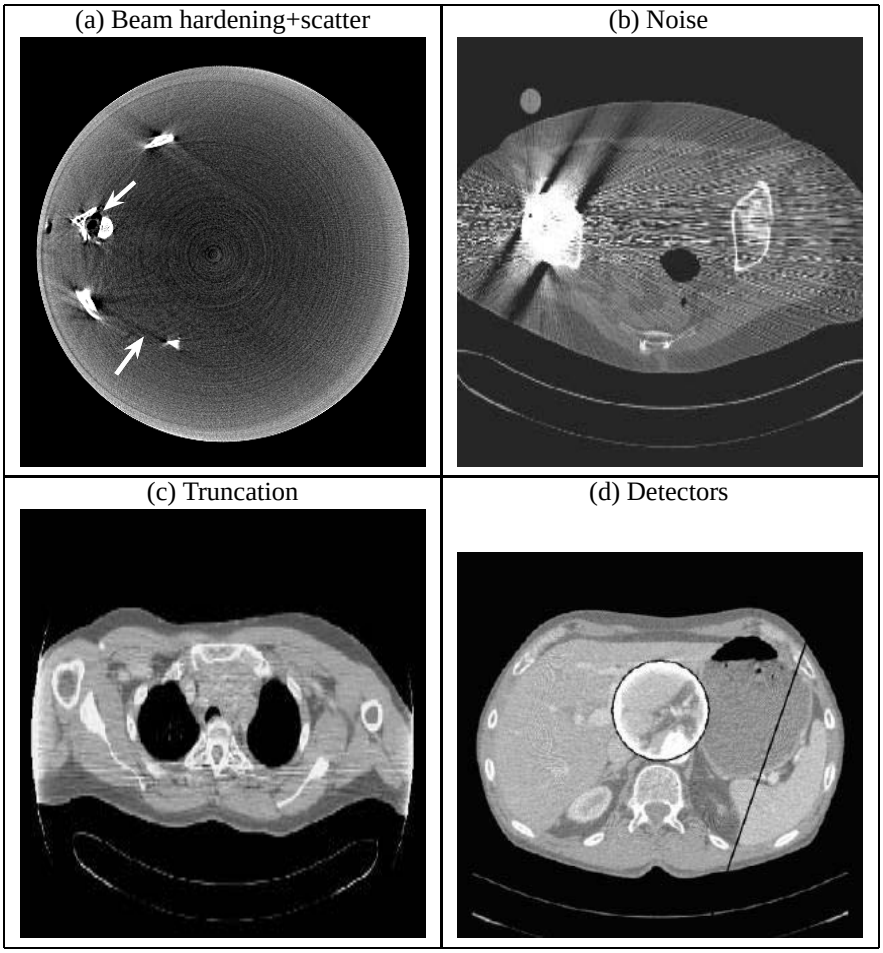

Figure 1.8: Examples of artefacts occurring in X-ray CT images. *a*: Cupping and streaks caused by beam hardening. *b*: Streaks caused by excessive noise. *c*: Truncation artefact. *d*: Ring artefact caused by a malfunctioning detector. Images *b*, *c* and *d* courtesy of W. Kalender

A commonly used method to reduce scatter-induced artefacts is to reject the scattered photons by post-patient collimation. A focused **collimator** is placed above the detector so that only the photons travelling along straight lines from the source are allowed to be detected. This approach is quite effective in single slice, fan-beam systems, where it limits the scatter-to-primary ratios to less than 4%. When the volume covered by the beam and the area of the detector increase significantly beyond a single slice, simple one-dimensional collimation becomes insufficient. Also, if high-resolution detectors consisting of small cells are used, the application of collimators may not be advisable owing to the amount of dead detector area that they would introduce. This situation is for example encountered in micro-CT scanners. In such cases, more sophisticated scatter estimation and correction schemes have to be used. For a survey of available methods the reader is referred to Chapters 5 and 6, where new solutions to the problem of scatter are also presented and tested.

- **Noise.** Projection data measured with CT scanners contain noise originating from two main sources: one, usually dominant, is the quantum noise inherent to X-ray generation and detection processes; the other is the electronic noise in the detector photodiodes and the data acquisition system. The number of quanta of a given X-ray energy measured by a CT detector cell obeys a Poisson distribution. Since photons corresponding to different energies are integrated during the detection, the noise in the total recorded signal follows a compound Poisson distribution (Whiting 2002, Elbakri 2003). Nevertheless, the basic property of Poisson-like distributions is conserved: the larger the mean value of the signal, the larger the signal-to-noise ratio. Relative noise contribution is therefore stronger for projection lines crossing highly attenuating or large structures.

  The noise present in the projection data obviously propagates into the reconstructed images. One of the consequences is the reduction in the detectability of low-contrast structures; they may become almost completely buried under noise. When however excessive noise is encountered in the projection data due to the presence of highly attenuating structures or the large size of the object being scanned, the non-linearity of the logarithm may lead to noise-induced streaks in the reconstructions. Such an artefact is visible around the metallic implant in Fig. 1.8 *b*. In order to battle such issues, the noise in the projection should be kept minimal. This can be achieved by increasing the scanning time or the intensity of the radiation, which however has the negative effect of increasing the **radiation dose** delivered to the patient. Since computed tomography accounts for around 40% of the collective effective dose delivered to the population during medical X–ray examinations (Shrimpton & Edyvean 1998, Hidajat et al. 2001), one of the crucial requirements is to keep the patient's exposure as small as possible while achieving sufficient image quality for the imaging task at hand. Currently this issue is handled by: (i) using techniques such as adaptive tube current modulation, which adjusts the X-ray intensity depending on the amount of attenuation encountered, (ii) careful planning of examinations to optimise scanning protocols depending on patient size and the requirements on image quality, and (iii) advanced, adaptive filtering applied to projection data as a pre-processing step (Hsieh 1998).

- **Incompleteness of projection data.** In two-dimensional imaging, accurate reconstruc-

tion of an object can only be obtained if the line integrals are known for all lines passing through it. If only a reconstruction of a Region-of-Interest (ROI) inside the object is needed, all the line integrals crossing this ROI have to be available (Noo et al. 2002). When these conditions are not fulfilled, the projection data set is incomplete. One example of such a situation is when the object being imaged protrudes outside the area covered by the X-ray beam. This leads to inconsistency between the projection views containing the whole object and the ones containing it only partially. This in turn may generate so-called **truncation artefacts**, shown in Fig. 1.8 *c*, if a reconstruction of the whole object is sought. Incomplete datasets are also created if the rotation arc of the source-detector pair is too short to yield all the necessary line integrals. For fan-beam systems, the minimum angle that has to be covered during data acquisition is $180\,^\circ$ plus the angular extent of the X-ray beam in the trans-axial direction (fan angle). Artefacts emerge if the data is collected over a shorter arc, which is often the case in C-arm systems.

For three-dimensional cone-beam imaging, the Tuy-Smith condition determines which source orbits may result in a complete projection dataset (Tuy 1983, Smith 1985):

> **Tuy-Smith condition:** *Exact cone-beam reconstruction is possible if the trajectory of the cone-beam source intersects every plane intersecting the object.*

A circular cone-beam acquisition obviously does not fulfil this condition, as the source trajectory remains confined to the central imaging plane. Only approximate reconstructions are therefore possible in circular cone-beam tomographic devices, such as micro-CT scanners or C-arm systems. The **cone-beam artefacts** caused by this type of data incompleteness usually appear as overall intensity drop or streaking patterns. They grow in strength as one moves away from the central imaging plane, where the reconstruction is exact. Accurate reconstructions can therefore still be obtained for a range of axial locations, which explains why circular cone-beam scanners found such a widespread use, despite the incompleteness of their data collection.

- **Other effects.** The four categories of artefacts described above are addressed in various ways in the research presented in the thesis. There are of course many other image-degrading effects present in X-ray CT. One more type of artefacts worth mentioning here is generated when the response to radiation of one of the detector cells differs significantly from the response of its neighbours. Such miscalibrated or faulty detector elements result in **ring artefacts** in the reconstructed images (Fig. 1.8 *d*). The erroneous rings correspond to circles that are tangent to the set of all the back-projection lines emerging from a faulty detector pixel for all the viewing angles. In order to deal with such disturbances, either post-processing of reconstructions (Sijbers & Postnov 2004, Riess et al. 2004) or pre-processing of projections (Tang et al. 2001) is employed. In the first case, the rings are detected in the image and reduced by some type of averaging or subtraction, whereas in the second case faulty detector pixels are isolated and their values are modified. Both methods have the disadvantage that they may globally influence the resulting image. In Chapter 7 we will propose an alternative solution to this problem.

  Another category of artefacts that can be tackled with methods similar to the approaches investigated in this thesis is related to the physics of X-ray tubes. Usually, the X-ray

radiation is not emitted from a single point, but from a spatially extended area around the focus. The so-called off-focal radiation may cause shading artefacts and degrade low-contrast detectability. The off-focal radiation can be partially controlled by pre-object collimators placed next to the X-ray source. Such collimators should, however, not be located too close to the source. They must also provide some sizeable opening in order to allow for the creation of a fan- (or cone-) beam covering the entire field of view. As a result, they will never allow for complete rejection of photons coming from outside the focal spot of the X-ray tube.

1.3 Statistical reconstruction methods for X-ray Computed Tomography

In this section we will introduce **statistical image reconstruction methods (SR)**. In short, such algorithms treat the reconstruction task as a statistical estimation problem and therefore take into account the noise in projection data. Moreover, their structure allows the incorporation of detailed system modelling into the reconstruction process. In this way the problem of idealised assumptions about the projection data made in analytical methods can be overcome. Significant improvements in image quality are therefore expected.

The section will be commenced by rewriting the image reconstruction task in a discrete form. Such a form will later be used as the basis for the derivation of statistical reconstruction methods. Finally, the issues related to the implementation of system models in SR will be discussed.

1.3.1 Image reconstruction as a discrete problem

The distribution of the attenuation coefficient $\mu(\vec{x})$ can be expanded in terms of a finite set of **image basis functions** b_j:

$$\mu(\vec{x}) = \sum_{j=1}^{N_v} \mu_j b_j(\vec{x}) \tag{1.7}$$

where N_v is the number of basis functions. One possible choice of $b_j(\vec{x})$ is the basis of voxels: cubic elements centred at points of a rectangular grid covering the image space. Each element of $b_j(\vec{x})$ corresponds to a voxel located at a single grid point and the expansion coefficients μ_j represent the attenuation value within such a voxel, assumed to be constant. A voxel-based image representation is illustrated in Fig. 1.9. The intensity transmitted through an object for a single, monoenergetic X-ray following a projection line L_i can now be written as:

$$I_i = I_{0i} e^{-\int_{L_i} \mu(\vec{x}) \mathrm{d}\ell} = I_{0i} e^{-\sum_{j=1}^{N_v} \mu_j \int_{L_i} b_j(\vec{x}) \mathrm{d}\ell} = I_{0i} e^{-\sum_{j=1}^{N_v} a_{ij}\mu_j} \tag{1.8}$$

where a_{ij} is the line integral taken through the j-th element of the set of image basis functions along the projection line L_i. All the elements of a_{ij} together form a **transition matrix** $\hat{A}$. In the case of voxels, a_{ij} represents the intersection length of ray L_i with voxel j, so each element of the transition matrix describes the contribution of voxel j to the i-th line integral. One can

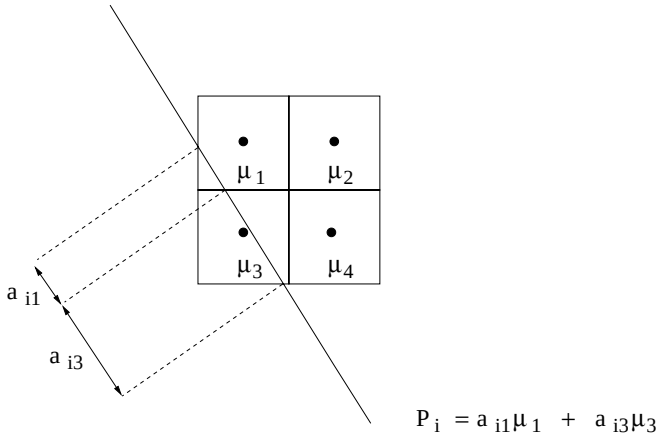

Figure 1.9: In a voxel-based image representation, the object is constructed out of cubic elements located at each point of the image grid and scaled by the image value at this point. The figure also illustrates how a line integral is computed by ray-tracing through a grid of voxels.

now think of image reconstruction from line integrals as of a problem of solving a set of linear equations:

$$\hat{P} = \hat{A}\vec{\mu} \tag{1.9}$$

where $\hat{P}$ is a vector containing all the measured line integrals and $\vec{\mu}$ is a vector of all unknown voxel attenuation values. Such a set of equations could in principle be solved algebraically. Because of potential instability caused by noise and due to the overdetermination of Eq. 1.9 (there are generally more projection lines than unknown voxel values), the use of **iterative techniques** is usually preferred. In iterative approach, one starts with some initial guess for the solution $\vec{\mu}^{(0)}$, calculates its projections by means of some model of data acquisition, compares them with the measured projections, and computes a new solution $\vec{\mu}^{(1)}$ based on the result of this comparison. The solution obtained is used to initialise the next iteration of the algorithm. Reconstruction methods such as the Algebraic Reconstruction Technique (ART, Gordon et al. (1970), Herman (1980)) or Simultaneous Algebraic Reconstruction Technique (SART, Andersen & Kak (1984)) use different variants of iterative approach to solve Eq. 1.9.

1.3.2 Maximum-Likelihood estimation

Similarly to FBP, methods such as ART or SART do not take into account the noise in the projection data. A natural way to address the problem of noise is to treat image reconstruction as a **statistical estimation task**. The intensity measured for each X-ray L_i is now treated as a statistical variable following a Poisson distribution. The mean of this distribution is given by the ideal, noise-free model provided in Eq. 1.8. We now group the intensity values measured for every projection line in a scan into a single vector $\vec{I}^{measured}$. From such a measurement vector, the distribution of the attenuation coefficient can be estimated using the **Maximum Likelihood**

(ML) approach:

$$\vec{\mu}_{ML} = \text{argmax}_{\vec{\mu}\geq 0} \log\left[\,\text{Probability}(\vec{I} = \vec{I}^{measured}; \vec{\mu})\,\right] \tag{1.10}$$

The ML estimate of object $\vec{\mu}_{ML}$ maximises the log-likelihood of the measured set of projections. In order to compute this likelihood, a forward projection step simulating the projections of the current object estimate is necessary during statistical reconstruction. Since finding the maximiser of 1.10 is analytically intractable, iterative algorithms have to be used again. There are many factors to take into account while developing such algorithms for the CT reconstruction problem. The ability to automatically obey the non-negativity constraint $\vec{\mu} \geq 0$, quick convergence, low sensitivity to numerical errors, minimal number of operations, and memory storage required per iteration are the most obvious design requirements. All these factors result in a need to go beyond general numerical maximisation algorithms and exploit the specific structure of the objective function of the CT reconstruction problem. There are various ways to do this; many statistical X-ray CT reconstruction algorithms have thus been proposed. It should be mentioned that some of the ML algorithms used now in X-ray CT reconstruction were first developed for transmission imaging in nuclear medicine. Such imaging is routinely performed to obtain low-resolution attenuation maps for the purpose of attenuation correction in Single Photon Emission Computed Tomography (SPECT). A similar principle as in X-ray CT is used: the detection of photons transmitted through the patient's body and tomographic reconstruction of the object. The main differences with X-ray CT are the use of almost mono-energetic gamma-ray sources and the fact that standard gamma cameras are employed for photon detection. Noise levels in projection data are usually quite high, but the requirements with respect to image quality are lower than in X-ray CT. Despite these differences, the transmission imaging systems used in nuclear medicine are based on very similar principles as CT scanners, so the migration of reconstruction algorithms between these modalities comes as no surprise.

In this work two SR algorithms have been used and they will be explained here in more details. The Convex algorithm has been proposed in 1990 by Lange (Lange 1990). The algorithm uses the following update step:

$$\mu_j^{(n+1)} = \mu_j^{(n)} + \mu_j^{(n)} \frac{\sum_{i=1}^{N_p} a_{ij}\,(I_i(\vec{\mu}^{(n)}) - I_i^{measured})}{\sum_{i=1}^{N_p} a_{ij}\,P_i(\vec{\mu}^{(n)})\,I_i(\vec{\mu}^{(n)})} \tag{1.11}$$

where N_p is the total number of projection lines in the sinogram and the I_i is the *expected* beam intensity for the integration line i, given by Eq. 1.8. The algorithm proceeds as follows: based on a current estimate of the object $\vec{\mu}^{(n)}$, the expected value of the beam intensity is simulated for all projections. The result of this simulation is compared with the measured data $\vec{I}^{measured}$ by subtraction and the result is back-projected over the image plane. The sum in the nominator of Eq. 1.11 expresses this back-projection process. The denominator determines a normalisation term, also computed for each projection line and subsequently back-projected over the image plane. The update term obtained through these back-projections is then used to calculate a new object estimate, $\vec{\mu}^{(n+1)}$. An obvious disadvantage of this approach to image reconstruction is its computational cost: every iteration of the Convex algorithm consists of one forward projection and two back-projections. The potential advantages are twofold. Firstly, noise in the projection data is taken into account. Secondly, the forward model used to simulate the expected value of beam intensity can include many details of photon transport. Image degradation caused in

analytical methods by neglecting effects such as beam-hardening, scatter, or off-focal radiation may therefore be reduced.

In order to tackle the beam-hardening problem, one has to go beyond only improving the modelling step in a statistical reconstruction algorithm. Since the attenuation coefficient depends on X-ray energy, a separate distribution of $\mu(E)$ should in principle be estimated for every energy present in the spectrum of the X-ray tube. If we split the spectrum into K energy bins, each having energy E_k, the number of unknowns in a poly-energetic problem will become $K \cdot N_v$, instead of N_v present in a mono-energetic case. Moreover, most of the information needed to reconstruct these energy-dependent attenuation maps is destroyed in the measurement process, since energy-integrating detectors are used. In order to reduce the number of degrees of freedom, one usually attempts to reconstruct a map of only a single quantity, such as the attenuation coefficient for a single energy value (De Man et al. 2001) or density (Elbakri & Fessler 2003). A relationship is then postulated between the value of this single quantity in a given voxel and the energy-dependent attenuation of X-rays in this voxel. In the case of the Segmentation-Free Poly-Energetic Statistical Algorithm (SR-POLY) proposed in Elbakri & Fessler (2003) and used in this thesis, it is assumed that voxels contain mixtures of M base substances (usually water and bone). For a voxel j, its density ρ_j determines the fraction of material m in this voxel through a set of pre-defined functions $f_m^j(\rho_j)$. The total expected X-ray intensity for the i-th ray is now:

$$I_i = \sum_{k=1}^{K} I_{0i}(E_k) e^{-\sum_{m=1}^{M} a_{ij}\mu^m(E_k) f_m^j(\rho_j)\rho_j} + r_i \tag{1.12}$$

where $\mu^m(E_k)$ is the attenuation coefficient of the m-th substance at energy E_k and r_i is the mean number of random background events, such as scatter. By using models like this one, new poly-energetic objective functions for ML estimation can be obtained and iterative algorithms can be derived to maximise such functions. The general processing chain will again include forward and back-projection steps, which will now be taking into account the poly-energetic nature of X-ray radiation.

In classical SR algorithms, a new object estimate is computed after all projection lines have been simulated. It turns out that if the updates are performed after only a *subset* of projections has been computed, visually appealing images can be achieved much quicker than with a standard algorithm. In such a scheme, each update is performed based on a different subset of projections. The subsets are usually grouping projections that are relatively far apart in terms of angular separation. This idea, known as the **Ordered Subsets (OS)** scheme, has first been proposed in Hudson et al. (1991) for emission tomography. It has to be noted that OS modifications of statistical algorithms destroy their monotonicity and usually yield iterations that converge to a limit cycle. Nevertheless, in practical cases the images obtained do not differ in any significant way from the ones computed with standard SR. This has been for example demonstrated in Beekman & Kamphuis (2001) for an OS version of the Convex algorithm (OSC algorithm). For both fan- and cone-beam X-ray CT data, acceleration of more than two orders of magnitude over the standard Convex algorithm has been achieved (Beekman & Kamphuis 2001, Kole & Beekman 2005*a*). The SR-POLY algorithm has also been proposed by its authors in an OS form (Elbakri & Fessler 2003).

Acceleration of statistical reconstruction methods can be achieved not only by algorithmic

means, but also by hardware methods. Promising solutions include the use of parallel computing (Kole & Beekman 2005*b*) and of floating-point graphic cards (Mueller & Yagel 1998, Kole & Beekman 2006). The rationale for the latter approach will be explained in more detail in the following subsection.

In spite of the long computation time involved, SR is attractive for X-ray CT imaging for several reasons. One of them is the fact that it requires no explicit expressions for inverse transforms and can therefore be easily adapted to any imaging geometry (Manglos et al. 1992, Li et al. 1994, Kamphuis & Beekman 1998*b*, Beekman et al. 1998, Gilland et al. 1997). Furthermore, the use of system modelling in the forward projection step results in more efficient utilisation of available projection data than in analytical algorithms. SR is therefore inherently more robust to truncation of projections and to cone beam artefacts than analytical methods (e.g. Manglos (1992), Gilland et al. (2000), Michel et al. (2005), Thibault et al. (2005)). As mentioned above, models accounting for details of photon emission and transport can be used as forward projectors in SR, thus allowing for reduction of blurring caused by the spatial extension of the source (Bowsher et al. 2002) and of artefacts related to beam-hardening (which has already been explained in this chapter, De Man et al. (2000), De Man et al. (2001), Elbakri & Fessler (2002), Elbakri & Fessler (2003)) and scatter. The latter will be demonstrated in Chapter 6. Finally, since noise is taken into account in the derivation of Maximum Likelihood formula, it is expected that the use of SR may facilitate dose-reduction. The ability to obtain images having similar resolution (or bias), but lower noise level than attained by FBP has already been reported both for conventional X-ray CT (e.g. Nuyts et al. (1998), Zbijewski & Beekman (2004*a*), Ziegler et al. (2004), Thibault et al. (2005)) and for low-count data representative for interventional CT (e.g. Wang et al. (1998)). To the best of our knowledge, however, a systematic study assessing the actual amount of dose reduction that can be achieved has not been published yet.

One issue that should be mentioned regarding the potential dose reduction achievable with SR is that most of statistical reconstruction algorithms are based on a Poisson model of projection noise. As has already been mentioned in the previous chapter, the true statistics of X-ray CT measurements is closer to a compound Poisson distribution. Further research is needed to assess what impact this discrepancy will have on the accuracy of statistical reconstruction and on the possible reduction of dose levels. Some preliminary results (Elbakri 2003) suggest that for high to moderate signal levels the Poisson approximation is good enough, since in this signal domain it results in log-likelihoods similar to that of an exact noise model. For low-count studies, more realistic statistical models may be necessary.

System modelling in statistical reconstruction

A huge amount of projection lines is collected in modern CT scanners. Moreover, high demands regarding image resolution result in reconstructions being performed on very dense image grids. The combination of those two factors makes it extremely impractical to pre-compute and store the transition matrix $\hat{A}$. Both forward projection and back-projection therefore have to be computed on the fly, during each iteration of a statistical algorithm. Efficient implementation of these processes is thus of crucial importance.

- **Ray-tracing and related algorithms.** The concept of ray-tracing can be most easily understood in terms of voxel-based image representation (see Fig. 1.9). A ray is cast from the source towards the detector, all the voxels crossed by the ray are identified and the corresponding intersection lengths are computed. By multiplying the intersection length with the voxel value μ_j, the line integral through this voxel is computed. The first efficient implementation of this method for CT-related applications was presented by Siddon (Siddon 1986). This algorithm forms the core of the software used in this thesis.

  Ray-tracing can also be extended to image representations different from square voxels. For rays that are crossing the volume in directions that are more vertical than horizontal, each intersection of a ray with a row of voxels occurs in between two adjacent grid points. The same holds for rays that are more horizontal than vertical, with columns replacing rows and vice versa. If the attenuation is now computed by interpolating the μ values corresponding to these two adjacent grid points, the resulting line integral corresponds to the case of the volume constructed out of triangular functions having their apexes at each grid point. The related ray-tracing algorithm was proposed by Joseph (Joseph 1987).

  The spherically symmetric Kaiser-Bessel functions, often denoted as **blobs** (Lewitt 1990, Matej & Lewitt 1996) were also used as image basis in X-ray CT reconstructions (Mueller et al. 1999*a*, Mueller et al. 1999*b*, Ziegler et al. 2004). Such blobs are centred at each grid point j and scaled by the attenuation value at this point μ_j. A ray-tracing scheme for the computation of cone-beam line integrals in images built using Kaiser-Bessel functions has been proposed in Mueller et al. (1999*b*). In Chapter 3, statistical reconstruction based on blobs is compared to voxel-based SR with regard to the issue of the so-called edge artefacts.

  When ray-tracing is used for forward projection, many rays can be traced towards each detector and the result can then be averaged to yield the final projection value. Such **detector sub-sampling** is used to account for blurring caused by detector aperture. Similarly, the source can be subdivided into many sub-sources, so that effects such as off-focal radiation can be taken into account. Finally, for poly-energetic simulation each ray may carry a set of line integral values, each of them corresponding to one energy from the spectrum.

  Alternatives to ray-tracing include splatting, often used in blob-based representations (Matej & Lewitt 1996, Mueller et al. 1999*b*) and the recently proposed distance-driven method (De Man & Basu 2004). The latter approach attempts at mitigating two known disadvantages of ray-tracing. One is the non-sequential memory access pattern, caused by the fact that each ray is passing through elements of the image grid that are located far apart in computer memory. The other known problem with ray-tracing is that it may lead to high-frequency, Moiré-like artefacts when used for back-projection.

  Computation of X-ray projections is conceptually very similar to volume rendering known from computer graphics. Since the latter is implemented in the hardware of graphic cards, attempts to employ such cards in iterative X-ray CT reconstruction has been reported (Mueller & Yagel 1998, Kole & Beekman 2006). Large speed-ups are expected with this approach, but the amount of memory available on board of modern consumer graphic cards is still insufficient to store all the data needed during CT image reconstruction.

- **Monte Carlo simulations.** The transport of photons in matter is a stochastic process and therefore fits very well into the framework of Monte Carlo (MC) simulations. In such a simulation, sampling from probability distributions describing various types of interactions is employed to follow many photons through a computer model of the object. First, the photon's direction is randomly selected using the probability distribution describing the geometry of the source radiation. Next, the photon's path to the first interaction site is randomly sampled, based on the known value of the mean free path in the medium. The photon is transported to the interaction site and random sampling, utilising the cross-sections for scattering and absorption, is performed to select the type of interaction. If scatter occurs, the scatter angle is chosen by sampling the differential cross-section. The simulation then proceeds by computing a new free path length. Many photons have to be followed in this manner in order to obtain a reliable, low noise estimate of the data recorded by a detector. Speed is therefore a main point of concern in MC simulations. Variance reduction techniques have been developed to minimise the number of photons that needs to be simulated. One frequently used variance reduction technique is **Forced Detection** (Williamson 1987, Kalos 1963, Leliveld et al. 1996), where photons that have scattered are not allowed to escape the object, but are always forced towards the detector.

  Even if variance reduction techniques are used, MC currently seems to be too slow to be applied as a forward model in statistical X-ray CT reconstruction. Moreover, ray-tracing or similar methods are accurate enough for the simulation of primary radiation. Scatter, however, is a stochastic phenomenon that is extremely difficult to emulate analytically. In Chapters 5 and 6 we develop and validate an accelerated MC simulator of scatter in X-ray CT. We exploit the smoothness of scatter distributions encountered in CT in order to significantly speed-up the simulator, so that it can be included in the framework of SR.

1.4 Motivation and outline of the thesis

As explained above, statistical reconstruction combined with detailed system modelling has the potential to both reduce the dose delivered to patients and to significantly mitigate the influence of image-degrading effects in X-ray CT. On the other hand, the overall quality of images obtained with SR depends on difficult and often not fully understood interaction between factors such as the conditioning of the input projection data, the initial estimate of the object used and the details and accurateness of the system model employed. One has to bear in mind that the observations based on the applications of SR in emission tomography are not always directly applicable to X-ray CT: the latter modality provides much higher resolution and thus imposes more strict demands with respect to image quality and the precision of system models used. The first part of this thesis investigates the most fundamental aspects of system modelling in statistical X-ray CT reconstruction. In **Chapter 2** we show how errors caused by voxel-based discretisation may lead to artefacts in images reconstructed with SR. We also propose a solution to this problem: reconstruction on a very fine grid followed by down-sampling of the reconstructions obtained. This approach leads to almost complete removal of any discretisation-related reconstruction errors. In **Chapter 3** two other possible solutions to the discretisation problem are investigated: the use of image basis based on Kaiser-Bessel functions and smoothing of measured projections prior to reconstruction. It is shown that neither of these methods is more efficient

in the reduction of discretisation-related artefacts than reconstruction on a fine grid. In **Chapter 4** another basic aspect of statistical reconstruction process is investigated: the influence of the initial image estimate. It is shown that by using images reconstructed with analytical methods, significant acceleration of SR's convergence can be achieved in regions surrounding small, high-contrast structures. Even a tenfold speed-up over initialisation with an empty object is attainable. Moreover, it is shown that any excessive noise present in the analytically-reconstructed initial images is efficiently removed by the statistical algorithm.

The second part of the thesis shows how detailed system modelling may improve image quality in X-ray CT. **Chapter 5** and **Chapter 6** deal with the correction of scatter-related artefacts in cone-beam micro-CT. As mentioned above, one of the most prominent current trends in X-ray CT is the growth of volume coverage. Large-area high-resolution detectors are more and more commonly used, not only in micro-CT, but also in human scanners. Demands on image resolution may render application of post-patient collimators infeasible. There is consequently a clear need for software-based scatter correction. One possible approach is to estimate the scatter fields of the objects being scanned by means of Monte Carlo simulations. Such simulations must be significantly accelerated in order to make their use during image reconstruction feasible. Our group proposed a very efficient acceleration scheme that can achieve this goal (Colijn & Beekman 2004). This scheme has been included in an in-house developed Monte Carlo simulator of X-ray CT systems. In **Chapter 5** this accelerated simulator is validated against real data measured with a SkyScan1076 micro-CT scanner. The accuracy of the simulator is proven and detailed studies on scatter contamination of the X-ray micro-CT projections are performed. It is found that scatter-to-primary ratios reaching 20% can be encountered in rat imaging, which proves the necessity of some form of scatter correction. In **Chapter 6** it is shown how one can efficiently achieve such a correction by combining statistical reconstruction methods with rapid Monte Carlo scatter simulations. Results for both real and simulated data are presented. An extension of the MC acceleration scheme used in Chapter 5 is introduced; the new scheme leads to a reduction of the MC scatter simulation time by three to four orders of magnitude as compared to a brute-force simulator. Thanks to the use of a poly-energetic statistical reconstruction algorithm, simultaneous reduction of both scatter and beam-hardening artefacts is achieved; to our knowledge it is the first time that such a combined artefact removal is reported for real micro-CT data.

Another potential advantage of statistical reconstruction methods over their analytical counterparts is that SR is usually more immune to problems caused by the insufficiency of projection data. In **Chapter 7**, cone beam systems with non-continuous detectors are investigated. Detector discontinuities may occur as a result of system design if modular detector technology is used; they also appear as a result of malfunctioning detector cells in classical scanner configurations. Chapter 7 shows that in this case SR requires a complete object coverage in the central imaging plane in order to render an almost artefact-free image; such a coverage should be ensured through appropriate placement of gaps and appropriate selection of the scanning orbit. Statistical reconstruction can then be applied directly to the non-continuous projection data. Analytical algorithms would in this case require sophisticated projection pre-processing. Material presented in Chapter 7 also demonstrates that SR results in less severe cone-beam artefacts than analytical methods.

Chapter 2

Characterization and suppression of edge and aliasing artefacts in iterative X–ray CT reconstruction

Abstract

For the purpose of obtaining X–ray tomographic images, statistical reconstruction (SR) provides a general framework with possible advantages over analytical algorithms like Filtered Back Projection (FBP) in terms of flexibility, resolution, contrast and image noise. However, SR images may be seriously affected by some artefacts that are not present in FBP images. These artefacts appear as aliasing patterns and as severe overshoots in the areas of sharp intensity transitions ("edge artefacts"). We characterize this inherent property of iterative reconstructions and hypothesize how discretization errors during reconstruction contribute to the formation of the artefacts. An adequate solution to the problem is to perform the reconstructions on an image grid that is finer than typically employed for FBP reconstruction, followed by a downsampling of the resulting image to a granularity normally used for display. Furthermore, it is shown that such a procedure is much more effective than post–filtering of the reconstructions. Resulting SR images have superior noise–resolution trade-off compared to FBP, which may facilitate dose reduction during CT examinations.

2.1 Introduction

Statistical methods for tomographic reconstruction like Maximum Likelihood Expectation Maximization (ML-EM, Shepp & Vardi (1982), Lange & Carson (1984)) or the Convex algorithm (Lange (1990)) take into account the statistical noise in the projection data, so that noise can be reduced in the reconstructed image. In addition, these methods can incorporate accurately the precise details of photon transport and the emission process in the transition matrix. SR is also flexible enough to be applied to a large variety of image acquisition geometries, since it

requires no explicit expressions for inverse transforms. Consequently, statistical methods for image reconstruction are attractive for X–ray computed tomography (X–ray CT), despite the long computation time that is currently involved.
Potential benefits of using SR for obtaining X–ray CT images include (i) the removal of streak artefacts when fewer projections are used, (ii) suppression of polychromatic artefacts, (iii) resolution recovery, (iv) contrast enhancement and (v) better noise properties in low–count studies (e.g Nuyts et al. (1998), Wang et al. (1998), De Man et al. (2000), De Man et al. (2001), Elbakri & Fessler (2002), Bowsher et al. (2002)). Nevertheless, for X–ray CT applications considerable work has still to be done in order to characterize issues such as reconstruction convergence and quality of the images obtained with SR for different parameter settings and imaging geometries. The removal of edge and aliasing artefacts from the reconstructions is one of the issues of crucial importance if SR is to be utilized in X–ray CT. These artefacts appear as severe over– and under–shoots in the regions of sharp intensity transitions and are much more pronounced and disturbing for statistical reconstruction than for FBP. The edge artefacts in SR have been well described for Emission Computed Tomography (ECT) (e.g. Snyder et al. (1987)). They can be explained as a combined effect of two factors. The first factor is the inevitable loss of high frequency components during the detection process, which leads to Gibbs phenomenon when attempts are made to perform the ill–posed deblurring operation. Consequently, such errors should be only present when a blurring component (e.g. detector and/or collimator response) is modeled in the reconstruction algorithm. The second factor is the mismatch between the kernel of the reconstruction algorithm (the model of the detector blurring) and the true blurring in the system. This is a manifestation of a more general observation: the more accurate the simulation of photon transport and detection process during the reconstruction, the better the quality of the images obtained. When statistical reconstruction is employed to X–ray CT, detector blurring is only barely involved and straight rays are used to model the acquisition of projections. Despite that, disturbing edge overshoots and interference–like patterns appear in SR images that are not present in FBP reconstructions. Errors of this kind have already been observed by several authors (e.g. Nuyts et al. (1998),De Man et al. (2000)). However, a thorough analysis of the causes of edge and aliasing disturbances and of methods to avoid them is still lacking. The goal of this paper is to explain the development of these artefacts. To this end, a model based on a thorough analysis of the discrete simulation of projections (typically employed in SR) is presented (Section 2.2). Artefact suppression by employing a finer reconstruction grid than is typical in Filtered Back Projection is a direct consequence of the proposed artefact formation model. This approach will be evaluated and compared with post–filtering in the Results section.

2.2 Methods

In this section first a hypothesis explaining the edge artefacts formation is put forward. From this hypothesis a simple method stems that should prevent the artefacts appearance. Subsequently details are described concerning the simulation experiments, reconstruction algorithms and data analysis procedures used to test the proposed model and artefact suppression methods.

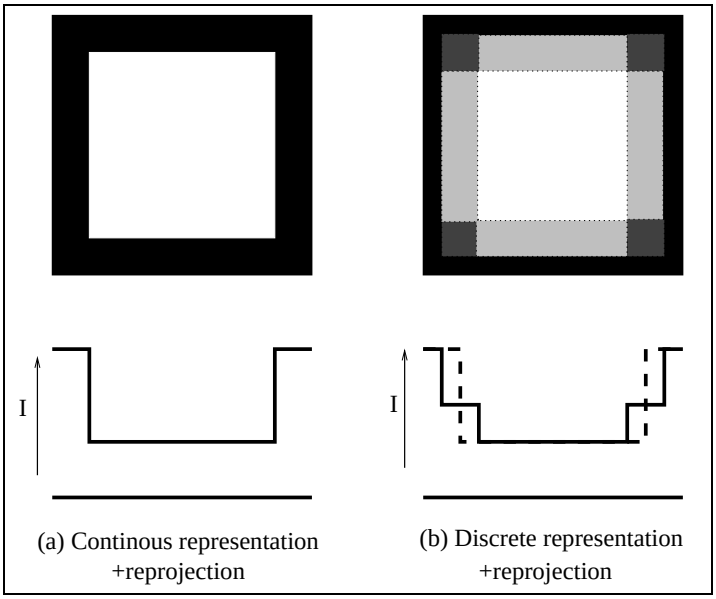

Figure 2.1: The continuous (a) and discrete (b) representation of a block object together with the intensity (I) projections obtained. Due to voxelization, the edges of the object get blurred, which in turn leads to blurring of the calculated projections. The reconstruction algorithm makes an attempt to achieve agreement between real (a) and simulated (b) projections. Therefore, deblurring of the discrete object (b) is required, which may lead to introduction of erroneous voxels into the reconstruction.

2.2.1 Artefact formation model

In Fig. 2.1 the continuous (a) and voxelized (b) representation of an object are compared. A voxel is defined here as a square area with a value equal to the normalized integral of the real, fine structured attenuation distribution over this square. The related discrete representation of the physical attenuation distribution will be referred to as the "ideal voxelized object". In order to simulate projections of an image estimate during the reconstruction ("reprojection" or "forward projection"), a couple of line integrals per projection bin is taken through the voxelized representation of an object, for example using the Siddon algorithm (Siddon (1986)). In the ideal voxelized object, the edges of the real, physical attenuation distribution that lie inside any of the voxels will get blurred as illustrated in Fig. 2.1 (b). As a result, for a ray bundle that passes the outermost voxels of the ideal voxelized object, over or underestimation of simulated line integrals compared to the measured ones will occur, depending on the position of the individual rays with respect to the actual edge. Therefore the reprojections of an ideal voxelized representation of the physical attenuation distribution are inconsistent with the measured projections. A statistical algorithm will try to produce an object distribution which matches the measured projections according to some likelihood measure. We hypothesize that for a coarse grid better consistency is achieved when an object with erroneous edges is constructed instead of the ideal voxelized version of the physical distribution. The angle dependence of the voxelization–induced blurring of the simulated projections can be assumed to cause the aliasing patterns that accompany the artefacts

If the utilization of a voxelized representation of an object indeed leads to modeling errors underlying the formation of edge artefacts, it should be possible to suppress these disturbances by performing the reconstruction on a very fine grid. In the Results section it is shown that this solution is indeed an effective countermeasure to the problem of both edge and aliasing artefacts and that this approach is superior to post–filtering of the reconstructions, the more heuristic practice often used.

2.2.2 Simulation

Simulated projections of a central slice of a three–dimensional, mathematical abdomen phantom (Fig. 2.2, Schaller (1999)) were generated. The phantom axes lengths were 400 mm and 240 mm. Low (10 HU) contrast circular lesions of varying size (diameters: 2 mm, 3 mm, 4 mm, 5 mm, 6 mm, 8 mm, 10 mm and 12 mm) were placed in a region modeling the liver. The ribs were modeled as two circular objects with a contrast of 1000 HU, situated on the long axis of the phantom.

For the assessment of image resolution, three 0.5 mm wide line–shaped patterns with a contrast of +500 HU were added to the phantom. Lines were placed equidistantly starting from the center of the object. For the estimation of small object contrast, a 4 by 4 grid of 2 mm squares with a contrast of +500 HU was placed in a uniform background area. The distance between the centers of the squares was 6 mm.

Transmission data for a fan–beam geometry were simulated by calculating the attenuation along rays through the object. The projection data contained 1000 views, acquired over $360\,^{\circ}$. The distance between source and detector was 1000 mm and the magnification factor was set to 2. The detector contained 500 projection pixels, each having a width of 2 mm. In order to em-

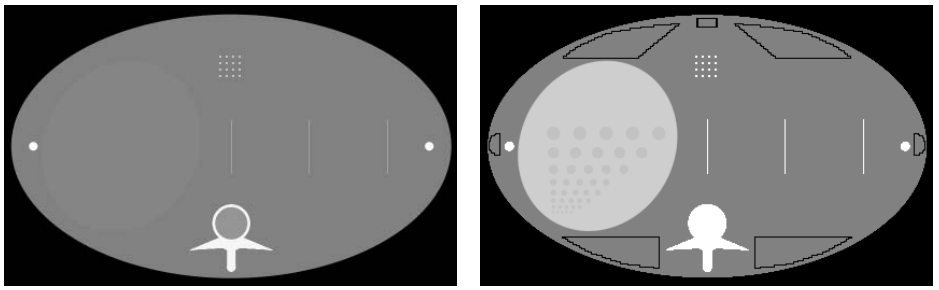

(a) Abdomen phantom, full gray–scale

(b) 0.9–1.1 scale, regions for ME calculation superimposed

Figure 2.2: Slice of the modified Schaller abdomen phantom. Panel (a): full gray–scale range. Panel (b): compressed 0.9–1.1 scale with the outlines of the regions used for mean error calculations superimposed.

ulate the fine resolution character of the transmission data, the phantom was constructed on a 4096x4096 square matrix consisting of 125 μm voxels and the number of rays traced per detector element was set to sixteen. This simulation grid is four times denser than the grid employed for the reconstruction (see also Section 2.2.3); the fine voxelization used is proven to be more than sufficient to make an adequate estimate of real density distributions (Goertzen et al. 2002). Poisson noise was generated in the simulated projections assuming 10^6 photons per detector in an unattenuated X–ray beam. This corresponds to the intensities used in clinical practice (Guan & Gordon 1996). For water, a constant attenuation factor of 0.168 cm $^{-1}$ was assumed.

2.2.3 Reconstruction

Statistical reconstruction routines were based on the Ordered Subsets Convex algorithm (OSC). In this approach, the convex algorithm is combined with an ordered subsets method in order to speed up the computations. For X–ray CT, the reduction in the computation time achieved can be about two orders of magnitude, while visual appearance of the images obtained, as well as their resolution–noise and contrast–noise tradeoff remain the same as for the standard Convex algorithm (Beekman & Kamphuis (2001)). In the present study, 40 iterations of OSC with 125 subsets were employed for the reconstruction. Such a relatively large number of iterations is required in order to suppress streak artefacts around the circular objects modeling the ribs (Zbijewski & Beekman (2004*c*)).

The reconstructions were performed using three different grid sizes: 2048x2048, 1024x1024 and 512x512 voxels (Table 2.1). Afterwards the images obtained for denser discretizations were all downsampled to 512x512 voxels by adding together assemblies of four or sixteen voxels. In the sequel these final reconstructions will be referred to as: $OSC\text{–}FOLD_{2048}$, $OSC\text{–}FOLD_{1024}$ and $OSC\text{–}NOFOLD$, respectively. For each of the grids, the same subsampling of 4 rays per detector pixel was utilized during the ray–tracing, both for forward and back-projection steps of the algorithm. The back-projector was an exact transpose of the projector, both were based on the Siddon algorithm (Siddon (1986)).

algorithm	number of reconstruction voxels	size of the voxel	size of the detector bin	#rays per bin
simulation phantom	4096x4096	0.125x0.125 mm	2 mm	16
$OSC\text{–}FOLD_{2048}$	2048x2048	0.25x0.25 mm	2 mm	4
$OSC\text{–}FOLD_{1024}$	1024x1024	0.5x0.5 mm	2 mm	4
$OSC\text{–}NOFOLD$	512x512	1x1 mm	2 mm	4
FBP	512x512	1x1 mm	2 mm	4

Table 2.1: Details of the discretizations used for simulation and reconstructions.

The object was also reconstructed with the Filtered Back Projection algorithm using CTSim 3.5 package (Rosenberg 2002). FBP reconstruction was performed on a grid of 512x512 voxels, using a ramp filter with a cutoff at the Nyquist frequency.

2.2.4 Assessment of image resolution and noise and quantitation of the artefacts

- *Noise measurement.* For each initialization method analyzed, the set of reconstructions obtained consisted of six images, each calculated from a different noise realization of the projection data. For each possible pair of reconstructions from such a set, the images forming the pair were subtracted. Then, the standard deviation in a region covering the liver was computed for each of the resulting difference images:

$$\mathrm{SD}_i = \sqrt{\frac{\sum_k^N \tilde{\mu_i}^d(k)^2}{N-1}} \tag{2.1}$$

  where N is the total number of voxels in the region of interest and $\tilde{\mu}_i{}^d(k)$ represents the value of voxel k in the i-th difference image. Finally, the standard deviations were averaged over all difference images to produce the final numerical estimate of the noise:

$$\mathrm{Noise} = \frac{1}{K}\sum_i^K \frac{\mathrm{SD}_i}{\sqrt{2}} \tag{2.2}$$

  where K is the number of difference images. In this way we ensured, that the noise measurement was not biased by the non–uniformities in the reconstruction.

- *Resolution measurement using the high intensity line-shaped objects.* For each of the three line objects placed in the phantom, the Full Width at Half Maximum (FWHM) was determined from a 30 mm wide profile drawn perpendicular to the line. Prior to the calculation of the FWHM, the background surrounding the line objects was removed from the reconstructed image by subtraction of a noiseless reconstruction performed without the line pattern. The FWHM for a single line in a single noise realization was calculated as follows: The profile through the line was modeled as a set of segments connecting adjacent points that represented profile values. The FWHM is defined as the distance between

the locations where these segments cross the half of maximum pixel value. Subsequently, FWHMs were calculated for all six images with different noise realizations and averaged. For further comparisons the mean resolution of the three lines is used.

- *Quantitation of the artefacts*. For the measurement of the strength of the artefacts, noise–free projections were reconstructed using FBP, $OSC–NOFOLD$, $OSC–FOLD_{1024}$ and $OSC–FOLD_{2048}$ (for statistical algorithms 40 iterations were performed). In order to facilitate comparisons over a range of image resolution values, the reconstructions obtained were post–filtered with a set of Gaussian kernels (with FWHM varying from 1 mm to 2 mm). Finally, for each value of image resolution, the mean error in a union of image regions covering the most pronounced aliasing patterns (on the top of the object, around the ribs and around the spine, Fig. 2.2 (b)) was computed. Mean error is defined as the absolute difference between the corresponding pixels in the noise–free reconstructions and in the original image:

$$\text{ME(r)} = \frac{1}{N}\sum_{k}^{N} |\bar{\mu}(k) - \mu(r;k)| \tag{2.3}$$

where r represents image resolution, $\mu(r;k)$ refers to the value of pixel k in a reconstruction blurred to the resolution r, N is the number of pixels in the region of interest and $\bar{\mu}(k)$ is the attenuation of pixel k in the phantom.

2.3 Results

Prior to visual examination, all the OSC reconstructions were resampled to 512x512 grid (if necessary) and blurred with Gaussian kernels to equalize their resolution or noise values with that of the FBP image. In Fig. 2.3 different reconstructions, all displayed at 512x512 grid, are compared at equal noise. Fig. 2.4 compares the same reconstructions at equal resolution. In both figures the panels on the left display reconstructions of a single noise realization of the projection data (gray-scale: 0.9–1.1). In the panels on the right a compressed 1.0–1.02 scale (meant to emphasize the artefacts) is employed to show means of the images computed from six different noise realizations of the projection data. Despite many iterations performed, some streaks emerging from the ribs can be perceived in the OSC images, albeit only for the narrow gray–scales. Artefacts of this kind are independent from the edge disturbances; they have been investigated in more details in Zbijewski & Beekman (2004*c*) and it has been shown that they can be prevented by FBP–initialization of the iterative algorithm.
$OSC–NOFOLD$ reconstructions shown both in Fig. 2.3 (a) and in Fig. 2.4 (a) are severely corrupted by edge and aliasing artefacts that are not present in the FBP image (Fig. 2.3 (d)). These artefacts are more pronounced in Fig. 2.3 because less blurring was necessary to obtain match between the noise levels of OSC and FBP reconstructions than to equate their resolutions (as can be deduced from the noise and resolution values provided with the images and summarized in Table 2.2). $OSC–FOLD_{2048}$ adequately corrects the edge disturbances, so that none artefacts can be perceived either in Fig. 2.3 (c) or in Fig. 2.4 (c). For $OSC–FOLD_{1024}$ some slight remnants of the overshoots are present only in Fig. 2.3 (b), where less post–filtering was

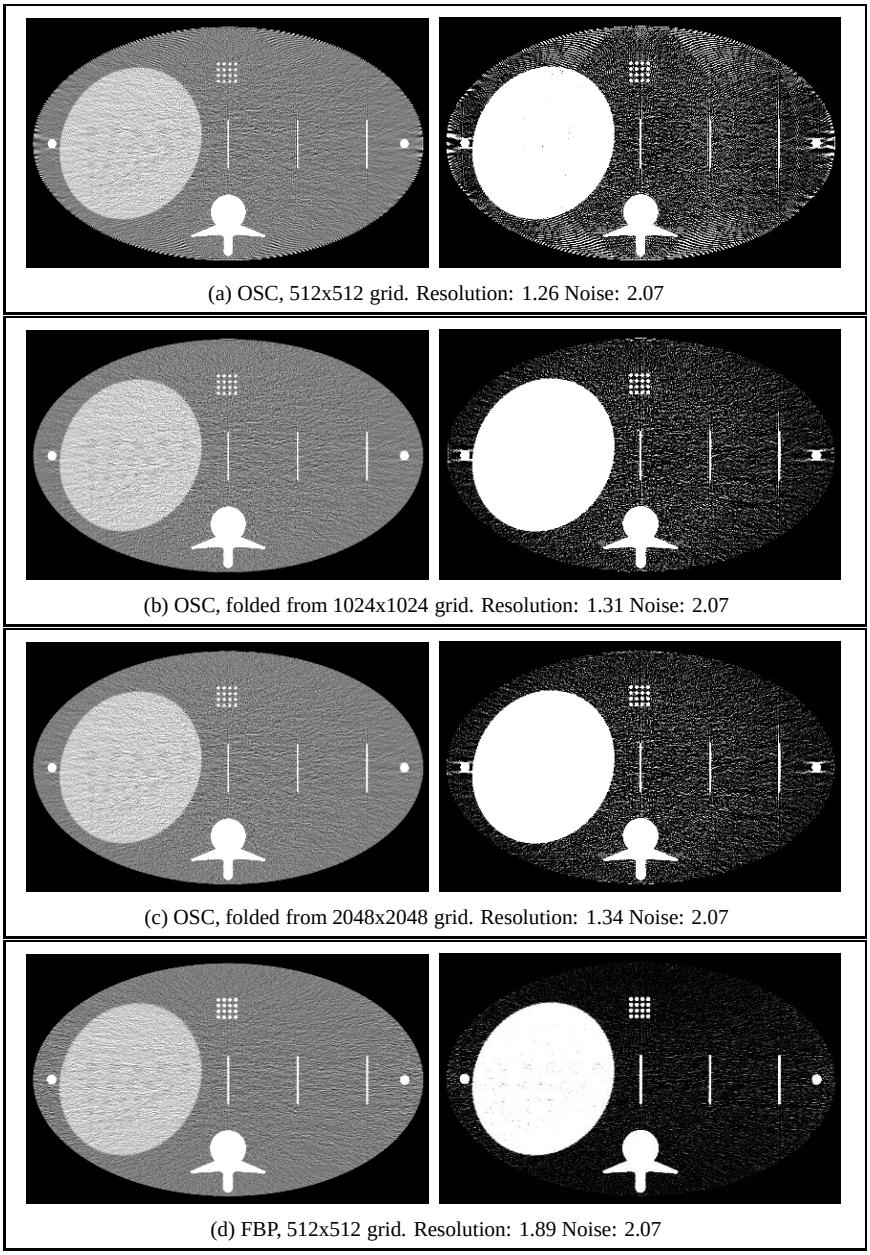

(a) OSC, 512x512 grid. Resolution: 1.26 Noise: 2.07

(b) OSC, folded from 1024x1024 grid. Resolution: 1.31 Noise: 2.07

(c) OSC, folded from 2048x2048 grid. Resolution: 1.34 Noise: 2.07

(d) FBP, 512x512 grid. Resolution: 1.89 Noise: 2.07

Figure 2.3: Different reconstructions analyzed in the paper compared at equal noise. On the left images computed from single noise realization of projection data are displayed using 0.9–1.1 scale, on the right means of the reconstructions obtained from different noise realizations are shown using a compressed 1.0–1.02 scale. Edge and aliasing artefacts are strongly pronounced for OSC reconstruction performed directly on 512x512 grid (panel (a)). For $OSC\text{–}FOLD_{1024}$ (panel (b)) only slight remnants of the artefacts are visible near the top of the image. The $OSC\text{–}FOLD_{2048}$ reconstruction (panel (c)) and the FBP image (panel (d)) do not exhibit any edge disturbances.

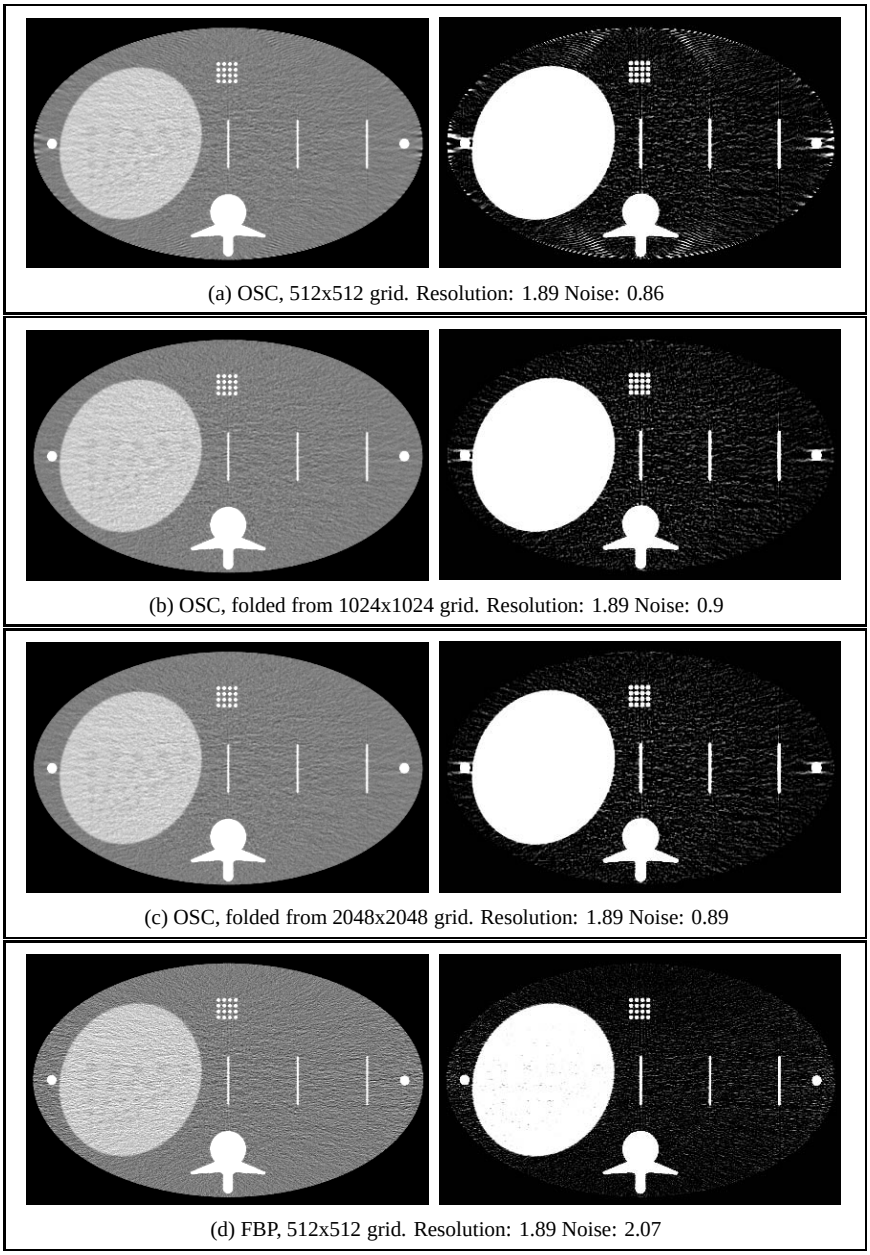

(a) OSC, 512x512 grid. Resolution: 1.89 Noise: 0.86

(b) OSC, folded from 1024x1024 grid. Resolution: 1.89 Noise: 0.9

(c) OSC, folded from 2048x2048 grid. Resolution: 1.89 Noise: 0.89

(d) FBP, 512x512 grid. Resolution: 1.89 Noise: 2.07

Figure 2.4: Like Fig. 2.3, but images filtered to equal resolution. Edge and aliasing artefacts are clearly visible for OSC reconstruction performed directly on 512x512 grid (panel (a)). The OSC reconstructions computed on a 1024x1024 (panel (b)) and 2048x2048 (panel (c)) grids and then folded down to 512x512 voxels, as well as the FBP image (panel (d)), do not exhibit such disturbances.

image	mean resolution	noise in liver area	mean resolution at noise of 2.07	noise in liver area at 1.89 mm resolution
FBP	1.89 mm	2.07	1.89 mm	2.07
OSC–$NOFOLD$	1.10 mm	3.35	1.26 mm	0.86
OSC–$FOLD_{1024}$	1.19 mm	2.79	1.31 mm	0.90
OSC–$FOLD_{2048}$	1.28 mm	2.36	1.34 mm	0.89

Table 2.2: Mean resolution and noise (calculated for 512x512 grid) for FBP and for OSC reconstructions incorporating different strategies for edge artefact removal. The second and third column display values achieved after 40 iterations of OSCs. In the sequel OSC images are displayed at matching noise or resolution with the FBP reconstruction, relevant resolution and noise values are given in the fourth and fifth column.

employed. These artefacts are however visible only for the compressed gray–scale and are very localized, thus do not seriously degrade the reconstructions. It can be concluded that in this study doubling of the reconstruction grid voxelization in OSC–$FOLD_{1024}$ was sufficient to almost completely remove the edge and aliasing disturbances.

Gaussian post–filtering reduces the strength of the artefacts and can in principle be used to remove them from OSC–$NOFOLD$ reconstruction. Fig. 2.5 shows the mean error (defined in Eq. 2.3) as a function of resolution (varied by smoothing the initial reconstruction) for FBP, OSC–$NOFOLD$, OSC–$FOLD_{1024}$ and OSC–$FOLD_{2048}$. The mean error for OSC–$NOFOLD$ is always higher than for other reconstructions. This is in agreement with Fig. 2.3 and Fig. 2.4, where the artefacts are most pronounced for the OSC performed directly on 512x512 grid. The initial difference in mean error between OSC–$FOLD_{1024}$ and OSC–$NOFOLD$ (when compared at equal resolution) is almost one order of magnitude. The amount of smoothing necessary to compensate for this initial difference would bring the resolution of the OSC–$NOFOLD$ image even below the value attained by an artefact–free FBP reconstruction. This renders post–filtering inferior to the proposed, more fundamental solution of utilizing a fine grid for the reconstruction.

Further analysis of Table 2.2 shows that, when compared at equal resolution (cf. Table 2.2, 5th column), the noise level of FBP reconstruction is about two times higher than for the OSC reconstructions. When comparison is made at matching noise (cf. Table 2.2, 4th column), the mean resolutions of the blurred OSC images is superior to the resolution achieved by FBP. This opens some perspectives for dose reduction, as discussed in the next section.

An additional experiment was carried out to support our hypothesis concerning the sources of the edge artefacts, namely that their cause lies mainly in reprojection and not so much in the back-projection. For a 2048x2048 image grid, each reprojection step of the reconstruction algorithm was performed using the image space folded to the granularity of 512x512 voxels. In this way, smoothing of simulated projections caused by the use of sparse discretization was introduced into the reconstruction performed on a dense grid. Fig. 2.6 (a) displays reconstruction which was obtained using this modified algorithm. It is displayed together with OSC–$NOFOLD$ image of the same resolution Fig. 2.6 (b) (identical with Fig. 2.4 (b)). Edge and aliasing artefact patterns are slightly more pronounced for the modified algorithm than for OSC–$NOFOLD$, but their appearance is in general very similar in both images. An important difference between this

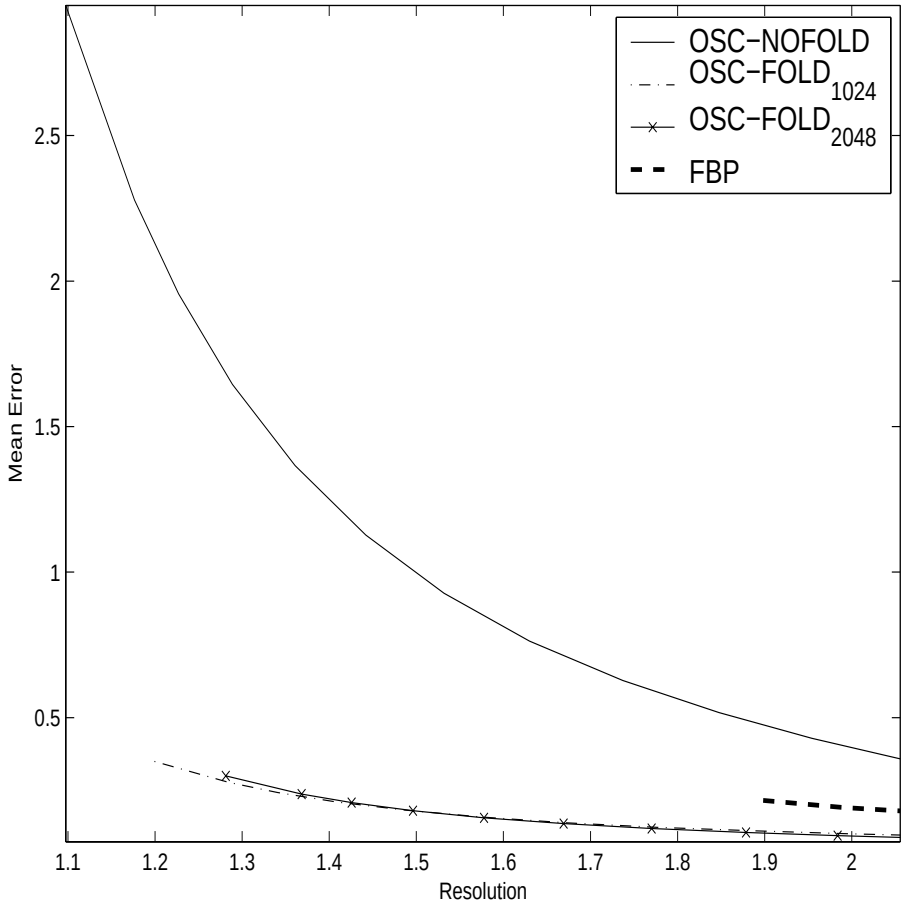

Figure 2.5: Mean error in the regions containing the strongest aliasing patterns as a function of image resolution. The calculations were performed for noise–free reconstructions. Even at resolutions lower than the initial resolution of the FBP image, $OSC–NOFOLD$ attains larger values of mean error than any other reconstruction analyzed. This is in agreement with the presence of edge artefacts in the corresponding $OSC–NOFOLD$ images (cf. Fig. 2.4 and Fig. 2.3).

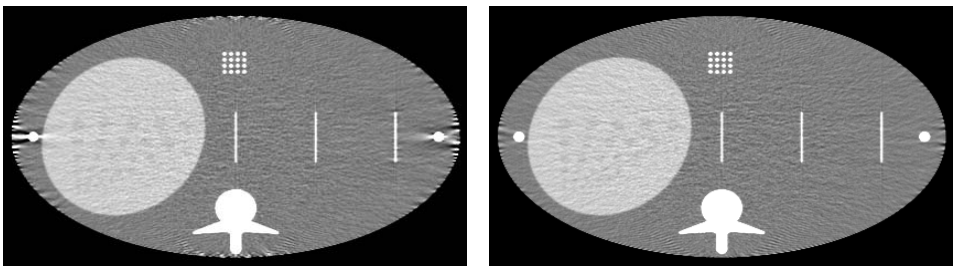

(a) Artificially induced artefacts
Resolution: 1.89 Noise: 0.81

(b) OSC, 512x512 grid
Resolution: 1.89 Noise: 0.86

Figure 2.6: Panel (a): OSC reconstruction performed using a 2048x2048 voxels grid for back projections, but a folded 512x512 image space for reprojections. Image is displayed at 512x512 voxels. Panel (b): $OSC–NOFOLD$ image of similar resolution. Artificially induced edge artefacts in (a) and the disturbances visible in $OSC–NOFOLD$ image from panel (b) are very similar.

experiment and the standard reconstruction algorithm used in this study is that in the standard implementation of OSC the projector and backprojector match each other, while in the experiment they are unmatched due to the use of different discretizations. Consequently, the artefacts appearing for the modified algorithm might be, at least partially, a result of this mismatch. On the other hand, the edge disturbances present for the modified OSC are very similar to those found in $OSC–NOFOLD$ images and it is certain that the latter cannot be an effect of a projector/backprojector mismatch. The success of dual matrix approach, demonstrated already for emission tomography (e.g. Zeng & Gullberg (1992), Kamphuis et al. (1998), Zeng & Gullberg (2000)) also indicates, that the quality of backprojector and the match between projector and backprojector are actually not critical for the convergence of iterative algorithms. It therefore seems to be more likely that in both cases the artefacts have similar origins, ie. the blurring that is introduced into the forward projection due to the use of a sparse discretization. Therefore the above described experiment gives indeed additional support to our hypothesis about the origins of the edge artefacts.

2.4 Discussion and conclusions

In this paper the hypothesis was tested that edge overshoots and aliasing patterns in X–ray CT statistical reconstruction are caused by the disturbances introduced into the reprojection step of the algorithm as a result of the use of a discrete, voxelized model of an object. Artefacts indeed disappear if discretization is reduced by using smaller voxels. In addition, an experiment was performed, where only the forward projection was performed using a sparse discretization. The final image exhibited very similar artefact patterns as for the reconstructions executed entirely on a sparse grid.

Edge disturbances and aliasing patterns can be effectively prevented by conducting the reconstruction on a finer grid. We have demonstrated that this method is much more effective than post–filtering of the images reconstructed on a coarser grid. In particular, reconstruction on a

finer grid leads to better image resolution–noise trade–off than post–filtering, because the latter requires significant blurring in order to completely remove the artefacts.
Images obtained with OSC have also superior resolution–noise trade–off compared to the FBP reconstruction. Consequently, if only sufficiently dense grid is employed during the reprojection, OSC can provide artefact–free images having similar noise and resolution to an FBP image achieved using a larger radiation dose. To quantify the possible dose reduction, however, an elaborate study is required, utilizing a variety of image quality benchmarks including task–oriented measures. Such a study would be very extensive and therefore is beyond the scope of this paper.
The use of fine grids leads to an increase in the reconstruction time; the increase in the amount of operations is approximately inversely proportional to the linear voxel size in the discretization. One iteration of OSC accounts for processing all the projections once. For each projection, the OSC algorithm performs one forward and two backprojection steps. Since the time of backprojection is dominant for FBP, it can be concluded that one iteration of OSC takes three times longer, than the FBP reconstruction of the whole object performed on the same grid. In our study, a grid two times denser than employed in FBP was sufficient to remove the artefacts from OSC images. This slows down the statistical reconstruction by additional factor of two, yielding the execution time of one iteration of OSC roughly equivalent to six full FBP reconstructions. So far, improvements in the computation speed for SR were achieved mainly by means of block–iterative methods (reviewed in Leahy & Byrne (2000)). The ordered subsets convex algorithm (Kamphuis & Beekman (1998*a*), Erdo ğan & Fessler (1999)) utilized in the presented paper belongs to this category of methods. In Beekman & Kamphuis (2001) it was shown that for X–ray CT, OSC produces almost an equal resolution and lesion contrast as the standard convex algorithm but does so more than two orders of magnitude faster. The need for dense reconstruction grids, however, leads to a slowdown in computation time that hampers the standard and block–iteratively accelerated SR to the same extent. In this case, solutions allowing for fast execution of forward– and back–projection steps of the algorithm, perhaps by means of hardware acceleration (e.g. Mueller & Yagel (2000)) or alternative sampling strategies (e.g. Mueller et al. (1999*b*), De Man & Basu (2004)) may be crucial in speeding up the reconstruction.
In Mueller et al. (1999*b*), square voxels are replaced with spherically symmetric Kaiser–Bessel base functions (also known as blobs, Lewitt (1990), Matej & Lewitt (1996)) and the independence of their line integrals on the projection angle is exploited to devise an effective volume sampling strategy. Other attractive properties of blobs, such as smoothness and effective band limitedness may lead to reduced edge artefacts in comparison with voxelized representation. It will however not solve the problem completely, since edge artefacts will always be present if the object under investigation contains sharp edges and if the resolution of the detector system is sufficiently high. Therefore the potential advantages of blobs for edge artefacts suppression should be investigated in a separate study. Since Kaiser–Bessel windows has not been widely used in iterative X–ray CT reconstruction, such a study must actually go beyond the subject of edge artefacts and is therefore outside the scope of this paper.
Combining several acceleration schemes and availability of faster computers will bring the execution times for X–ray SR down to a level acceptable for a wider variety of clinical applications. The necessary technical and scientific effort is worthwhile, because of the possible gain in the

image quality over the analytical methods is apparent.

Acknowledgments

We thank to Dr. Auke-Peter Colijn for critical comments and discussions.

Chapter 3

Comparison of methods for suppressing edge and aliasing artefacts in iterative X–ray CT reconstruction

Abstract

X-ray CT images obtained with iterative reconstruction (IR) can be hampered by so-called edge and aliasing artefacts, which appear as interference patterns and severe overshoots in the areas of sharp intensity transitions. Previously, we have demonstrated that these artefacts are caused by discretization errors during the projection simulation step in IR. Although these errors are inherent to IR, they can be adequately suppressed by reconstruction on an image grid that is finer than the one typically used for analytical methods such as Filtered Back-Projection. Two other methods that may prevent edge artefacts are: (i) to smooth the projections prior to reconstruction or (ii) to use an image representation different than voxels; spherically symmetric Kaiser-Bessel function are a frequently employed example of such a representation. In this paper we compare reconstruction on a fine grid with the two above-mentioned alternative strategies for edge artefact reduction. We show that the use of a fine grid results in a more adequate suppression of artefacts than the smoothing of projections or using the Kaiser-Bessel image representation.

3.1 Introduction

For several years now there has been renewed interest in the application of iterative reconstruction methods (IR) to X-ray CT data. Iterative algorithms have numerous potential advantages over their analytical counterparts, namely: (i) greater flexibility with respect to the choice of image acquisition geometries, (ii) reduced vulnerability to sampling issues such as cone-beam

artefacts (Thibault et al. 2005), limited field-of-view (Michel et al. 2005) or limited acquisition arc and (iii) their ability to incorporate precise models of photon transport, which allows for e.g. suppression of beam-hardening and/or scatter-induced artefacts (De Man et al. 2001, Elbakri & Fessler 2002, Zbijewski & Beekman 2006). In addition to these advantages, significant dose reduction (Zbijewski & Beekman 2004*a*, Ziegler et al. 2004) can be achieved with iterative methods incorporating noise models, known as statistical reconstruction (SR) algorithms.

In order to achieve improved image quality, iterative methods rely on accurate modeling of the scanning process. Projections are usually simulated by tracing straight rays through a voxelized representation of the object. Since a voxel is often modeled as a cube with constant density, the resulting simulated projections are always smoothed relative to the actual projections of the real, continuous object. As we have explained in Zbijewski & Beekman (2004*a*), iterative algorithms often attempt to compensate for this inappropriate smoothing by introducing spurious, high–valued voxels on the sharp edges. This pollutes iteratively reconstructed X-ray CT images with overshoots and interference–like patterns. To eliminate these artefacts, the discretization-induced smoothing has to be avoided. This can be accomplished by performing the reconstruction on a very fine grid, followed by down-sampling to a commonly used voxel size or by slight post-filtering of the resulting image to reduce the noise. We have shown that this method is more effective in reducing the edge artefacts than post-filtering of the reconstructions performed on coarser grids. Reconstruction on a fine grid leads to almost complete removal of the artefacts with no loss of resolution, whereas post-filtering of reconstructions requires a large degree of smoothing in order to significantly reduce the edge overshoots and the aliasing patterns.

An alternative way of suppressing the edge artefacts is to force the algorithm to accept some amount of smoothing in the final reconstruction. This reduces the reconstruction problem to estimating only a blurred version of the real object. This approach has been put forward by Snyder an co-workers in their classic paper on edge and noise artefacts in emission tomography (Snyder et al. 1987). Since the system model investigated in Snyder et al. (1987) was based on simple Gaussian projection kernels, the method proposed there cannot be directly applied to X-ray CT reconstruction based on ray-tracing. In this case, the most straightforward way to constrain IR to a blurred version of the object is to smooth the measured projections prior to reconstruction. In this way, a match between real and simulated projections can be achieved without the introduction of any edge overshoots or aliasing patterns. Similar observations have recently been made by Kunze et al. (2005), without however a detailed analysis of resolution losses induced by the smoothing or a comparison with other edge artefact reduction strategies.

Another potential way to mitigate the edge artefacts may lay in using image representations different than conventional voxels. A promising example of such an alterative set of base functions are the so-called blobs. In this case an image is composed as a sum of spherically symmetric Kaiser-Bessel functions centered at each grid point and scaled by the image value at this point (Lewitt 1990, Matej & Lewitt 1996). Attractive properties of blob base functions include the fact that they are nearly band-limited and that their line integrals do not depend on integration angle, but only on the distance from blob's center. The exact functional form of this dependence is known and can therefore be precomputed prior to the reconstruction. Extensive studies have been performed to compare the performance of blob- and voxel-based IR for the case of PET data (Matej & Lewitt 1996). For a fixed value of contrast recovery coefficient, blobs have been

shown to provide lower reconstruction noise levels than voxels. Moreover, whenever edge artefacts were present, their appearance in blob representation was more uniform and more localized than when voxels were used. This indicates that a change in the image representation used will most probably not obviate the main reason for the occurrence of edge artefacts, ie. the erroneous blurring of simulated projections. It may, however, influence the appearance of the artefacts in the reconstructed image and thus also the ability to remove them by eg. further post-filtering. It is therefore interesting to investigate how the observations made for blob-based reconstructions in PET imaging transfer to the case of X-ray CT. Blobs have already been used with some success for iterative X-ray CT reconstruction (Mueller et al. 1999*a*, Mueller et al. 1999*b*, Ziegler et al. 2004), but, to our best knowledge, their performance with respect to edge disturbances has never been assessed.

The goal of the present paper is to compare the effectiveness of edge artefact reduction achieved by (i) reconstruction on a fine grid, (ii) blurring the projections and (iii) the use of blob-based image representations. For the case of artefact removal by blurring the measured projections, a whole range of pre-reconstruction filters is applied to simulated projection data and the trade-offs between image resolution and the degree of artefact reduction are assessed visually and numerically. Similar trade-offs are examined for blob-based reconstructions post-filtered with a set of Gaussian kernels.

3.2 Methods

This section describes in details the artefact suppression methods and the simulation studies used for their evaluation.

3.2.1 Simulations

A fan–beam system with distance from source to detector of 1000 mm and a magnification factor of 2 was simulated. The projection data contained 1000 views, acquired over $360\,^{\circ}$; the detector consisted of 500 projection pixels (pixel width: 2 mm). A ray-tracer based on Siddon's algorithm (Siddon 1986) was used for the simulation. The phantom was constructed on a 4096x4096 square matrix (voxel size: 125 μm) and the number of rays traced per detector element was set to sixteen. This simulation grid was four times denser than the grid employed for the reconstruction; the fine voxelization used is proven to be more than sufficient to make an adequate estimate of real density distributions (Goertzen et al. 2002).
Six noise realizations of projections were generated according to Poisson distribution. The blank scan intensity was set to 10^6 photons per detector cell. For water, a constant attenuation factor of 0.168 cm^{-1} was assumed.

A mathematical abdomen phantom (Fig. 3.1, Schaller (1999)) was used for the simulations. The lengths of the phantom axes were 400 mm and 240 mm. For the assessment of image resolution, three 0.5 mm wide line–shaped patterns with a contrast of +500 HU were placed in the phantom.

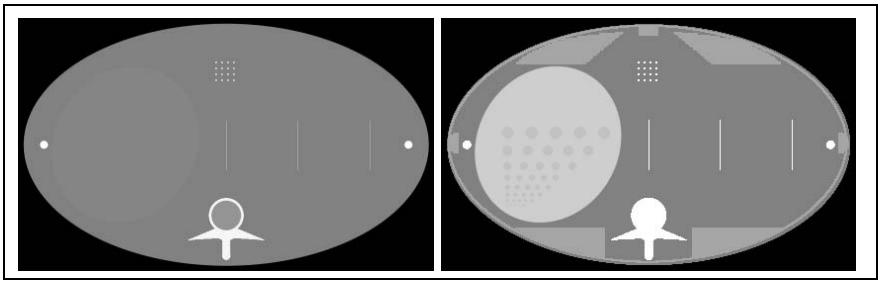

Figure 3.1: Slice of the modified Schaller abdomen phantom. Left: full gray–scale. Right: 0.9–1.1 $\frac{g}{cm^3}$ scale, with the regions used for mean error calculations superimposed.

3.2.2 Reconstruction

Forty iterations of the Ordered Subsets Convex algorithm (OSC, Kamphuis & Beekman (1998*a*), Beekman & Kamphuis (2001), Kole & Beekman (2005*a*)) with 125 subsets were used. Such a relatively large number of iterations is required to suppress streak artefacts around the circular objects modeling the ribs (Zbijewski & Beekman 2004*c*) [1].

For the reconstructions based on the voxel-based representation, both the forward and the back-projector employed were based on Siddon's algorithm and were identical to the ray-tracer used for the simulation; a sub-sampling of four rays per detector pixel was utilized. The target resolution of the reconstruction was set to 512x512 voxels (voxel size: 1 mm). The OSC result obtained directly on this grid will be referred to as $OSC–NOFOLD$.

In a blob-based representation, the object is composed as a superposition of blobs centered at each point of a cubic grid and scaled by the value of reconstruction at this point. A 512x512 image grid was used in this study, the distance between grid points was 1 mm. The final images were obtained by convolving the reconstructed grid values with the Kaiser-Bessel function used as the base for image representation. Projection and back-projection in blob-based reconstructions were performed using ray-driven splatting (Mueller et al. 1999*b*). In this method, rays are traced through the volume and for each ray-blob intersection the distance is determined from the intersection point to the center of a blob. Based on this distance, appropriate value of ray integral is retrieved from a pre-computed table. The table samples the analytical formula for a line integral of a blob at 1000 radial points located between 0 and the total radial extent of a blob.

For comparison, reconstructions were also obtained with the commonly used Filtered Back-Projection (FBP) algorithm. CTSim 3.5 package (Rosenberg 2002) was used. A ramp filter with a cutoff at the Nyquist frequency was employed; the image grid was 512x512 voxels.

[1] These artefacts can be removed by FBP-initialization (Zbijewski & Beekman 2004*c*). This technique was not used in the present study because we wanted to separate clearly the effects of different edge artefact reduction methods from the effects of FBP initialization.

3.2.3 Artefact suppression methods

The first method attempts to reduce the artefacts by performing the reconstruction on a fine grid. In this study, a 1024x1024 grid (voxel size: 0.5 mm) was employed. The OSC reconstructions obtained at this resolution were down-sampled to the target resolution of 512x512 voxels by adding together assemblies of four voxels. The results will be denoted by $OSC\text{–}FOLD_{\,1024}$.

The second method under consideration attempts to reduce the artefacts by blurring the input projections. The choice of blurring kernel determines the performance of this approach. An optimal filter should exactly match the smoothing of the simulated projections caused by discretization errors. However, it is difficult to find a blurring kernel that will guarantee such an exact match. This task is especially troublesome for systems with divergent beams; in such systems the extent of blurring depends on the distance from the source. We have therefore chosen to analyze a whole range of filters obtained by varying the width of a Gaussian kernel. This basic filter shape provides a very general blurring function and by varying its size one should at some point achieve close agreement with the complex smoothing introduced by ray-tracing in a fan beam geometry. The Full Widths at Half Maximum (FWHM) of the Gaussian kernels used for pre-reconstruction filtering of the input projections varied from 1 to 5 detector pixels (2 to 10 mm), their size being always 20 times the standard deviation. Two methods of blurring were investigated. In the first one, the intensity values were logarithmically transformed into line integrals prior to blurring. After the smoothing, the line integrals were transformed back into the intensity space. The set of reconstructions obtained in this way will be referred to as $OSC\text{–}GAUSS$. For comparison, the smoothing was also performed directly on the intensity values. The reconstructions obtained will be further denoted as $OSC\text{–}GAUSS_{\,NOLOG}$.

The third artefact reduction method under consideration represents images using a basis of Kaiser-Bessel functions (blobs) instead of voxels. The Kaiser-Bessel functions are given by the following formula (Lewitt 1990, Matej & Lewitt 1996):

$$\begin{array}{lcll} b_{m,a,\alpha}(r) & = & \frac{1}{I_m(\alpha)}\left(\sqrt{1-(\frac{r}{a})^2}\right)^m I_m\left(\alpha\sqrt{1-(\frac{r}{a})^2}\right) & 0 \le r \le a \\ b_{m,a,\alpha}(r) & = & 0 & r > a \end{array} \tag{3.1}$$

where I_m is a modified Bessel function of order m, a represents the radius of a blob and α is a taper parameter determining the blob's shape. The interplay of the three free parameters describing a Kaiser-Bessel function is crucial for the quality of reconstruction. The value of m determines the continuity of a blob and its derivatives when its argument approaches a. The value of m should be at least equal to two, so that the associated Kaiser-Bessel function is continuous at least up to its first derivative. The extent of a blob is determined by the radius a. It should be small enough to guarantee that the FWHM of a blob is lower or equal to the FWHM of the imaging system, so that aliasing is minimized. Finally, the taper parameter influences the magnitude of the side-lobes of a Kaiser-Bessel function, thus determining the blob's ability to reduce aliasing. The combination of all three parameters of a blob should ensure that the spectrum of a blob is identically zero at the sampling frequency of a grid and close to zero at other multiplies of the sampling frequency. This criterion (further referred to as the minimization of representation error) guarantees that a superposition of blobs will provide a good representation of a constant function. For Kaiser-Bessel functions such representation will never be ideal, but, as shown in Matej & Lewitt (1996), its error can be made negligible if a, m and α are carefully selected.

In the current study, two shapes of blobs were tested. In the latter, $OSC\text{–}BLOB_{STD}$ denotes reconstructions performed using a Kaiser-Bessel function with $m = 2$, $a = 2$ (expressed in units of grid spacing) and $\alpha = 10.83$. A blob described by this combination of parameters will be denoted as a "standard" blob. It has been proven to work well for PET reconstruction (Matej & Lewitt 1996) and has also been frequently and successfully applied to X-ray CT data (Mueller et al. 1999*a*, Mueller et al. 1999*b*, Ziegler et al. 2004). A standard blob fulfills the minimization of representation error criterion and has a FWHM equal to 1.31 of grid spacing. In addition, a basis composed of narrower Kaiser-Bessel functions having a FWHM of 1.17 of grid spacing has been tested. A narrower blob may provide a better model for steep edges than the standard one. On the other hand, despite the fact that the narrow blob fulfills the representation error criterion, its error of representation of constant image is larger than for a standard blob (Matej & Lewitt 1996). The narrow blob parameters are: $m = 2$, $a = 1.5$ and $\alpha = 6.94$. The associated reconstructions will be denoted as $OSC\text{–}BLOB_{NARROW}$.

3.2.4 Noise and resolution measurements, quantitation of the artefacts

In order to compare the artefact reduction methods quantitatively, the following measures were used:

- *Noise.* For each of the methods analyzed, a set of six reconstructions obtained from different noise realizations of projection data was considered in order to ensure that the noise measurement was not biased by the non–uniformities in the reconstruction. For each possible pair of reconstructions from such a set, the images forming the pair were subtracted and the variance (σ^2) in a region covering the liver was computed for the resulting difference image. The final numerical estimate of the noise (understood as the standard deviation of a signal in an uniform area) was obtained by taking the square root of half of the average variance in all difference images:

$$\text{Noise} = \sqrt{\frac{1}{K}\sum_{i}^{K}\frac{\sigma_i^2}{2}} \tag{3.2}$$

  where K is the number of difference images.

- *Resolution measurement.* The FWHM was determined for each of the three line objects. Prior to the calculation of the FWHM, the background surrounding the line objects was removed by subtraction of a noiseless reconstruction performed without the line pattern. The values of the resolution cited in the sequel are averaged over the three lines.

- *Quantification of the artefacts.* Noise–free projections were reconstructed using all the methods under investigation. In order to facilitate comparisons over a range of image resolution values, the reconstructions obtained with FBP, $OSC\text{–}NOFOLD$, $OSC\text{–}BLOB_{STD}$, $OSC\text{–}BLOB_{NARROW}$ and $OSC\text{–}FOLD_{1024}$ were post–filtered with a set of Gaussian kernels (with FWHM varying from 0 mm to 2 mm). Due to the initial blurring of projections, $OSC\text{–}GAUSS$ and $OSC\text{–}GAUSS_{NOLOG}$ also produce an ensemble of reconstructions that span a range of resolution values. For each value of image

resolution, the mean error in a union of image regions covering the most pronounced aliasing patterns (along the edge of the object, around the ribs and around the spine, Fig. 3.1 (b)) was computed. Mean error is defined as:

$$\text{ME(r)} = \frac{1}{N}\sum_{k}^{N} |\bar{\mu}(k) - \mu(r;k)| \tag{3.3}$$

where r represents image resolution, $\mu(r;k)$ refers to the value of voxel k in a reconstruction blurred down to the resolution r, N is the number of voxels in the region of interest and $\bar{\mu}(k)$ is the attenuation of voxel k in the phantom.

3.3 Results

Fig. 3.2 displays FBP reconstruction of the simulated, noisy projections of the abdomen phantom. In this and in the following figures the panels on the left display reconstructions of a single noise realization of the projection data (gray-scale: 0.9–1.1 $\frac{g}{cm^3}$). In the panels on the right a compressed 1.0–1.02 $\frac{g}{cm^3}$ scale (meant to emphasize the artefacts) is used to show the means of the images computed from six different noise realizations. FBP results in an image free of any edge artefacts. All the OSC reconstructions displayed in the sequel are presented either at equal

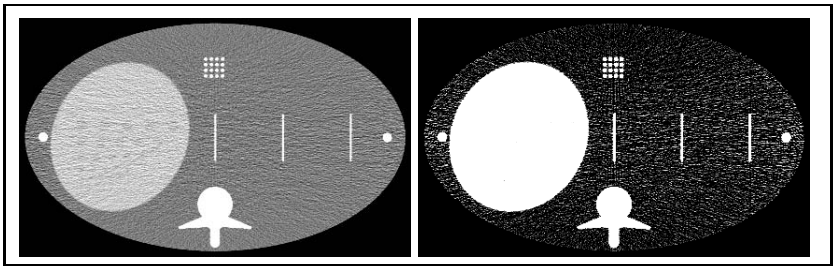

Figure 3.2: FBP reconstruction of the simulated abdomen phantom projections. The resolution of this image is 1.9 mm, the noise level 0.02 $\frac{g}{cm^3}$. Left: reconstruction from a single noise realization, 0.9–1.1 $\frac{g}{cm^3}$ gray scale. Right: mean of reconstructions obtained from different noise realizations, 1.0–1.02 $\frac{g}{cm^3}$ gray scale. FBP reconstructions are free of any edge disturbances.

noise or at equal resolution with this FBP image.

In Fig. 3.3 various iterative reconstructions, all displayed on a 512x512 grid, are compared at equal level of statistical noise. For OSC–$GAUSS$, a reconstruction of projections blurred with a Gaussian kernel having an FWHM of 1.3 detector pixels is presented. For other OSC results, a match with the noise level of the FBP image was achieved by smoothing the original reconstructions with a Gaussian kernel. Fig. 3.4 compares the same methods at equal resolution. In this case, OSC–$GAUSS$ with a kernel having an FWHM of 1.9 pixels was selected for display. The minor streaks emerging from the ribs in the OSC images are independent from the edge disturbances; they have been investigated in more details in Zbijewski & Beekman (2004*c*) and it has been shown that they can be prevented by FBP–initialization of the iterative algorithm.

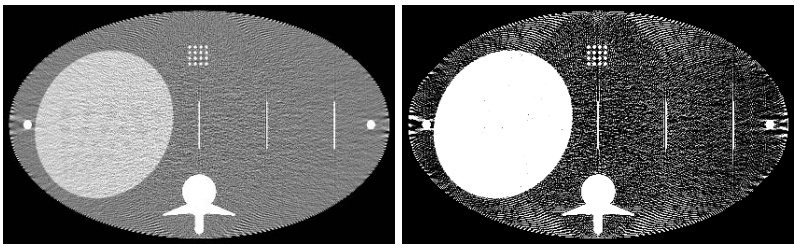

(a) OSC, 512x512 grid. Resolution: 1.3 mm. Noise: 0.02 $\frac{g}{cm^3}$

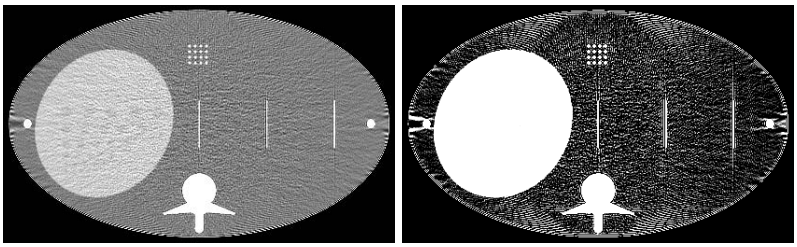

(b) OSC, 512x512 grid+std. blob. Resolution: 1.2 mm. Noise: 0.02 $\frac{g}{cm^3}$

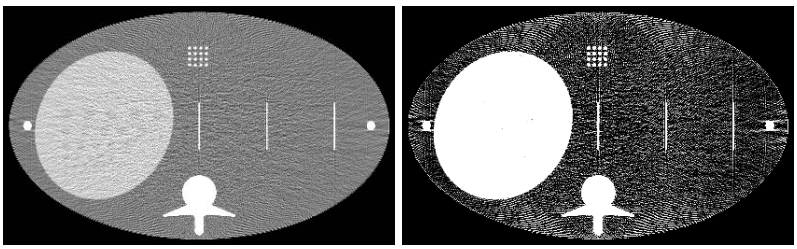

(c) OSC, 512x512 grid, filtered projections. Resolution: 1.4 mm. Noise: 0.02 $\frac{g}{cm^3}$

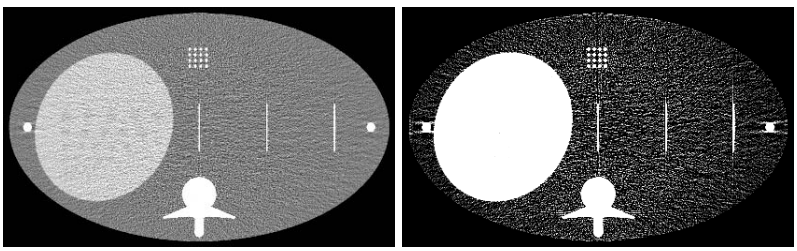

(d) OSC, folded from 1024x1024 grid. Resolution: 1.3 mm. Noise: 0.02 $\frac{g}{cm^3}$

Figure 3.3: Like the previous figure, but various statistical reconstruction approaches are compared at noise level equal to that of the FBP image. For OSC performed directly on a 512x512 grid (panel *a*), edge artefacts are strongly pronounced. Using standard blobs on a 512x512 grid results in only minor improvement (panel *b*). Filtering the projections also reduces the artefacts only slightly (OSC–$GAUSS$, panel *c*). Almost complete artefact removal is achieved with OSC–$FOLD_{1024}$ (panel *d*).

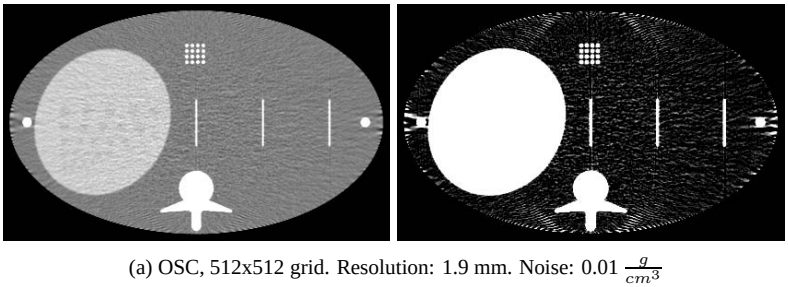

(a) OSC, 512x512 grid. Resolution: 1.9 mm. Noise: 0.01 $\frac{g}{cm^3}$

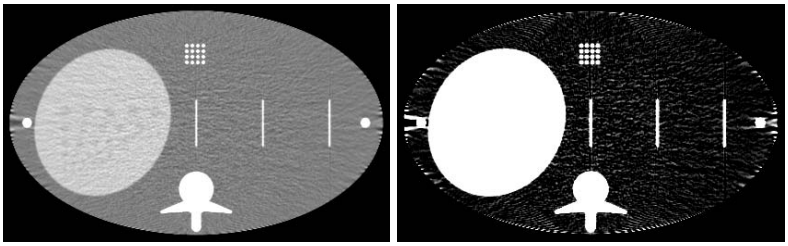

(b) OSC, 512x512 grid+std. blob. Resolution: 1.9 mm. Noise: 0.01 $\frac{g}{cm^3}$

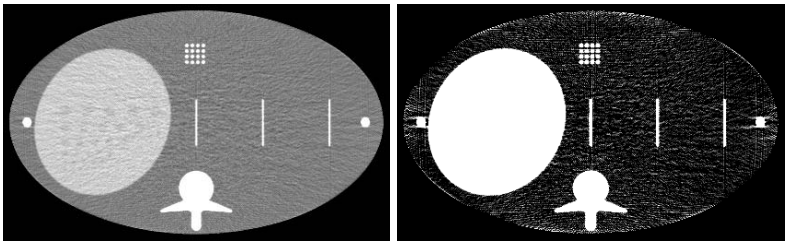

(c) OSC, 512x512 grid, filtered projections. Resolution: 1.9 mm. Noise: 0.01 $\frac{g}{cm^3}$

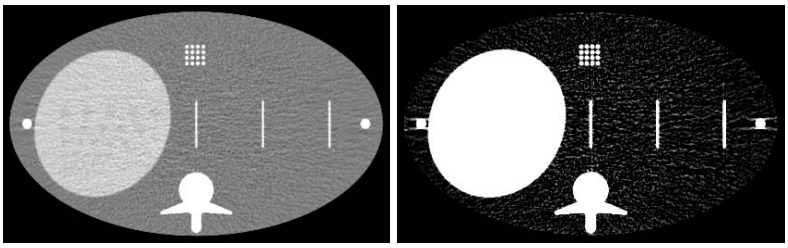

(d) OSC, folded from 1024x1024 grid. Resolution: 1.9 mm Noise: 0.01 $\frac{g}{cm^3}$

Figure 3.4: Like the previous figure, but with reconstructions compared at equal resolution. Edge and aliasing artefacts are still visible for OSC reconstruction performed directly on the 512x512 grid (panel *a*). Similar level of artefacts is seen in the reconstruction obtained with standard blobs (panel *b*) and in the reconstruction of blurred projections ($OSC–GAUSS$, panel *c*). The $OSC–NOFOLD$ reconstruction (panel *d*) exhibits almost no edge artefacts.

The images obtained using a blob-based representation on a 512x512 grid are presented in Fig. 3.3 *b* and Fig. 3.4 *b*. Compared to the voxel-based OSC performed using the same grid resolution (Fig. 3.3 *a* and Fig. 3.4 *a*), blob-based reconstructions exhibit some degree of artefacts reduction. The artefact suppression is most effective for the interference patterns protruding from the edge into the object. The edge overshoots itself are more pronounced for blobs than for the voxel-based representation. This indicates a more localized appearance of such disturbances in blob-based reconstructions and is in agreement with the results shown in Matej & Lewitt (1996). Fig. 3.3 *b* shows that $OSC\text{–}BLOB_{STD}$ achieves better resolution than $OSC\text{–}NOFOLD$ when compared at equal noise. This finding is also in agreement with Matej & Lewitt (1996).

When the projections are blurred prior to the reconstruction, a slight reduction in the artefact level can be perceived in the case of matching noise (Fig. 3.3 *c*). Even more filtering had to be applied to the projections to arrive at a reconstruction with resolution equal to that of the FBP image (Fig. 3.4 *c*). This filtering leads to a more significant reduction of the aliasing patterns. Compared to the results obtained for blob-based image representation, filtering the projections prior to reconstruction leads to images that are visually less disturbing. This is because for $OSC\text{–}GAUSS$ the artefact patterns are more evenly distributed over the edge and within its immediate neighborhood than for $OSC\text{–}BLOB_{STD}$. Neither method can however produce a result that would be much better than the reduction achieved with $OSC\text{–}NOFOLD$. $OSC\text{–}FOLD_{1024}$ clearly outperforms all the other artefact suppression techniques.

Fig. 3.5 analyzes a trade-off between the image resolution and the error magnitude. Blurring

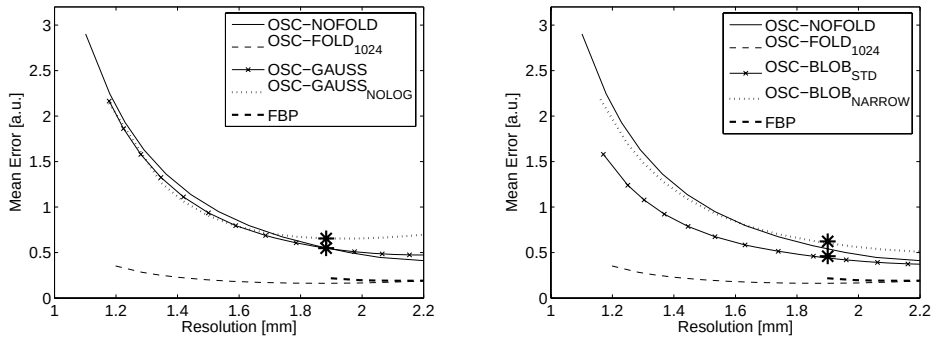

(a) (b)

Figure 3.5: Mean error in the regions containing the strongest aliasing patterns plotted as a function of image resolution. In panel *a*, $OSC\text{–}FOLD_{1024}$, $OSC\text{–}NOFOLD$ and FBP are compared with the method based on blurring the measured projections prior to reconstruction ($OSC\text{–}GAUSS$ and $OSC\text{–}GAUSS_{NOLOG}$). Stars mark the reconstructions depicted in Fig. 3.6. Panel *b* presents the performance of blob-based OSC ($OSC\text{–}BLOB_{STD}$ and $OSC\text{–}BLOB_{NARROW}$), stars mark the reconstructions displayed in Fig. 3.7.

the projections prior to reconstruction leads to only a minor improvement over the post-filtering of the reconstructions. Blob-based reconstruction achieves lower total value of ME when compared at equal resolution with $OSC\text{–}GAUSS$, but the difference between the two methods

diminishes as the resolution is decreased. The only method that resulted in successful artefact reduction over the whole range of resolutions is $OSC\text{–}FOLD_{1024}$. It is interesting to note that, according to Fig. 3.5, the values of Mean Error for $OSC\text{–}GAUSS$ and $OSC\text{–}BLOB_{STD}$ reconstructions displayed in Fig. 3.3 are actually equal.

Fig. 3.5 *a* shows also the trade-off between artefact strength and resolution for the $OSC\text{–}GAUSS_{NOLOG}$, where the blurring of projections is performed directly on the intensity data. For small blurring kernels this method behaves similarly to $OSC\text{–}GAUSS$. For larger filters it exhibits some increase in the value of mean error, reaching values larger than for $OSC\text{–}NOFOLD$. Similar behavior might be observed for $OSC\text{–}GAUSS$, although instead of increase, the error value seems to reach a plateau for broad smoothing kernels. In Fig. 3.6 reconstructions obtained with $OSC\text{–}GAUSS$ and $OSC\text{–}GAUSS_{NOLOG}$ are compared at equal resolution (corresponding to points marked with stars in Fig. 3.5). Both methods provide a sim-

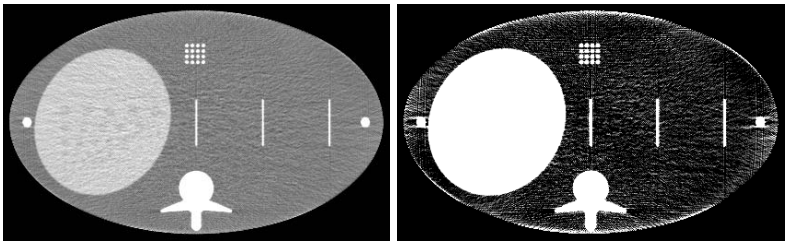

(a) $OSC\text{–}GAUSS_{NOLOG}$. Resolution: 1.9 mm. Noise: 0.01 $\frac{g}{cm^3}$

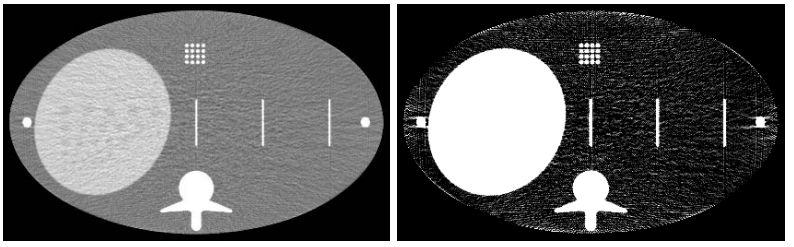

(b) $OSC\text{–}GAUSS$. Resolution: 1.9 mm. Noise: 0.01 $\frac{g}{cm^3}$

Figure 3.6: Like Fig. 3.4, but here a reconstruction obtained after filtering the projections directly in the intensity space ($OSC\text{–}GAUSS_{NOLOG}$, panel *a*) is compared to the one obtained by filtering in the line integral domain ($OSC\text{–}GAUSS$, panel *b*, same image as in Fig. 3.4 *c*). Both images have similar resolution and noise, but $OSC\text{–}GAUSS_{NOLOG}$ reveals increased intensity of the edge artefacts.

ilar degree of artefact removal inside the phantom, but when filtering is performed directly in the intensity domain, additional overshoots emerge at the edges of the phantom. This explains the increase in the Mean Error value for $OSC\text{–}GAUSS_{NOLOG}$ that can be seen in Fig. 3.5.

In panel *b* of Fig. 3.5, a curve representing the Mean Error achieved by OSC employing a base of narrow blobs is also presented. Compared to $OSC\text{–}BLOB_{STD}$, $OSC\text{–}BLOB_{NARROW}$ results in much worse artefact reduction. Fig. 3.7 displays the reconstructions obtained with narrow and standard blob. The resolution of both images is equal. $OSC\text{–}BLOB_{NARROW}$

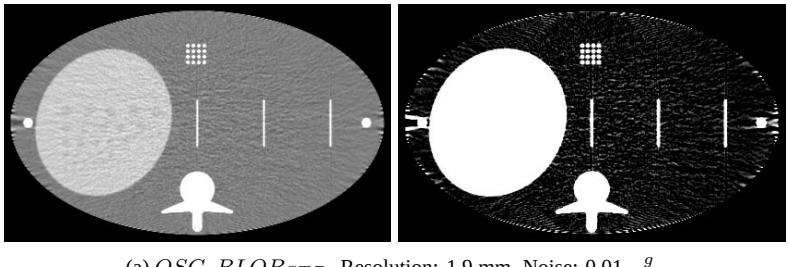

(a) $OSC–BLOB_{STD}$. Resolution: 1.9 mm. Noise: 0.01 $\frac{g}{cm^3}$

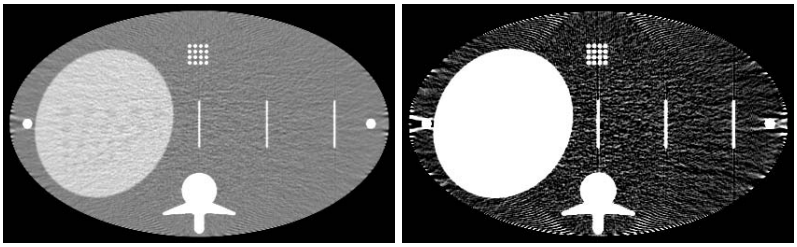

(b) $OSC–BLOB_{NARROW}$. Resolution: 1.9 mm. Noise: 0.01 $\frac{g}{cm^3}$

Figure 3.7: Like Fig. 3.4, but here OSC reconstructions employing two different blob shapes are compared. Panel *a* displays image computed with $OSC–BLOB_{STD}$, panel *b* demonstrates a reconstruction obtained using a blob narrower than the standard one. While both images have similar noise level and resolution, $OSC–BLOB_{NARROW}$ exhibits more pronounced edge artefacts than $OSC–BLOB_{STD}$.

is indeed polluted by artefacts that are much more visible than for $OSC\text{–}BLOB_{STD}$. It also exhibits some overall bias in the reconstructed attenuation values.

3.4 Discussion

A comparison has been made between various methods of reducing edge and aliasing artefacts in statistical X-ray CT reconstruction. The method based on reconstruction on a fine grid leads to almost complete removal of the artefacts with no significant loss of resolution. In contrast, when the projections are blurred prior to reconstruction, the amount of smoothing required to achieve a significant artefact reduction leads to images with a resolution lower than that attained by FBP and by reconstruction on a fine grid. Similarly, when blobs are used as the image basis and the reconstruction grid is kept at a lower resolution, only a slight artefact reduction is achieved compared to the case of voxel basis and the same grid spacing. Again, significant amount of blurring is needed to reduce the level of artefacts in blob-based reconstruction to a level similar to that attained by FBP.

For the method based on blurring the projections it is worth noting that if the blurring is performed directly on intensity values, instead of first converting them into line integrals, additional edge overshoots emerge in the reconstructions. This phenomenon occurs for large widths of the blurring kernel and is most probably a result of the inconsistencies that strong filtering introduces into the set of intensity measurements. Such behavior was much less pronounced when the intensity values were logarithmically transformed into line integrals prior to blurring. In this case, the reconstructions followed a very similar trend in terms of the trade-off between artefact reduction and resolution as the post-filtered reconstructions of original projections.

When blobs are used to represent the images, care has to be taken to properly select their parameters. Narrow blobs seem to be preferable because they provide better intrinsic resolution. In this study we have compared a frequently used "standard" blob to a narrower one. Our results show that the reconstructions obtained with the narrow blob exhibit some overall bias and contain more visible artefacts than $OSC\text{–}BLOB_{STD}$. A plausible explanation for this result is that the narrow blob yields larger representation errors for uniform images than the standard blob (Matej & Lewitt 1996). Another important characteristic of blob-based reconstruction is the fact that it produces more localized edge artefact patterns than a voxel-based approach. Images obtained with $OSC\text{–}BLOB_{STD}$ and images reconstructed from blurred projections may have the same overall value of Mean Error in the areas polluted by edge artefacts, but the artefacts will be more visually disturbing for the blob-based case due to their concentration in a smaller area.

An important practical consideration are the computational demands of the various algorithms investigated in this paper. In two dimensional case, the computation time associated with ray-tracing is roughly proportional to the linear size of the image matrix. The penalty for using $OSC\text{–}FOLD_{1024}$ is therefore a two-fold increase in the reconstruction time as compared to $OSC\text{–}NOFOLD$ or $OSC\text{–}GAUSS$ (the time spent on blurring the projections is negligible compared to the reconstruction time). Computation of projections for the case of blob-based image representation is heavily influenced by the radial extent of a blob. The size of a blob dictates the amount of overlap between the basis functions and thus the number of blobs crossed by every ray. In our implementation, reconstructions based on the standard blob and running on a

512x152 grid were approximately 1.8 times slower than voxel-based computations on the same grid. This timing is similar to that for $OSC\text{–}FOLD_{1024}$, but the latter approach provides better artefact reduction than $OSC\text{–}BLOB_{STD}$. Since reconstruction on a fine grid seems to be the only method that results in complete edge artefact removal, effective methods have to be sought to offset the increase in the reconstruction time caused by this approach. This can be achieved by a combined use of software and hardware acceleration methods: Ordered Subset reconstruction with huge numbers of subsets (Hudson & Larkin 1994, Beekman & Kamphuis 2001, Kole & Beekman 2005*a*), parallelization (Kole & Beekman 2005*b*) and the use of graphic cards for performing the projection and back-projection (Mueller & Yagel 2000, Kole & Beekman 2006). Growing interest of CT manufacturers in iterative reconstruction methods may also result in development of dedicated electronics that will facilitate clinically acceptable computation times.

3.5 Conclusions

We have found that reconstruction on a fine grid followed by down-sampling of the resulting image is more effective in reducing the edge artefacts than blurring the projections prior to reconstruction or using a blob-based image representation. Only by reconstruction on a fine grid one can almost completely remove the artefacts and at the same time retain the major advantage of statistical reconstruction over the analytical methods, namely its superior noise-resolution trade-off.

Chapter 4

Suppression of intensity transition artefacts in statistical X–ray CT reconstruction through Radon Inversion initialization

Abstract

Statistical reconstruction (SR) methods provide a general and flexible framework for obtaining tomographic images from projections. For several applications SR has been shown to outperform analytical algorithms in terms of resolution–noise trade–off achieved in the reconstructions. A disadvantage of SR is the long computational time required to obtain the reconstructions, in particular when large data sets characteristic for X–ray CT are involved. As was shown recently, by combining statistical methods with block iterative acceleration schemes (e.g. like in the Ordered Subsets Convex (OSC) algorithm), the reconstruction time for X–ray CT applications can be reduced by about two orders of magnitude. There are, however, some factors lengthening the reconstruction process that hamper both accelerated and standard statistical algorithms to similar degree. In this simulation study based on monoenergetic and scatter–free projection data, we demonstrate that one of these factors is the extremely high number of iterations needed to remove artefacts that can appear around high–contrast structures. We also show (using the OSC method) that these artefacts can be adequately suppressed if statistical reconstruction is initialized with images generated by means of Radon Inversion algorithms like Filtered Back Projection (FBP). This allows the reconstruction time to be shortened by even as much as one order of magnitude. Although the initialization of the statistical algorithm with FBP image introduces some additional noise into the first iteration of OSC reconstruction, the resolution–noise trade–off and the contrast-to-noise ratio of final images are not markedly compromised.

4.1 Introduction

Statistical methods for tomographic reconstruction like Maximum Likelihood Expectation Maximization (ML-EM, Shepp & Vardi (1982), Lange & Carson (1984)) or the Convex algorithm (Lange 1990) take into account the statistical noise in the projection data. As a result they have the potential to reduce the noise in the reconstructed images compared to analytical techniques. Therefore SR seems to be perfectly suited to facilitate the reduction of the dose delivered to a patient during X–ray CT examination. This task is of profound importance, since computed tomography accounts for around 40% of the collective effective dose, delivered to the population during medical X–ray examinations (Shrimpton & Edyvean 1998, Hidajat et al. 2001). In addition, SR can incorporate accurately into the transition matrix the precise details of photon transport and of the emission process. This offers a possibility to obtain highly quantitative reconstructions, free of scattering and beam hardening artefacts. Statistical reconstruction is also flexible enough to be applied to a large variety of image acquisition geometries, since it requires no explicit expressions for inverse transforms.
The computation times required currently by SR are still long in comparison with analytical methods; each iteration of SR requires at least one projection and one backprojection operation through the reconstructed object, whereas analytical methods need only one backprojection preceded by relatively quick filtering to arrive at the final reconstruction. Despite that, the abovementioned benefits of the statistical reconstruction together with a constant increase in the computer speed and the development of powerful algorithmic acceleration techniques (Manglos et al. 1995, Kamphuis & Beekman 1998*a*, Nuyts et al. 1998, Erdo ğan & Fessler 1999, Beekman & Kamphuis 2001) have recently resulted in a renewal of interest in the appliance of SR to X–ray CT.
Several successful applications of SR in TCT reconstruction have already been reported, comprising the removal of beam hardening artefacts, contrast enhancement in low–count studies and axial resolution improvement (e.g Wang et al. (1998), Nuyts et al. (1998), De Man et al. (2000), De Man et al. (2001), Elbakri & Fessler (2002), Bowsher et al. (2002)). Nevertheless, with regard to clinical X–ray CT considerable work has still to be done in order to characterize issues such as reconstruction convergence and quality of the images obtained with SR; the behavior of iterative reconstructions depends strongly on the kind of imaging device they are applied to, as well as on the acquisition protocols used. Numerous thorough investigations have already been performed in connection with applications of SR in nuclear medicine, where statistical reconstruction algorithms clearly outperform direct inversion methods and are now the method of choice in clinical routine. There are, however, important differences between emission imaging performed with PET or SPECT and X–ray transmission CT. For PET and SPECT, the projection data are substantially noisier and have resolution that is an order of magnitude lower than in X–ray CT. As a result, when SR is applied to X–ray CT some reconstruction artefacts will become visible that are not perceivable in PET or SPECT.
This work aims at contributing to the characterization of SR in application to data representative for X–ray CT. It focuses on cases where high–contrast structures are present in the objects being reconstructed. We show that from such structures artefacts emerge, that disappear only after a huge number of iterations of the statistical algorithm. This leads to unacceptable long reconstruction times. It will be shown how initialization of SR with Filtered Back Projection (FBP) image suppresses these artefacts and significantly cuts down the number of iterations required

to arrive at an almost artefact–free reconstruction with noise properties identical to SR started from a uniform image.

4.2 Methods

The studies presented in this paper were based on simulated projections of an abdomen phantom. These projections were subsequently used as input data for reconstruction algorithms. Different ways of initializing the SR were compared. This section gives details concerning the generation of simulation data, reconstruction algorithms and data analysis procedures.

4.2.1 Simulation

Simulated projections of a central slice of a three–dimensional, mathematical abdomen phantom (Fig. 4.1, Schaller (1999)) were generated. The phantom axes lengths were 400 mm and 240

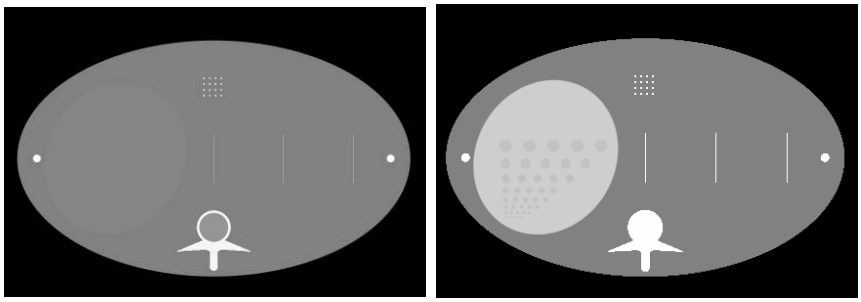

Figure 4.1: Slice of the modified Schaller abdomen phantom. Left: full gray–scale range. Right: compressed 0.9–1.1 scale.

mm. Low (10 HU) contrast circular lesions of varying size (diameters: 2 mm, 3 mm, 4 mm, 5 mm, 6 mm, 8 mm, 10 mm and 12 mm) were placed in a region modeling the liver. The ribs were modeled as two circular objects with a contrast of 1000 HU, situated on the long axis of the phantom.
For the assessment of image resolution, three 0.5 mm wide line–shaped patterns with a contrast of +500 HU were added to the phantom. Lines were placed equidistantly starting from the center of the object. For the estimation of small lesion contrast, a 4 by 4 grid of 2 mm squares with a contrast of +500 HU was placed in a uniform background area. The distance between the centers of the squares was 6 mm.
Transmission data for a fan–beam geometry were simulated by calculating the attenuation along rays through the object. The projection data contained 1000 views, acquired over $360\,^{\circ}$. The distance between source and detector was 1000 mm and the magnification factor was set to 2. The detector contained 500 projection pixels, each having a width of 2 mm. In order to emulate the fine resolution character of the transmission data, the phantom was discretized into a 4096x4096 square matrix with 125 μm voxels and the number of rays traced per detector

element was set to sixteen. This simulation grid is four times denser than the grid employed for the reconstruction (see also Sec. 4.2.2); the voxelization used is proven to be more than sufficient to make an adequate estimate of real density distributions (Goertzen et al. 2002). For noisy projections, discretization errors are adequately removed from the reconstructed images already when the phantom grid is two times finer than the one used for reconstruction and when four rays are traced per detector unit.
Poisson noise was generated in the simulated projections assuming 10^6 photons per detector in an unattenuated X–ray beam. This corresponds to the intensities used in clinical practice (Guan & Gordon 1996). Eighteen projection data sets were generated with different realizations of noise. For water, a constant attenuation factor of 0.168 cm $^{-1}$ was assumed.

4.2.2 Reconstruction

Statistical reconstruction routines were based on the Ordered Subsets Convex algorithm (OSC). In this approach, the convex algorithm is combined with an ordered subsets method (analogous to proposed for emission tomography in (Hudson & Larkin 1994)) in order to speed up the computations. In OS reconstructions, only a subset of projections at the time is employed for updating of the image estimate, and this update together with a different subset of projections is then used for calculating the next update. By definition, *an entire iteration n of OSC is completed when all subsets have been processed once*; this takes roughly the same processing time as one iteration with the standard convex algorithm. The OSC algorithm updates all estimates of the attenuation coefficients $\mu^n_{s+1}(k)$ (with k the voxel number in the object, n the iteration number and $s+1$ the subset number) according to:

$$\mu^n_{s+1}(k) = \mu^n_s(k) + \mu^n_s(k) \frac{\sum_{i \in S(s)} l_{ik} \left(\bar{y}_i(\mu^n_s) - Y_i\right)}{\sum_{i \in S(s)} l_{ik} \left\langle l_i, \mu^n_s \right\rangle \bar{y}_i(\mu^n_s)} \tag{4.1}$$

where the *expected* number of counts $\bar{y}_i(\mu^n_s)$ in detector bin i is given by

$$\bar{y}_i(\mu^n_s) = d_i \, e^{-\langle l_i, \mu^n_s \rangle} \text{ and } \langle l_i, \mu^n_s \rangle = \sum_j l_{ij} \, \mu^n_s(j). \tag{4.2}$$

In Eq. (4.1) and Eq. (4.2), Y_i represents the measured transmission counts in bin i, d_i represents the blank scan counts in bin i, l_{ij} is the length of projection line i through voxel j, and $S(s)$ contains the projections in subset s.
For X–ray CT the reduction in the computation time achieved with OSC can be as much as two orders of magnitude. The visual appearance of the images obtained, as well as their resolution–noise and contrast–noise tradeoff remain the same as for the standard Convex algorithm (Beekman & Kamphuis 2001). In the present study OSC with 125 subsets was employed for the reconstruction. The following initializations for OSC were compared: (i) with a uniform ellipse with diameters slightly larger than the diameters of the phantom, (ii) with an FBP reconstruction incorporating a Hanning filter with a cutoff at the Nyquist frequency of the detector system (Fig. 4.2, left), (iii) like (ii) but with a cutoff at 0.7 of the Nyquist frequency (Fig. 4.2, center) and (iv) like (ii) but with a cutoff at 0.3 of the Nyquist frequency (Fig. 4.2, right). In the sequel these reconstructions will be referred to as : $OSC\text{–}UNIF$,

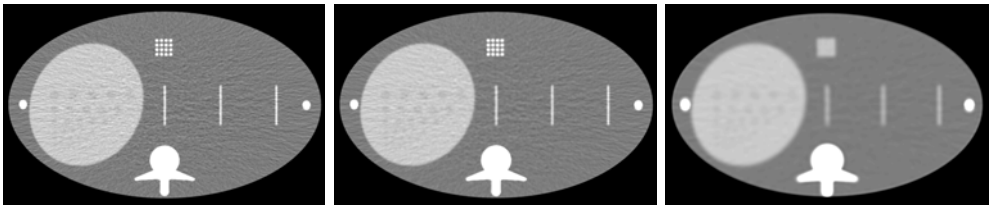

Figure 4.2: FBP reconstructions used for the initialization of statistical reconstruction. Left: FBP with a cutoff set to the Nyquist frequency of the detector system ($OSC–FBP_N$). Center: FBP with a cutoff set to 0.7 of the Nyquist frequency ($OSC–FBP_{0.7}$). Right: FBP with a cutoff set to 0.3 of the Nyquist frequency ($OSC–FBP_{0.7}$). The gray–scale is 0.9–1.1

$OSC–FBP_N$, $OSC–FBP_{0.7}$ and $OSC–FBP_{0.3}$, respectively. The software used for the generation of FBP images was based on the CTSim 3.5 package (Rosenberg 2002).
SR was performed on a 1024x1024 voxels grid with a subsampling of 4 rays per detector pixel during the ray–tracing. Afterwards, assemblies of four reconstruction voxels were added together to fold the image to the granularity of 512x512 voxels. During the statistical reconstruction the use of a dense discretization is essential to suppress edge artefacts that appear when the computational grid is relatively coarse (i.e. when it has a resolution comparable to the resolution that would be used for FBP, Zbijewski & Beekman (2004*a*)).

4.2.3 Assessment of image quality

The following measures were utilized to quantify the accuracy of the images and to facilitate comparisons :

- *Noise measurement*. For each initialization method analyzed, the set of reconstructions obtained consisted of eighteen images, each calculated from a different noise realization of the projection data. For each possible pair of reconstructions from such a set, the images forming the pair were subtracted. Then, the standard deviation in a region covering the liver was computed for each of the resulting difference images:

$$\mathrm{SD}_i = \sqrt{\frac{\sum_k^N \tilde{\mu_i}^d(k)^2}{N-1}} \tag{4.3}$$

  where N is the total number of voxels in the region of interest and $\tilde{\mu_i}^d(k)$ represents the value of voxel k in the i-th difference image. Finally, the standard deviations were averaged over all difference images to produce the final numerical estimate of the noise:

$$\mathrm{Noise} = \frac{1}{K}\sum_i^K \frac{\mathrm{SD}_i}{\sqrt{2}} \tag{4.4}$$

  where K is the number of difference images. In this way we ensured, that the noise measurement was not biased by the non–uniformities in the reconstruction.

- *Resolution measurement using the high intensity line-shaped objects.* For each of the three line objects placed in the phantom, the Full Width at Half Maximum (FWHM) was determined from a 30 mm wide profile drawn perpendicular to the line. Prior to the calculation of the FWHM, the background surrounding the line objects was removed from the reconstructed image by subtraction of a noiseless reconstruction performed without the line pattern. The FWHM for a single line in a single noise realization was calculated as follows: The profile was modeled as a set of lines connecting adjacent points that represented profile values. The FWHM is defined as the distance between the locations where these lines cross the half of maximum pixel value. Subsequently, FWHMs were calculated for all six images with different noise realizations and averaged. For further comparisons the mean resolution of the three lines is used.

- *Small object contrast* of the 16 squares in the block pattern were calculated for all six data sets with the six different noise realizations. The contrast is defined as

$$\text{Contrast} = \frac{|l - b|}{l + b} \tag{4.5}$$

  where l is the average pixel value in the square pattern and b is the average pixel value in a uniform region of 30 x 30 mm. The relative contrast is the contrast in the image divided by the contrast in the phantom. The values presented in the paper were averaged over different noise realizations.

- *Bias*. This measure is defined as the squared difference between the corresponding pixels in the mean of the reconstructions and in the original image:

$$\bar{\mu}(k) = \frac{1}{M} \sum_{i}^{M} (\tilde{\mu_i}(k)) \tag{4.6}$$

$$\text{Bias} = \frac{1}{N} \sum_{k}^{N} (\bar{\mu}(k) - \mu(k))^2 \tag{4.7}$$

  where $\tilde{\mu_i}(k)$ refers to the value of pixel k in the i-th noise realization of the reconstructions, M is the number of noise realizations, N is the number of pixels, $\bar{\mu}(k)$ is the mean image and $\mu(k)$ represents the attenuation value of the phantom. In this study, bias was computed over a region consisting of two 50x50 mm squares surrounding the two ribs.

- *Acceleration factor*. To asses the acceleration in artefact reduction achieved by using FBP–initialized OSC, the following procedure has been used:
  Iteration–bias curves were calculated for each of the OSC reconstructions. Then, for each iteration of FBP initialized OSC (denoted as I_{FBP}) the associated number of iterations of OSC–$UNIF$ required to achieve the same value of bias (denoted as I_{UNIF}) was estimated by linear interpolation. The acceleration factor is defined as:

$$\text{Acceleration} = \frac{I_{UNIF}}{I_{FBP} + 0.3} \tag{4.8}$$

The constant 0.3 in the denominator of equation (4.8) accounts for the computation time of the initial FBP reconstruction. It is roughly equal to the execution time of one backprojection step, which takes at most one third of an iteration of OSC (one iteration of OSC consists of one forward and two backprojections of all the projections). This is a very conservative estimate, because most implementations of FBP employ voxel–driven backprojectors that are considerably faster than the ray–driven backprojector used in OSC.

4.3 Results

4.3.1 Rapid transition artefact removal through FBP initialization

Fig. 4.3 (a) presents bias for the ribs area as a function of iteration number for differently initialized OSC reconstructions. In the whole range of iterations analyzed, the bias values for FBP–initialized statistical reconstruction are lower than for SR started form the uniform image. Consequently, FBP initialization reduces the number of iterations required to reach a given bias. At early iterations the scale of artefact suppression depends strongly on the amount of filtering in the start FBP image; $OSC\text{–}FBP_{0.7}$ is about 50% less effective in this respect than $OSC\text{–}FBP_N$.

Fig. 4.3 (b) quantifies the acceleration obtained by initializing OSC with the FBP reconstructions. As mentioned above, the upper bound estimate for the computation time of initial FBP reconstruction is taken into account in the calculation of the acceleration factor. Therefore the values of the acceleration presented here represent the lower bound estimate of this quantity. At early stages of reconstruction $OSC\text{–}FBP_N$ achieves a given bias almost an order of magnitude faster than $OSC\text{–}UNIF$. $OSC\text{–}FBP_{0.7}$ results in acceleration factor that is on average about 0.75 times lower than for $OSC\text{–}FBP_N$. The lowest acceleration is accomplished with $OSC\text{–}FBP_{0.3}$, which uses the most blurred FBP reconstruction for initialization.

Fig. 4.4 compares the images obtained after a single iteration of $OSC\text{–}UNIF$ (frame (a)), $OSC\text{–}FBP_{0.7}$ (frame (b)) and $OSC\text{–}FBP_N$ (frame (c)). These images support observations made earlier in this subsection; OSC initialized with the uniform ellipse produced reconstructions containing prominent streak artefacts around the ribs and the spine. Such artefacts are practically invisible in the reconstructions started from the FBP images. As the iterations proceed, one expects to find a slow reduction in the differences in the quality of images obtained by means of the two methods. In Fig. 4.5 the situation at late iterations (forty) of reconstruction is compared for $OSC\text{–}FBP_N$, $OSC\text{–}FBP_{0.7}$ and $OSC\text{–}UNIF$. All the reconstructions presented have similar noise and resolution (Fig. 4.6, region R) and are practically artefact–free. This demonstrates that the artefacts can indeed be suppressed solely by performing a very high number of OSC iterations. It is however more efficient to use FBP–initialized OSC, since then similar degree of artefact reduction can be achieved at earlier iterations of the reconstruction (cf. Fig. 4.3).

Very slight remnants of the streaks (appearing as horizontal bursts of higher attenuation value emerging from top and bottom of the rib) can still be perceived in all the images from Fig. 4.5. This may suggest, that (similar to FBP solutions) streaks are actually a part of the OSC solution and cannot be completely removed from reconstructions, even after many iterations of the FBP–initialized algorithm.

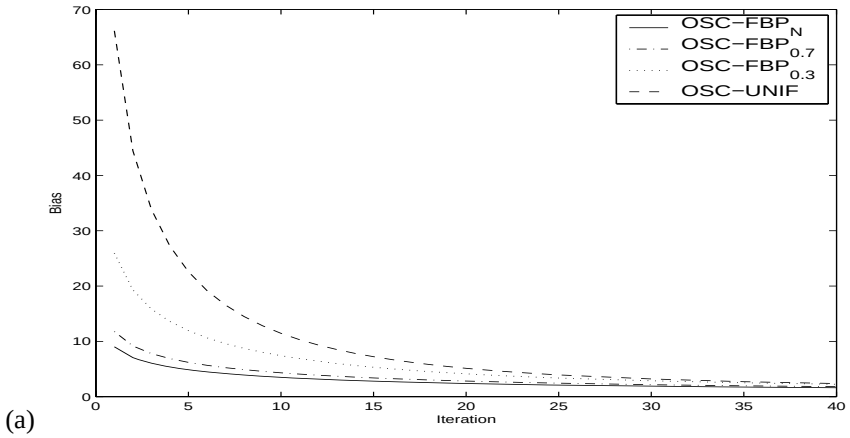

(a)

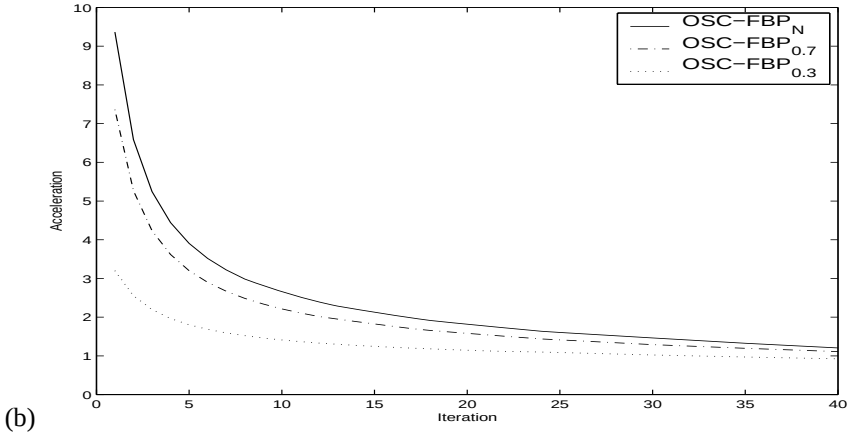

(b)

Figure 4.3: Frame (a) shows the bias in the area surrounding the ribs for differently initialized OSC. The reconstruction error is greatly reduced when the FBP image is used to start OSC. The scale of bias reduction depends on the degree of smoothing present in the initial FBP image. Frame (b) shows the acceleration factor as a function of iteration number for OSC initialized with noisy and blurred FBP images.

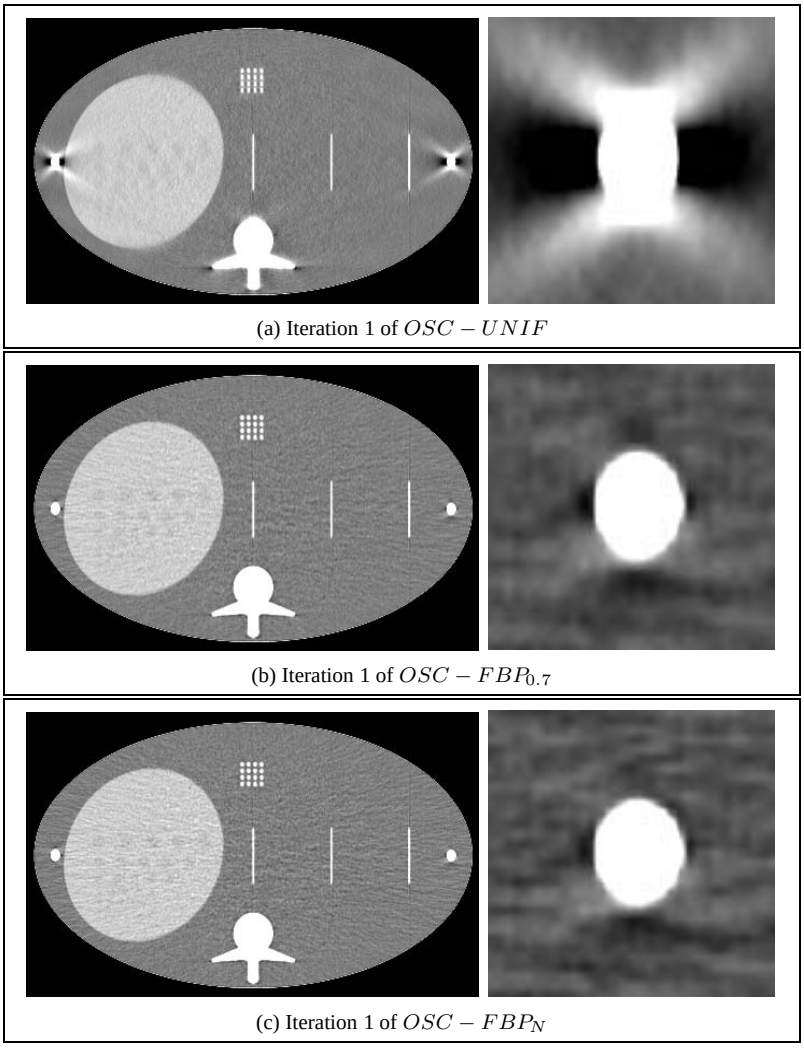

(a) Iteration 1 of $OSC - UNIF$

(b) Iteration 1 of $OSC - FBP_{0.7}$

(c) Iteration 1 of $OSC - FBP_N$

Figure 4.4: Reconstructions (whole object view and rib region) after one iteration of differently initialized OSC (corresponding to the region marked as P on Fig. 4.6). For OSC initialized with a uniform start image (Frame (a)), streaks emerging from ribs are clearly visible and other high–contrast structures of the object are yet not fully resolved. FBP–initialized OSCs (Frames (b) and (c)) produce images with streaks almost completely suppressed and high–contrast structures already well resolved. The gray–scale is 0.9–1.1 for the whole object view and 0.95-1.1 for the images of the rib region.

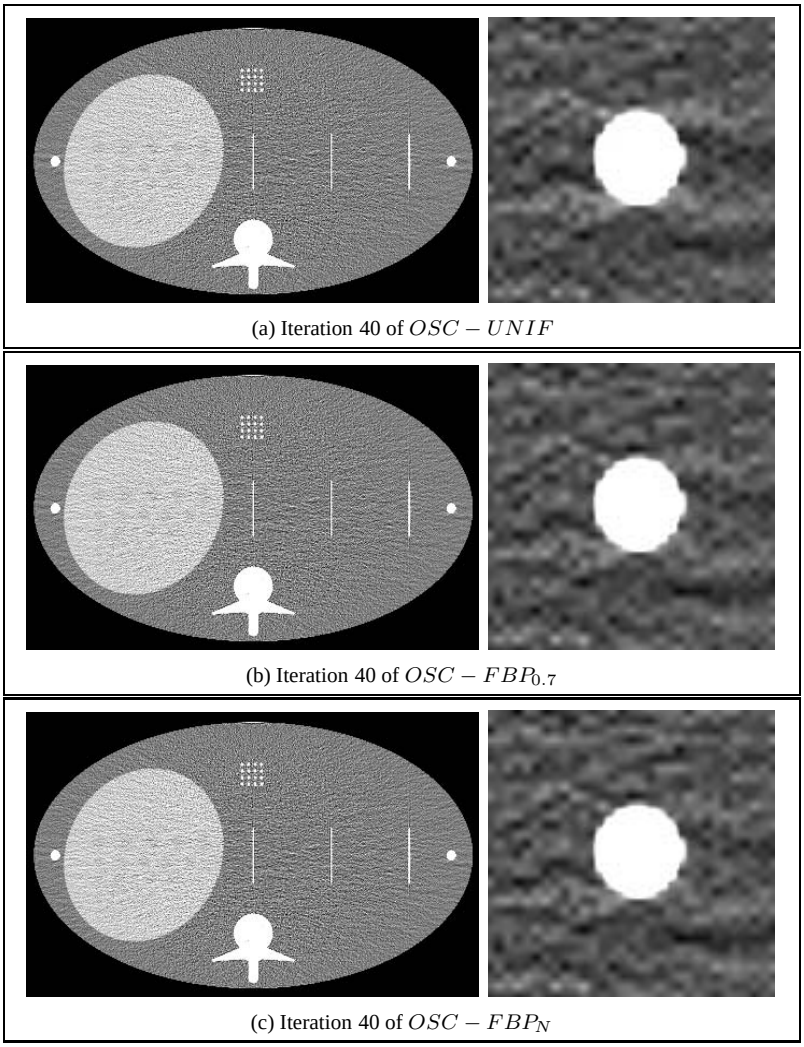

(a) Iteration 40 of $OSC - UNIF$

(b) Iteration 40 of $OSC - FBP_{0.7}$

(c) Iteration 40 of $OSC - FBP_N$

Figure 4.5: The 40th iteration of differently initialized OSC (corresponding to the region marked as R on Fig. 4.6), showing that all the initializations eventually converge to almost identical images with similar noise and resolution. The gray–scale is 0.9–1.1 for whole object view and 0.95-1.1 for the images of the rib region.

4.3.2 Noise properties of FBP–initialized OSC

Since a FBP—based start estimate injects noise into early iterations of the statistical algorithm, it had to be verified that the accelerated artefact reduction was not achieved at the price of compromised resolution–noise and contrast–noise trade–offs. Therefore, in Fig. 4.6 resolution– and contrast–noise relationships are presented for OSC initialized with the uniform ellipse and with the FBP reconstructions. When compared at equal resolution and at early iterations, OSC–FBP_N and OSC–$FBP_{0.7}$ generate images which are initially slightly noisier than the images produced with uniformly initialized OSC. This can be also verified by comparing the reconstructions presented in Fig. 4.4. However, after a couple of iterations OSC–FBP_N and OSC–$FBP_{0.7}$ attain almost identical tradeoff between resolution and noise as achieved by OSC–$UNIF$. Also the contrast–noise behavior of OSC–FBP_N and OSC–$FBP_{0.7}$ closely follows the behavior of OSC–$UNIF$. Simultaneously, (as shown in Fig. 4.3) these FBP–initialized OSCs have considerably lower bias in the rib area than the OSC–$UNIF$.
In Fig. 4.7 the situation near the convergence point of resolution–noise curves from Fig. 4.6 (region Q) is depicted. Reconstructions presented there do indeed appear visually very similar. However, OSC–$UNIF$ still results in strong artefacts that emerge from the ribs; these artefacts are adequately suppressed in OSC–FBP_N images and are only slightly visible for OSC–$FBP_{0.7}$.
OSC–$FBP_{0.3}$ reconstructions show practically the same values for resolution, noise and contrast as the reconstructions produced after initializing with a uniform distribution. This is not surprising, since the blurred initial FBP images used here (Fig. 4.2) are almost noise–free and have the structures devised for assessing the resolution and contrast poorly resolved.

4.4 Conclusions and discussion

In the paper we have shown that streak artefacts, appearing around high–contrast structures in OSC reconstructions, can be adequately suppressed when OSC is initialized with an FBP image. These artefacts are almost completely removed after only one iteration of FBP–initialized OSC, while 10-20 iterations are necessary to clear away the streaks when OSC is started from an uniform image. To achieve such an impressive acceleration, the FBP reconstructions used as the initial condition for the statistical algorithm should not be significantly blurred. As a consequence, additional noise may be introduced into the early iterations of SR. This paper shows, however, that after only a couple of cycles of FBP–initialized OSC the resolution–noise and contrast–noise tradeoff of the reconstructions obtained do not differ any longer from the corresponding quantities for OSC started with a uniform image. The noise initially injected by the FBP image is rapidly removed by SR, after which the final quality of the reconstructions is not compromised.
The initialization of SR with FBP images containing scatter or beam hardening artefacts may seriously affect the convergence properties of the statistical algorithm and the quality of final reconstructions. In such situations it may be necessary to apply one of the existing ad hoc meth-

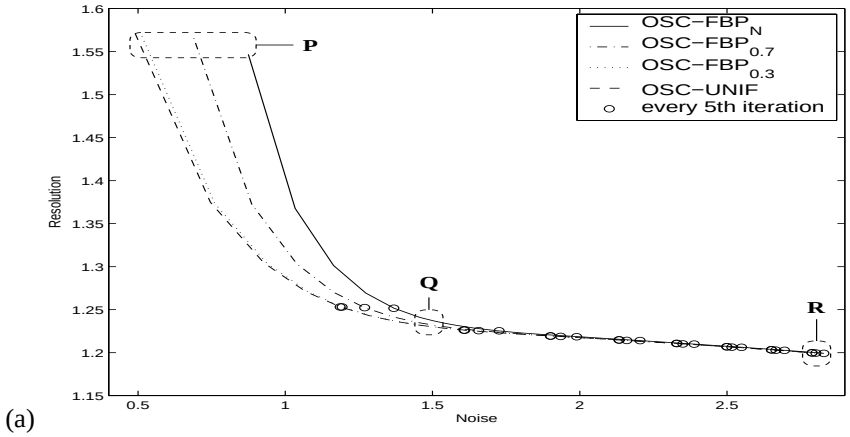

(a)

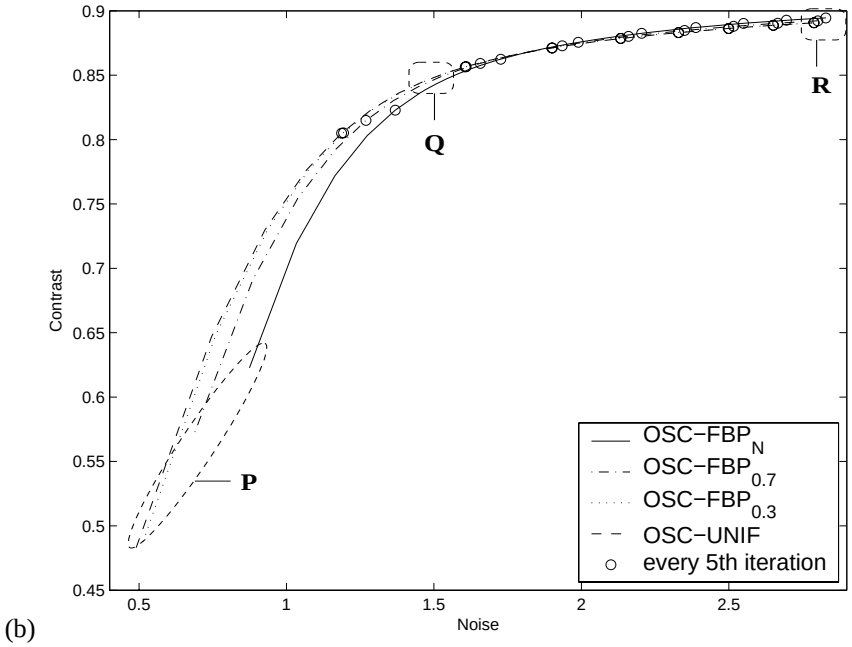

(b)

Figure 4.6: Resolution (Frame (a)) and contrast (Frame (b)) as a function of noise in the background region for differently initialized OSC. For $OSC\text{–}FBP_N$ and $OSC\text{–}FBP_{0.7}$ the start images introduce some additional noise into the reconstructions. It influences only the early iterations of the algorithm and is removed after a few cycles of the reconstruction. The contrast-to-noise ratio of the final reconstruction is not markedly compromised by using FBP as a start image for the OSC. Areas P, Q and R correspond to iterations presented in Fig. 4.4, Fig. 4.7 and Fig. 4.5, respectively.

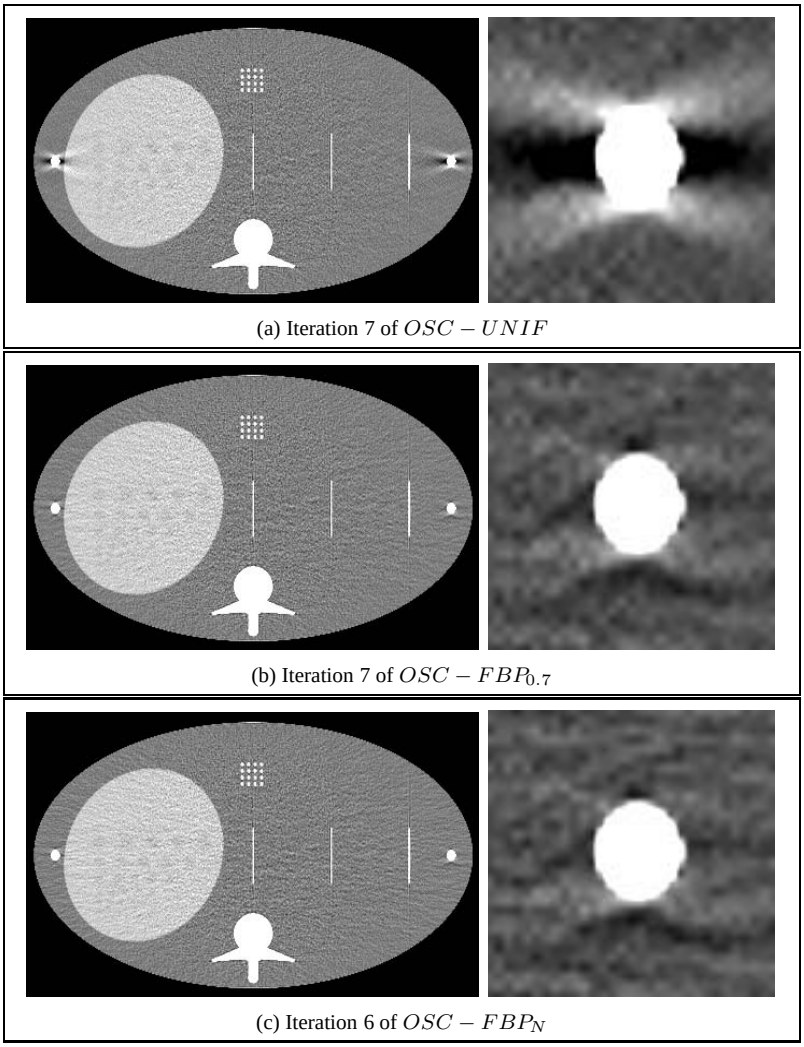

(a) Iteration 7 of $OSC - UNIF$

(b) Iteration 7 of $OSC - FBP_{0.7}$

(c) Iteration 6 of $OSC - FBP_N$

Figure 4.7: Reconstructed images corresponding to the point where the resolution–noise curves for differently initialized OSC begin to coincide (region marked as Q on Fig. 4.6). OSC–$UNIF$ (Frame (a)) still contains streak artefacts that are not visible in the images generated with FBP–initialized OSC (Frames (b) and (c)). The gray–scale is 0.9–1.1 for the whole object view and 0.95-1.1 for the images of the rib region.

ods for beam hardening and scatter correction to FBP reconstruction before the latter is used for SR initialization. These issues were beyond the scope of the present work, but will be addressed in the future in connection with more advanced statistical algorithms, incorporating accurate models of the abovementioned image degrading effects.
In conclusion, we have shown that the advantages of the two reconstruction methods, namely the computational efficiency of FBP and the accurate handling of noise in SR, can be combined in an effective framework for obtaining accurate X–ray CT reconstructions for at least a subset of the cases.

Acknowledgments

We thank to Dr. Auke-Pieter Colijn for valuable comments and discussions.

Chapter 5

Experimental validation of a rapid Monte Carlo based Micro-CT simulator

Abstract

We describe a newly developed, accelerated Monte Carlo simulator of a small animal micro-CT scanner. Transmission measurements using aluminium slabs are employed to estimate the spectrum of the X-ray source. The simulator incorporating this spectrum is validated with micro-CT scans of physical water phantoms of various diameters, some containing stainless steel and Teflon rods. Good agreement is found between simulated and real data: normalized error of simulated projections, as compared to the real ones, is typically smaller than 0.05. Also the reconstructions obtained from simulated and real data are found to be similar. Thereafter, effects of scatter are studied using a voxelized software phantom representing a rat body. It is shown that the scatter fraction can reach tens of percents in specific areas of the body and therefore scatter can significantly affect quantitative accuracy in small animal CT imaging.

5.1 Introduction

Pollution of cone-beam CT projection data with scattered photons can lead to significant degradation of image quality. Scatter contributes to cupping artefacts and causes streaks to appear between dense objects in the reconstructed images (Johns & Yaffe 1982, Joseph & Spital 1982, Glover 1982). Moreover, additional noise is induced into the reconstructions due to the noisy scatter background. This limits the low-contrast detectability in the images obtained (Endo et al. 2001).

The amount of scattered X-rays detected depends strongly on the type of CT scanner and the object under study. It is much higher for clinical cone-beam CT scanners than for fan-beam CT,

due to the use of 2D detectors that observe out-of-slice scattered photons: an SPR in excess of 100% can be found for pelvis scans with flat panel detectors (Siewerdsen & Jaffray 2001). For clinical cone-beam CT scanners the amount of scatter can be reduced by using scatter grids and by post-object focused collimation (Endo et al. 2001). In micro-CT, however, the use of scatter grids and post-object collimation is prohibited due to the small size of the detector elements (of the order of 10 micron) compared to the septa thickness required. As a result, scatter may affect the image quality for micro-CT significantly, despite the small size of the objects scanned. Knowledge of scatter distributions is therefore essential to optimize the design of cone-beam (micro-)CT systems (Siewerdsen & Jaffray 2000). Such knowledge can also be used to develop corrective image reconstruction algorithms (Johns & Yaffe 1982, Joseph & Spital 1982, Glover 1982).

A common technique for estimating scatter projection data is to perform computer simulations. Some authors have simulated the scatter contribution using analytical models (Johns & Yaffe 1982, Boone & Seibert 1998, Honda et al. 1991). These models may become very complicated if they are to be used to accurately simulate non-homogeneous objects. Alternatively, Monte Carlo (MC) methods can be applied to model the interactions of X-rays with matter in a general and accurate way, even if the objects of study are complicated and non-homogeneous. Monte Carlo based simulations of scatter in X-ray CT have already been reported by several authors (e.g. Joseph & Spital (1982), Chan & Doi (1983), Kanamori et al. (1985), Boone & Seibert (1988), Kalender (1981), Spies et al. (2001), Spyrou et al. (1998)). Acceleration schemes such as point detector approach (aka. Forced Detection, Williamson (1987), Kalos (1963), Leliveld et al. (1996)) have been proposed in order to reduce the amount of simulated photons required to arrive at a noise-free projection estimate (ie. a MC estimate with very low variance). A method aimed specifically at the rapid estimation of noise-free scatter projections in cone-beam CT scanners has been developed recently (Colijn & Beekman 2004).

The goal of this paper is to describe and experimentally validate a newly developed, fast MC simulator which combines the method described in (Colijn & Beekman 2004) with other acceleration techniques. We outline the details of the model of photon transport employed in the simulator. Guidelines regarding the choice of some of the simulation parameters, such as the maximum scatter order to be included, are also presented. Furthermore, a method of estimating the X-ray tube's spectrum (modified from Ruth & Joseph (1997)) is described. Simulation accuracy is verified by comparing simulated micro CT-scans of various physical phantoms with measured data. Finally, the influence of scattered radiation on the quality of reconstructions is assessed by analysing the phantom data and by simulating CT scans of a digital rat abdomen phantom.

5.2 Methods

In this section the micro CT scanner and the physical processes that form the core of our simulation program are described and the measurement procedure for estimating the spectrum of the X-ray tube is outlined. Also the methods used to validate the simulator are presented.

5.2.1 Small animal CT scanner

The Monte Carlo based simulator developed here is parameterized for a small animal micro-CT scanner with cone-beam imaging geometry. A schematic picture of this scanner (SkyScan 1076, Sasov & Dewaele (2002)) is shown in Fig. 5.1 (left panel). The source-detector distance of the scanner is 172 mm and the distance from the rotation axis to the detector plane is 51 mm.

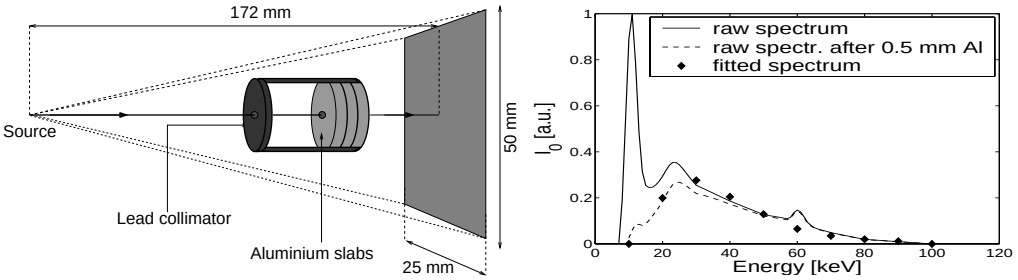

Figure 5.1: Left: schematic drawing of the SkyScan 1076 small-animal scanner and the experimental setup used for spectrum determination. Right: Spectral distribution of a Hamamatsu L8032 X-ray source operated at 100 kV. The solid line represents the raw spectrum operated, as obtained from the L8032 data-sheet. The dashed line shows the spectrum after the beam has passed 500 μm of aluminium attenuator. The diamonds show the measured spectrum found following the fitting procedure outlined in the text.

- **Source.** The photon source is a Hamamatsu micro-focus X-ray tube (type L8032) with a Tungsten anode operated at a high voltage of 100 kV. The source is 5 μm in diameter. A 100 μm Be window separates the vacuum chamber and the surrounding air. A 500 μm aluminium attenuator is used to reduce the primary flux of low energy photons.

  The emission cone of the the X-ray source is 39°. Behind the source and the attenuator the X-rays are collimated so that the primary rays are directed only towards the active part of the detector. The opening angle of the beam in the trans-axial plane, or fan-angle, is 32°, and the opening angle along the axis of the scanner, or cone-angle, is 8°.

- **Detection.** The SkyScan 1076 employs a P43 scintillator (Gd_2O_2S) with a density of 7.3 g/cm^3 and a thickness of 0.025 mm as X-ray converter. The converted photons are projected onto a CCD. There are 4000 pixels in the trans-axial and 2000 pixels along the axis of the scanner. The pixel-size is 12.5×12.5 μm^2. For wide field-of-view scans the CCD is translated in the trans-axial plane and each projection is obtained by stitching together two half-projections. In this way a detection area of 100 mm is obtained in the trans-axial plane.

5.2.2 Energy spectrum calibration

In the case of the Hamamatsu L8032 tube, an estimate of the raw spectrum was provided by the manufacturer (private communication) and the simulations could have been performed using this data. However, there are many factors (such as possible variations in the thickness of the

pre-object Al attenuator) that may cause the energy distribution of a particular scanner to differ from the data provided by the tube manufacturer. Sometimes, such data are not available. Below, a spectrum estimation technique that allows the simulation to be calibrated to any given scanner is outlined. The approach proposed is a variation of the method described in Ruth & Joseph (1997).

The experimental setup (see Fig. 5.1, left) consists of a 10 mm thick Pb collimator with an opening of 2 mm. The collimator is placed in the X-ray beam of the scanner behind the aluminium attenuator and directs the radiation towards the central detector pixels. After collimation, the beam is blocked with aluminium slabs of varying thickness d_{Al} ($d_{Al} = 1, 2, 3..10, 15 \pm 0.01$ mm). The detected radiation energy fluence $I_{measured}(d_{Al})$ is measured for each of the slabs. It is assumed that the spectrum can be described as a finite number of energy bins. The photon fluence in each bin is unknown and will be denoted as $\lambda(E_i)$. Using this model of the spectrum, one can predict the energy fluencies measured in the slab experiment on the basis of known values of attenuation coefficient of aluminium:

$$I(d_{Al}) = \sum_{i=1}^{N} \lambda(E_i)\epsilon(E_i)E_i e^{-\mu_{Al}(E_i)d_{Al}} \tag{5.1}$$

where $I(d_{Al})$ is the prediction of the measured energy fluence, $\mu_{Al}(E_i)$ is the attenuation coefficient of Al at energy E_i and $\epsilon(E_i)$ is the detector efficiency at this energy. N is the number of energy bins, in our case $N = 10$. In order to determine the unknown photon fluencies $\lambda(E_i)$, a χ^2 minimization is performed:

$$\chi^2 = \sum_{d_{Al}} \left(\frac{I(d_{Al}) - I_{measured}(d_{Al})}{\sigma(d_{Al})} \right)^2 + \alpha \sum_{i=1}^{N-1} (\lambda(E_i) - \lambda(E_{i+1}))^2 \tag{5.2}$$

where $\sigma(d_{Al})$ is the uncertainty of the energy fluence measurement with slab thickness d_{Al}. The quadratic penalty term is added to suppress strong, non-physical oscillations of the spectrum that arise due to ill-posed nature of the spectrum estimation problem.

In the original method described in Ruth & Joseph (1997), the detector efficency $\epsilon(E_i)$ is included in the energy bin value $\lambda(E_i)$. The resulting distribution therefore combines the spectral properties of the source and the detector. Since $\epsilon(E_i)$ depends on the incidence angle of the photons on the detector, such a combined estimate of the spectrum should in principle be based on measurements performed at different detector elements, not only at the central ray. Moreover, in a Monte Carlo simulation it is necessary to know the spectrum of the X-ray beam as it enters the object of interest. We therefore propose to separate the source and detector contributions to the spectrum by using the following model for detector efficiency:

$$\epsilon(E_i) = 1 - e^{-\mu_{scint}(E_i)d_{scint}} \tag{5.3}$$

where μ_{scint} and d_{scint} are the attenuation coefficient of the scintillator and the path length of the X-ray beam through the detector element, respectively. For measurements on the central detector pixels d_{scint} is equal to the detector thickness.

The raw spectrum of the tube, as obtained from Hamamatsu data-sheet, is drawn with a solid line in Fig. 5.1 (right panel). The dashed line shows the same spectrum after the beam

has passed a 500 μm Al attenuator (obtained by computer simulation). The diamonds mark the spectrum estimated with the fitting method described above. The regularization parameter α of the fit (Eq. 5.2) was found by repeated numerical simulations of the experiment. During these experiments, the computed attenuated spectrum of the Hamamatsu source was employed.

The global shape of the estimated spectrum agrees quite well with the simulated attenuated spectrum obtained from tube's manufacturer data. The fitting procedure, however, was unable to reproduce the fine details of the energy distribution, such as the peak at 60 keV. Instead, the peak was spread out over the spectrum. This is not surprising, taking into account the ill-posed nature of the estimation problem (Ruth & Joseph 1997). We found that the fit could not be improved by adding more measurement points (using more different Al slab thicknesses) since the measurements themselves are not sensitive to subtle variations in the energy distribution of the X-ray beam. For the same reason, dividing the spectrum into more energy bins would not lead to improvement in the quality of the fit.

The X-ray energy distribution estimated by the fitting method was further employed in the Monte Carlo simulations analysed in this paper. Good agreement was obtained between the simulated and measured projection data (see Sec. 5.3) of various objects. This shows that, despite the lack of fine details, the estimated spectrum retains the most important properties of the X-ray tube's energy distribution.

5.2.3 CT simulator

The simulator consists of two parts: the projections of primary X-ray radiation are computed with a ray–tracer and the scatter distribution is estimated with an accelerated Monte Carlo simulation. In this subsection both simulation tools are described in detail.

Simulation of primary X-ray radiation

- **Emission.** For each of the ten energy bins of the fitted spectrum (see Fig. 5.1, right), sixteen rays per detector pixel are emitted from the centre of the focal spot.

- **Photon transport.** The photon transport is simulated in a voxelized model of the object of interest. The grid contains $128 \times 128 \times 128$ voxels having a size of $0.55 \times 0.55 \times 0.55$ mm^3. Each voxel value represents the total attenuation of the corresponding material ('water', 'Teflon' or 'perspex' for the cylindrical phantoms and 'soft-tissue' or 'bone' for the rat abdomen phantom, cf. Sec. 5.2.4), obtained from XCOM databases (Berger et al. 1999). Siddon's ray–tracing algorithm (Siddon 1986) is used to calculate the total attenuation along each of the primary rays.

- **Detection.** The simulated detector consists of a 400×100 grid of 250×250 μm^2 pixels. The detection process is modelled using Eq. 5.3, taking into account the attenuation properties of the P43 scintillator and the energy and impact angle of each individual X-ray.

Accelerated Monte Carlo scatter simulation

- **Emission.** The X-rays are emitted from the centre of the focal spot. Their direction is chosen randomly from an isotropic distribution of angles in the cone and fan angle range.

To account for the spectral shape of the X-ray tube, photon energy is sampled randomly from the fitted spectrum (see Fig. 5.1, right).

- **Photon transport and detection using the point detector approach.** The simulation is performed in the same voxelized model of the object as the ray-tracing of primary X-rays. For each photon, the total attenuation path length to the interaction point (including the attenuation due to photoelectric absorption and to coherent and incoherent scattering) is first sampled randomly. The photon is traced to this point and then interaction type (either Compton or Rayleigh scattering) is randomly selected using attenuation coefficients from the XCOM libraries (Berger et al. 1999). Since only scattering interactions are of interest during the simulation, at each interaction point a weight is given to the photon that is equal to the probability of the photon not being absorbed photoelectrically.

  The simulator uses a slight variation of the point detector approach (aka. Forced Detection, Williamson (1987), Kalos (1963), Leliveld et al. (1996)) which speeds up the convergence to noise-free scatter projections. In the point detector approach, photons from each interaction point are forced to generate a signal in each of the detector elements. This involves assigning to each photon an appropriate weight that takes into account the probability of scatter in the forced direction, geometric factors, and the material between the scatter point and the detector. In the case of cone-beam CT, forcing detection in each of the detector elements would increase the computing time prohibitively, since the number of detector pixels, and thus the number of line integrations is extremely high. An effective way to reduce the number of line-integrations is to force the photons towards a limited subset of the N_{det} pixels only. $N_{det}^{FD} = 5$ pixels or $N_{det}^{FD} = 100$ pixels are chosen randomly if an interaction is due to Compton or Rayleigh scatter, respectively. An extra weighting factor of N_{det}/N_{det}^{FD} is assigned to the photon to correct for the fact that not all pixels are sampled. The photon detection process is simulated as in the case of primary X-ray radiation (see Eq. 5.3). The detector configuration is the same as that used for the ray-tracing of primary X-rays.

  After the signals have been generated in the detectors, the original photon is deflected along a randomly selected angle, its free path is again sampled and ray-tracing is performed till the next interaction. This process is repeated until the photon leaves the object or until the maximum number of interactions has been exceeded. In the latter case the photon is removed from the beam and no signal is generated. Up to fourth order scatter was simulated. The right frame of Fig. 5.2 presents a comparison of scatter distributions obtained with 1, 2, 3, 4 and 5 orders of scatter included in the simulation. Each profile represents the central detector row of a single scatter projection of a rat abdomen phantom (cf. Sec. 5.2.4). 10^9 photons were simulated with Forced Detection and de-noising of the resulting projection with a Richardson-Lucy fit (standard deviation of the Gaussian kernel of the fit $\sigma_{xy} = 5$, see the next Section). Only tiny differences can be observed between profiles obtained with the inclusion of more than 3 scatter orders. This is confirmed by Fig. 5.2 (right), where the contribution of photons that interacted for maximally 1,2,3,4 and 5 times to the total amount of scattered photons is compared. It follows, that simulation of 4 interactions per photon is sufficient to estimate scatter accurately in objects with a size comparable to that of the rat body (diameter of up to 6 cm).

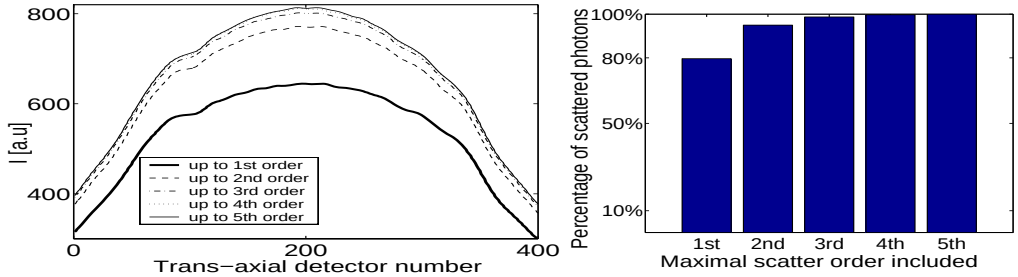

Figure 5.2: Left: Comparison of profiles through MC simulated scatter projections of the rat abdomen phantom. Compared are profiles obtained with the inclusion of up to 1st order scatter (thick solid line), up to 2nd order scatter (dashed line), up to 3rd order scatter (dash-dotted line), up to 4th order scatter (dotted line) and up to 5th order scatter (solid line). Right: contributions of different scatter orders to the total amount of scattered photons detected within a single projection; maximum number of interactions permitted was five. Each bar represents the fraction of scattering events up to a certain order in the total amount of scattered photons detected.

During the MC simulation, special care was taken to model the angular distribution of scattered X-rays properly. For Compton scattering, incoherent structure functions are used that take into account the electron binding energy and atomic shell profiles. For Rayleigh scatter, measured structure functions from Peplow *et al.* (Peplow & Verghese 1998) are used if available and otherwise the form factors from Hubbell *et al.* (Hubbell & Overbo 1979).

The contribution of Rayleigh scattering to the detected X-rays is not negligible, despite a relatively low cross-section. This is because the change in direction of a photon deflected through Rayleigh scatter is usually only a few degrees, resulting in a relatively high probability to still hit the detector plane after the interaction.

- **De-noising of scatter distributions using Richardson-Lucy fit.** The simulator described above uses Forced Detection to reduce the variance in the scatter distributions obtained. Nevertheless, a large amount of photons has still to be simulated if we are to obtain a noise-free Monte Carlo estimate. We therefore suggested the use of a Richardson-Lucy fitting algorithm in order to obtain low-noise scatter estimates from the noisy FD projections computed with a low number of simulated photons. This procedure is described in detail in Colijn & Beekman (2004). It uses maximum likelihood algorithm to fit Gaussian basis functions to the simulated data. Smooth estimates of scatter projections can therefore be obtained even from simulations with low number of photons. This allows for a reduction of the time needed for Monte Carlo simulation by as much as two orders of magnitude in comparison with MC with Forced Detection only.

  In the present study, MC simulations were performed using 10^5 photons per projection. The projections obtained were de-noised using 20 iterations of the Richardson-Lucy fit. The standard deviation of the Gaussian kernel of the fit was set to $\sigma_{xy} = 15$ detector pixels.

5.2.4 Evaluation and validation

- **Phantoms and simulations.** Three cylindrical phantoms were constructed: (i) a homogenous water phantom (diameter: 60 mm), (ii) a water phantom (diameter: 60 mm) with four Teflon rods with diameters (along the axial direction) of 10 mm and 3 mm and (iii) a water phantom (diameter: 60 mm) with two 10 mm Teflon rods and two 3 mm stainless steel rods. The casing of all phantoms was 1 mm polystyrene. Voxelized digital representations of the phantoms were created for use in the simulations.

  A digital phantom representative of a rat abdomen was used to simulate the effects of scatter in a more realistic environment. The phantom was derived from a digital mouse phantom (Segars et al. 2003) by scaling it to the size of a rat. The scaling constants were found by the investigation of micro-CT scans of rat abdomen and chest. In Fig. 5.3 an axial view of the whole phantom is displayed. Dashed lines delineate the abdomen zone

Figure 5.3: Left: central axial slice of rat phantom with the abdomen section that was used in the simulations delimited with dashed lines. Right: central trans-axial slice of the abdomen section. Gray-scale is 0.9-1.1.

  that is later used for simulations. In addition, a central trans-axial slice of the abdomen region is depicted. The long axis of the rat's body (the width of the animal) measures 58.2 mm, the short (apical) axis (the height) being 54.5 mm.

- **Measurements.** CT scans of the cylindrical phantoms were recorded. The axes of symmetry of the phantoms were positioned along the rotational axis of the scanner. The X-ray high voltage was set to 100 kVp and projections were recorded in steps of $0.6\,^{\circ}$.

- **Image Reconstruction.** A statistical reconstruction (SR) method, namely the Convex algorithm (Lange 1990), was used to reconstruct the images from both simulated and real projection data. Three reconstructions were generated for each phantom: from simulated projections with the scatter added, from simulated projections without the scatter (only primary radiation) and from the measured data. In the latter, these reconstructions and the corresponding projection data sets are denoted as MC-scatter, MC-no scatter and Measured Data, respectively.

  During the reconstruction, a ray–driven projector and back-projector were used. No beam hardening or scatter correction was included. The reconstruction grid was 128x128 voxels (covering only the central slice of the object) and a subsampling of two rays per detector pixel during the ray–tracing was applied. The display matrix was 64x64 voxels (resolution lower than that of the reconstruction grid was used to suppress edge artefacts (Zbijewski & Beekman 2004*a*)). A hundred iterations of the Convex algorithm were used to produce the images presented in the paper.

In order to calculate the ray attenuation values during the reconstruction of the real data, a blank scan was acquired with a large number of counts. It provided an almost noise-free estimate of the unattenuated X-ray energy fluence distribution in the detector plane. By using a blank scan during the reconstruction and during the comparison of simulated and real projections, it was possible to divide out some of the geometric effects and scanner non-uniformities, such as the spatial irregularity of the source radiation (due, for example, to the "heel-effect" of the X-ray tube).

- **Quantitative evaluation of Monte Carlo simulation.** Normalized Error in the simulated projections was computed, according to:

$$NE(u,v) = \frac{p_{MeasuredData}(u,v) - p_{MC-simulated}(u,v)}{p_{MeasuredData}(u,v)} \tag{5.4}$$

where u and v are detector coordinates and $p_{MeasuredData}(u,v)$ and $p_{MC-simulated}(u,v)$ are the real and the MC simulated projections, respectively. NE was calculated for both the Monte Carlo simulation with the scatter included and the scatter-free MC simulation. The NEs as displayed in the paper were smoothed by averaging up groups of eight neighbouring pixels.

- **Scatter Characterization.** The amount of scatter is characterized in terms of the scatter-to-primary ratio (SPR), which is defined as the ratio of detected scattered radiation and primary radiation in each pixel.

5.3 Results

In this section, results of the validation of the fast Monte Carlo simulator are presented. Thereafter, phantom data and simulation experiments are used to characterize scatter effects in cone beam micro-CT imaging.

5.3.1 Water and rod phantoms

Fig. 5.4, 5.5 and 5.6 depict profiles taken through simulated and measured projections of the water cylinders and rod phantoms. Both real and simulated projections were divided by their respective blank scans to compensate for some of the scanner non-uniformities (blank-scan correction). The profiles obtained from the measurements and from the MC simulations with scatter modelling are shown to be in good agreement. In the central panels of all the figures, Normalized Error (Eq. 5.4) is displayed for the projection under consideration. The error is usually no larger than ± 0.05. It peaks for the detectors onto which the borders of the object or of the high-contrast structures within the object were projected. This is probably due to slight geometric misalignment between the simulation and reality. For example, the oscillatory shape of NE of the steel rods (Fig. 5.6) suggests that in the phantom they are slightly shifted with respect to their true position. High attenuation of the rods causes their projections to have a high noise level, which also leads to increased uncertainty of the corresponding Normalized Error values. The bell-shaped NE pattern for the case of the 60 mm water phantom (Fig. 5.4) might have

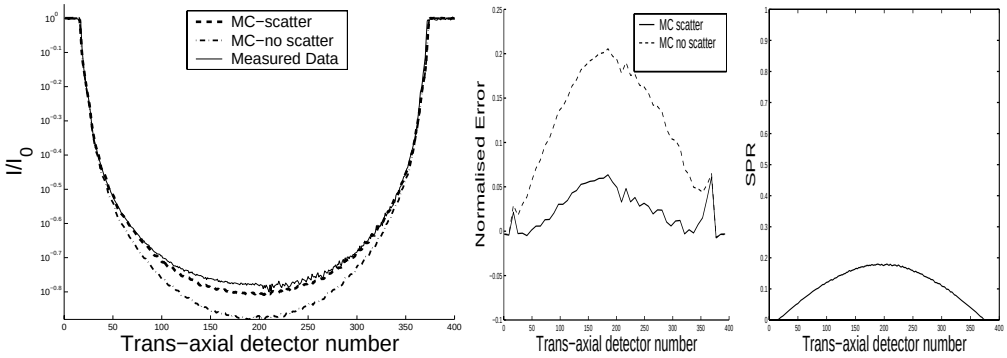

Figure 5.4: Left: Profiles taken through measured and simulated projection data of the 60 mm water phantom (logarithmic scale). Centre: the Normalized Error (defined by Eq.5.4) for the same projection profile. Right: the scatter-to-primary ratio for this projection.

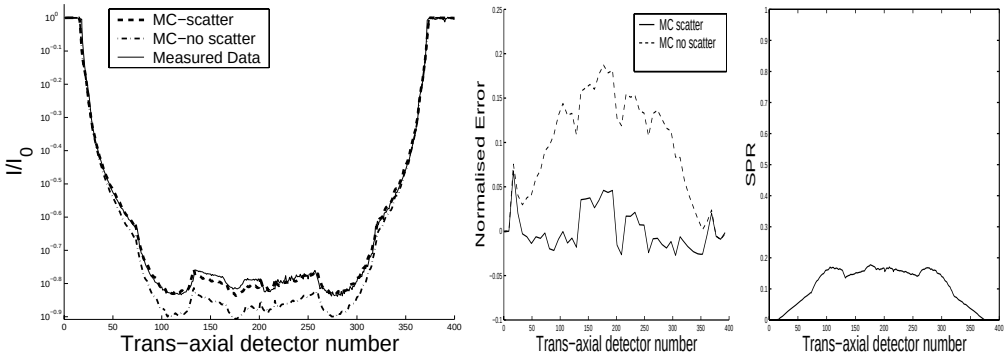

Figure 5.5: Like Fig. 5.4 but for the phantom containing Teflon rods.

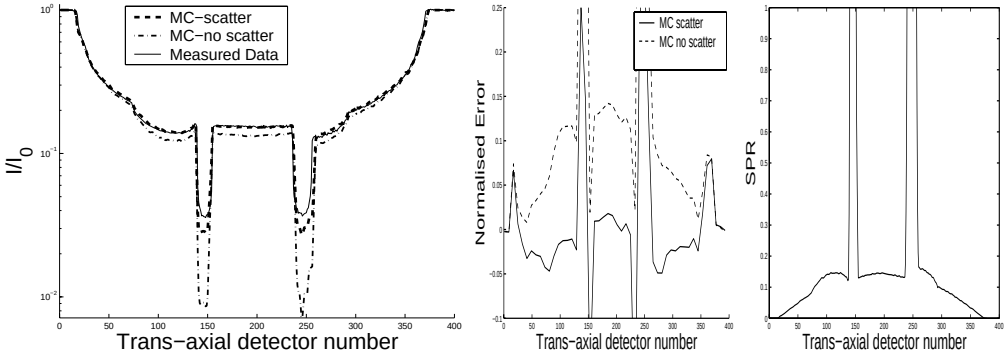

Figure 5.6: Like Fig. 5.4 but for the phantom containing Teflon and stainless steel rods.

been caused by discrepancies in the dimensions and shape of the phantom in simulation and in reality. The stitching of the half-projections performed in SkyScan micro-CT machine in order to broaden the field of view is probably also responsible for part of the simulation error.

Exclusion of the scatter component from projections (dashed lines in the Normalized Error plots) adds a significant, positive-definite, bell-shaped component to the Normalized Error profiles. Superimposed upon this component are error patterns similar to the ones obtained with MC simulations employing scatter modelling. This reinforces the conclusion that the discrepancies between MC simulated projections with scatter included and real data are due mainly to geometric misalignments and projection stitching. The size of the error caused by not including the scatter in the simulations shows that for the modelled micro-CT system the scatter contribution to the projection data is not negligible.

The SPR is plotted in all the figures in the right panel. It should be noted that even for a low average value of SPR, the SPR locally can be much higher, due to the presence of highly attenuating objects in the phantom. For small cylindrical water phantom (diameter: 36 mm) the maximum SPR was estimated to be of the order of 5-10%. In the water phantom of 60 mm diameter the SPR reached a maximum value of about 20%, whereas the steel rod phantom gave rise to maximum SPR values of even more than 100%.

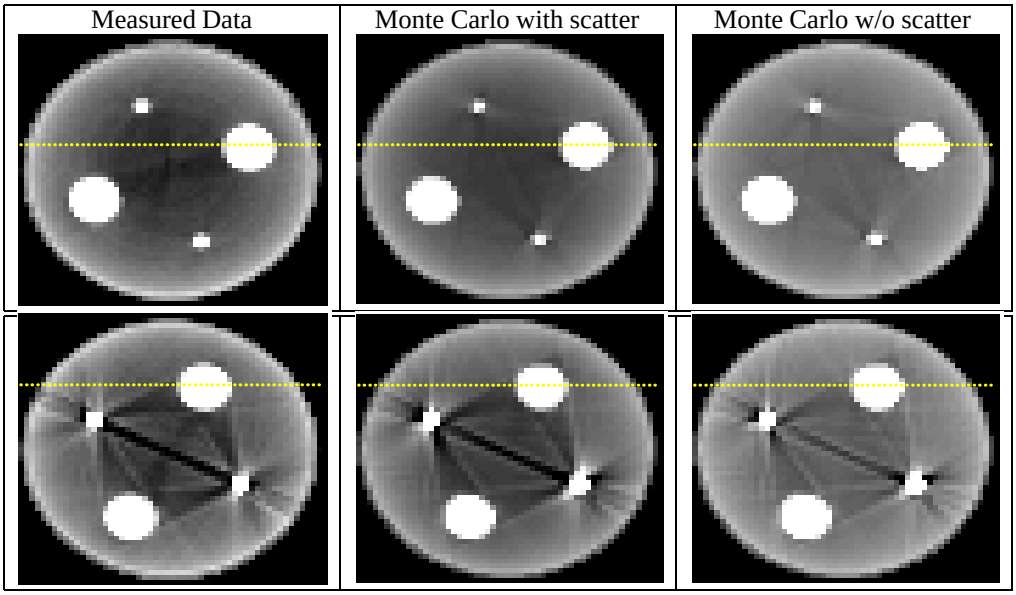

Figure 5.7: Reconstructed slices: 60 mm water phantom with Teflon inserts (upper row) and 60 mm water phantom with Teflon and stainless steel inserts (bottom row). Left: reconstruction of real data. Centre: reconstruction of Monte Carlo simulated data with scatter included in the simulation. Right: reconstruction of Monte Carlo simulated data with scatter component excluded from the simulation. Dashed line represents the position of profiles shown in Fig. 5.8. Grey-scale is 0.8-1.6.

Fig. 5.7 shows reconstructed images of the rod phantoms. In the column on the left, the reconstructions (central slices) of measured data are displayed. The central column contains

images obtained from simulated projections for the case where scatter was included in the simulation. For all phantoms, both images are visually very similar and show a decrease in density towards the centre of the phantom (cupping), as expected. In the column on the right the reconstructions of the simulated data are shown once more, but now for scatter-free simulations. Artefacts that can be perceived in these images are only due to beam hardening and to edge-gradient effects. It can be concluded that scattered radiation leads to a visible increase in cupping and to a broadening of the streaks.

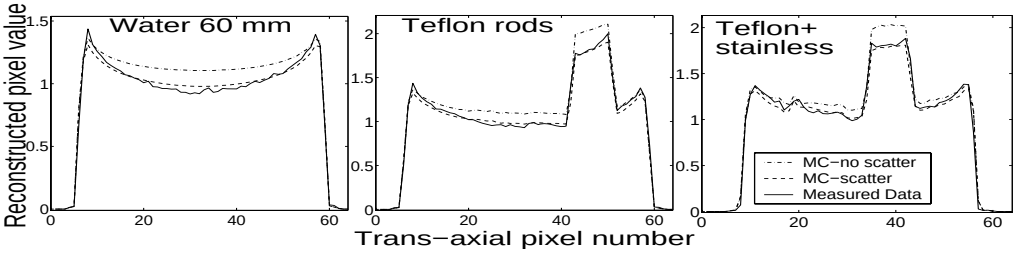

Figure 5.8: Profiles of reconstructed pixel values. Solid line: reconstruction of real data. Dashed line: reconstruction of Monte Carlo (MC) simulated data with scatter included in the simulation. Dash-dotted line: reconstruction of Monte Carlo simulated data with the scatter component excluded.

Horizontal profiles taken through the reconstructed images of the phantoms are shown in Fig. 5.8. The solid line represents the measured profile and the dashed line the simulated profile. The agreement between the simulation and measurement is good, indicating an accurate simulation. The dash-dotted line shows a profile taken at the same position but from a reconstruction of projections simulated without taking into account scattered radiation. The scatter is found to almost double the magnitude of the cupping artefact.

5.3.2 Rat abdomen phantom

Fig. 5.9 displays SPR for two projections taken through the rat abdomen phantom. SPRs achieve 20% for the central (thickest) parts of the body. For projections of bony regions, SPR grows to 25% and locally even to 35% (e.g. in the upper detector rows of Fig. 5.9, right panel). The values of SPR attained are comparable to the values obtained for the water phantom of similar diameter (60 mm).

5.4 Discussion

The simulation described in this paper was found to provide an accurate description of the measured projection data of a micro-CT scanner. The results of the validation allow us to use the MC simulator as a tool to investigate scatter effects in micro-CT scanners.

The use of Monte Carlo simulator allowed us to separate the scatter and primary radiation contributions to the projection data. The influence of scatter on the reconstructed images could therefore be studied separately from other artefact sources like beam hardening. Results indicate that scatter may be responsible for half of the magnitude of the cupping artefacts. It also induces

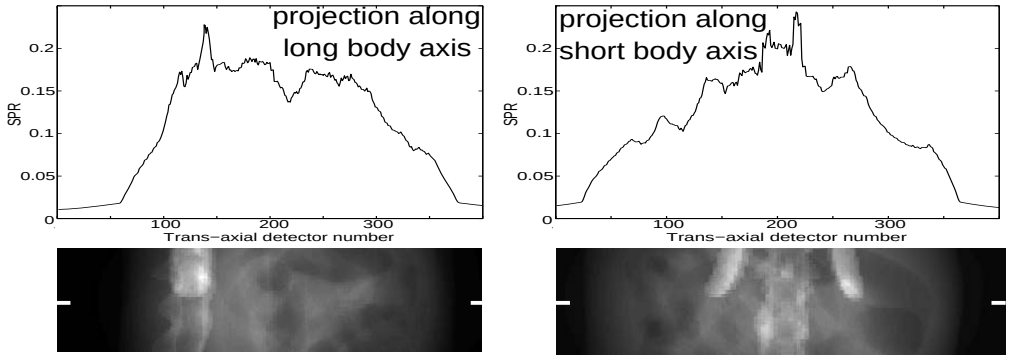

Figure 5.9: Scatter-to-primary ratios for two projections of the rat abdomen phantom. Top row: profile taken through the SPR at the central detector row. Bottom row: SPR for the whole projection image (grey-scale 0–0.35, segments mark the positions of the profiles).

a noticeable broadening of the streaking artefacts caused primarily by beam-hardening (and to some extent also by nonlinear partial volume effects).

For the rat abdomen phantom, the estimated scatter-primary-ratio was comparable to the SPR of the water cylinder of similar size (diameter: 60 mm), except for the projections of bony regions which reached an SPR of 35%. One can therefore expect that in the scans of rat abdomen and chest the degree of reconstruction artefacts caused by scatter will resemble the case of water phantoms, i.e. that scatter may cause serious cupping in the images obtained, hampering not only the contrast and lesion detectability, but also the quantitative accuracy of the reconstructions.

To obtain the smooth scatter projections that are needed for the image reconstructions the Richardson-Lucy based fitting algorithm (Colijn & Beekman 2004) was used. For this reason only it was possible to simulate the whole sinograms within reasonable amounts of time. By using this acceleration scheme, only 10^5 photons were needed for each simulated scatter projection, instead of 10^7 to 10^8 that would have been needed otherwise. It took about 8 hours to simulate 353 projections on a dual processor Xeon 2.6 GHz machine, the additional fitting time required being only one minute.

Effects such as non-uniformity of the source emission remained unaccounted for in the current version of the simulator. Also detector simulation is simplified and does not include, for example, the generation of characteristic radiation from the K-edge of the scintillating material. Since a major part of these inaccuracies cancels out during blank scan correction of projection data, good agreement could still be achieved between the simulation and the reality. Currently we are working on extending our simulator by incorporating more accurate models of source and detector physics. Such an improved simulator will allow us to study the influence of these factors on the quality of the images obtained. Incorporated into model-based corrective reconstruction framework, it will enable to reduce source and detector-related artefacts. This will be important for further development of tomographical X-ray micro-imaging, since effects such as source extension or source emission irregularity may significantly reduce the resolution of micro-CT images.

5.5 Conclusions

A Monte Carlo simulator for micro-CT has been developed and experimentally validated using CT scans of several water cylinder phantoms, both homogenous and containing Teflon and stainless steel rod inserts. The spectrum of the X-ray tube was estimated following a slight modification of the scheme proposed in Ruth & Joseph (1997). The simulated projections were shown to be in good agreement with the measured data. The reconstructed images were also similar to the images obtained from the real projections. The simulation results were further used to characterize the effects of scatter in small animal CT imaging. The results presented indicate that for objects such as rat abdomen, up to 50% of the cupping artefacts observed in micro-CT reconstructions might be due to scatter.

Acknowledgments

We thank Dr. Sebastiaan Kole for critical comments and discussions.

Chapter 6

Efficient Monte Carlo based scatter artefact reduction in cone-beam micro-CT

Abstract

Cupping and streak artefacts caused by the detection of scattered photons may severely degrade the quantitative accuracy of cone-beam X-ray CT images. In order to overcome this problem, we propose and validate the following iterative scatter artefact reduction scheme: Firstly, an initial image is reconstructed from the scatter-contaminated projections. Next, the scatter component of the projections is estimated from the initial reconstruction by a Monte Carlo (MC) simulation. The estimate obtained is then utilized during the reconstruction of a scatter-corrected image. The last two steps are repeated until an adequate correction is obtained. The estimation of the noise-free scatter projections in this scheme is accelerated in the following way: first, a rapid (i.e. based on a low number of simulated photon tracks) Monte Carlo simulation is executed. The noisy result of this simulation is de-noised by a three-dimensional fitting of Gaussian basis functions. We demonstrate that, compared to plain MC, this method shortens the required simulation time by three to four orders of magnitude. Using simulated projections of a small animal phantom, we show that one cycle of the scatter correction scheme is sufficient to produce reconstructed images that barely differ from the reconstructions of scatter-free projections. The reconstructions of data acquired with a CCD-based micro-CT scanner demonstrate a nearly complete removal of the scatter-induced cupping artefact. Quantitative errors in a water phantom are reduced from around 12% for reconstructions without the scatter correction to 1% after the proposed scatter correction has been applied. In conclusion, a general, accurate and efficient scatter correction algorithm is developed that requires no mechanical modifications of the scanning equipment and results in only a moderate increase in the total reconstruction time.

6.1 Introduction

In cone beam micro–CT systems, anti-scatter grids and pre–detector collimators cannot be used for scatter reduction due to the small size of detector pixels. For very small objects, such as mice, the amount of detected scatter can still be relatively low, despite the lack of any efficient scatter rejection mechanism (Black & Gregor 2005). For larger specimens, such as rats, the detection of scattered photons becomes a significant problem, leading to scatter-to-primary ratios reaching 10-20% in individual detector pixels (Colijn et al. 2004). Scattered photons significantly degrade the quantitative image accuracy, reduce the low-contrast detectability (Endo et al. 2001) and introduce cupping and streak artefacts (Johns & Yaffe 1982, Joseph & Spital 1982, Glover 1982). As much as half of the magnitude of the cupping artefacts present in micro-CT reconstructions of rat-sized objects is caused by scatter (Colijn et al. 2004). Therefore micro-CT will clearly benefit from some form of scatter correction.

One class of the existing scatter correction methods is based on an assumption of a uniform scatter background, where uniformity is either imposed on all projections or only within one tomographic view (Glover 1982, Bertram et al. 2005). However, even in a simulation study, where optimal choice of the constant scatter value was possible, the results obtained with this class of correction methods were inferior to those achieved with a spatially varying approximation of the true scatter distribution (Bertram et al. 2005).

Another approach would be to use scatter distributions measured in advance for homogeneous objects similar in shape and size to the typical object being scanned. Due to the strong dependence of scatter fields on the density distribution of the scattering medium (Colijn & Beekman 2004, Colijn et al. 2004), such a scheme would be also sub-optimal (Zhu et al. 2005).

Alternatively, scatter fields are sometimes represented as a convolution of weighted measured projections with some blurring kernel (Ohnesorge et al. 1999, Sabo-Napadensky & Amir 2005), a method that has been used previously in digital radiography (Love & Kruger 1987). Scatter estimation is in this case only approximate, as the kernel shapes are either empirically determined for some typical experimental circumstances or are derived from simplified mathematical models. Furthermore, knowledge of scatter-to-primary ratio (SPR) is necessary for those methods, but the dependence of SPR on the object shape and composition is usually neglected and some global, empirically determined constant is typically applied.

All the above-mentioned techniques result only in a very approximate estimates of the true scatter distributions since the details of the shape and composition of the scattering object are usually neglected. If truly quantitative correction is sought, more accurate knowledge of the exact shape of the scatter distribution of the particular object being examined is desirable (Bertram et al. 2005).

The scatter component on the projections can be measured during the scanning. To this end, additional projections are acquired with an array of narrow lead beam-stops placed between the source and the patient. The main contribution to the radiation measured behind the beam-stops comes from object scatter. The distribution of scatter in a particular projection is estimated by an interpolation of the data measured in pixels located in the shadows of the beam stops. Several variations of this method exist, each inspired mainly by the desire to reduce the dose increase caused by the need for additional beam-stop exposures. Some authors propose to measure only a few scatter projections and to retrieve the remaining ones by an angular cubic spline interpolation (Ning & Tang 2004). Alternatively, scatter can be measured together with the projections

used later for the reconstruction by keeping the beam-stop array constantly present during the acquisition. To avoid a build-up of errors in the projection data, the position of the array with respect to the detector changes during the scan (Zhu et al. 2005). Both these measurement-based methods require mechanical modifications of the equipment, complicate and lengthen the scanning procedure and may increase the dose delivered.

Scatter fields can also be estimated by computer simulation based either on simplified models of the object (which, as mentioned above, might not be sufficient) or on the reconstructions obtained from scatter-contaminated data. Analytical simulation schemes have been proposed (Wiegert et al. 2005), but they may become prohibitively slow when inhomogeneous objects are considered. Moreover, the incorporation of higher order scattering (which constitutes a high fraction of the total scattered radiation, Colijn et al. (2004)) into analytical models is not feasible due to the quickly growing number of degrees of freedom. Another approach is to simulate the scatter distribution as a superposition of Monte Carlo generated kernels (Spies et al. 2001), computed using semi-infinite slabs or water cylinders whose size is comparable to that of the object. For each detector pixel a kernel corresponding to the water-equivalent path length of X-rays impinging on that pixel is selected. In this way, however, the actual distribution of tissues along the path of the ray is neglected and the resulting scatter estimate is therefore only approximate. Moreover, the actual size of the scattering object is also largely neglected, which may result in an underestimation of the higher order scatter.

Monte Carlo simulation of scatter projections is a viable alternative to all the methods presented above. It is based on exact physical modeling, requires no simplifying assumptions about the shape or composition of the object, lets any order of scatter be modeled, does not rely on any cumbersome alterations to the scanner hardware and scanning protocols and can easily be adjusted to any scanner configuration. Practical implementation of a Monte Carlo based scatter correction scheme however requires a significant acceleration of the MC simulations. Previously it has been shown (Colijn & Beekman 2004) that noisy scatter estimates obtained with a low number of simulated photons can be accurately de-noised with a Richardson-Lucy (RL) fitting (Richardson 1972, Lucy 1974) performed separately on each projection. This allows the MC simulations to be accelerated by as much as two orders of magnitude without any loss of fidelity of the projections obtained. Since scatter distributions tend to change slowly with the projection angle (Ning & Tang 2004), further reduction in the required number of simulated photon histories can be expected if data from neighboring projections are used simultaneously during the fitting. On the basis of this observation, we develop in this paper an improved MC acceleration algorithm that we denote as 3D RL fitting.

The impressive acceleration achieved with 3D RL fitting paves the way for MC based scatter correction in cone-beam X-ray CT. Since initially the only available estimate of the object being scanned is its scatter contaminated reconstruction, we propose to perform Monte Carlo based scatter correction in an iterative manner. In the proposed scheme, Monte Carlo scatter estimation steps are interleaved with the computation of improved reconstructions. Furthermore, for the reconstruction steps of the scheme we propose to employ statistical algorithms designed to intrinsically correct for beam hardening effects (De Man et al. 2001, Elbakri & Fessler 2003). In this manner, simultaneous scatter and beam hardening artefact reduction are achieved.

The goals of the present paper are: (i) to introduce and validate the 3D Richardson-Lucy fitting-based Monte Carlo acceleration algorithm, (ii) to study the convergence properties of the

combined iterative scatter and beam hardening correction scheme and (iii) to prove the effectiveness of the proposed scheme in the simultaneous removal of scatter and beam hardening artefacts using experimental data.

6.2 Methods

6.2.1 System parameters and the Monte Carlo X-ray CT simulator.

A dedicated Monte Carlo simulator of X-ray photon transport (Colijn et al. 2004) is used throughout this study. The simulator is parameterized for a SkyScan1076 CCD-based micro-CT scanner. The same scanner is utilized for experimental validation of the correction scheme. The source-to-detector distance of SkyScan1076 is 172 mm, the distance from the rotation axis to the detector center is 51 mm. The detector measures 100x25 mm. The X-ray beam is collimated towards the active area of the detector, thus the fan-angle of the system is approx. $32\,^\circ$ and the cone-angle is approx. 8°. Both the measured and the experimental projection data-sets examined throughout this study cover a 180°+fan angle range with an angular step of 0.6°.

The energy spectrum of the X-ray tube used by the MC simulator is estimated from a set of attenuation measurements of Al slabs of varying thickness (Ruth & Joseph 1997). The detector efficiency for each ray is computed taking into account the attenuation properties of the scintillator. Up to 4th order scatter is included in the simulation; higher orders were found to contribute to less than 1% of the detected scattered radiation (Colijn et al. 2004). During the simulation, photons are emitted from the source under an angle randomly selected from the range given by the fan- and cone-angles of the system. The photons are then traced within the whole voxelized object volume, also outside the primary beam. The point detector approach (aka. Forced Detection, FD, Williamson (1987), Kalos (1963), Leliveld et al. (1996)) is employed to achieve a basic speed-up of simulation.

6.2.2 Acceleration of Monte Carlo scatter simulation by 3D Richardson–Lucy fitting

In Colijn & Beekman (2004) we proposed to employ two-dimensional Richardson–Lucy (RL) fitting (Richardson 1972, Lucy 1974) to suppress noise inherent to scatter estimates obtained by MC simulations based on low number of traced photons. The advantages of using RL fitting for de-noising MC scatter estimates include robustness to noise, an ability to cope with truncated data, an inherent positivity constraint and simplicity of implementation. The RL algorithm is equivalent to the Maximum Likelihood-Expectation Maximization method used in emission tomography reconstruction, although the derivations and underlying assumptions of the two algorithms differ. The RL method itself comprises a general, iterative de-blurring method. It requires only knowledge of the blurring kernel involved and makes no assumptions about the noise in the measured data. In our case, the de-blurring is performed on MC-simulated scatter projections. It produces a virtual distribution of scatter sources that is then re-blurred to yield a noise-free scatter estimate. This re-blurring operation essentially composes the sought noise-free scatter distribution from a set of Gaussian basis functions. Gaussian kernels have been chosen not only because of their generality, but also because they are separable, which

means that N-dimensional filtering can be reduced to N consecutive one dimensional blurring operations. This significantly reduces the fitting time.

The 2D fitting exploits the *a priori* knowledge about the smoothness of individual scatter projections and uses 2D Gaussian basis functions to represent the scatter estimate. Since scatter projections tend to change slowly with the projection angle (further denoted as θ), 3D Gaussian kernels, extending both in the projection plane and in the angular direction, also form an accurate basis for decomposing the scatter distribution. The RL fitting can therefore be extended into the third - angular - dimension, identical to θ. Information from neighboring projections is now combined during the fitting. As will be demonstrated in Sec. 6.3.1, this results in an additional reduction in the number of photons required in the initial MC simulation. The estimator for scatter $\tilde{p}(x, y, \theta)$ (x, y are axial and trans-axial projection coordinates) is now calculated for all projections simultaneously by blurring the virtual scatter distribution $\lambda(x, y, \theta)$ with a three-dimensional Gaussian function $G(x, y, \theta)$, extending both in the projection plane and in the angular direction:

$$\tilde{p}(x, y, \theta) = G(x, y, \theta) * \lambda(x, y, \theta) \tag{6.1}$$

where $*$ denotes convolution. In the latter, σ_{xy} will denote the standard deviation of $G(x, y, \theta)$ in the in-plane directions and σ_θ will denote the standard deviation in the angular direction. Starting from a uniform underlying distribution, the values of λ_i are updated iteratively, according to the RL algorithm. The update for the underlying distribution after k iterations is:

$$\lambda^{(k+1)}(x, y, \theta) = \lambda^{(k)}(x, y, \theta) \frac{G(x, y, \theta) * (p(x, y, \theta)/\tilde{p}^{(k)}(x, y, \theta))}{\sum_{x,y,\theta} G(x, y, \theta)} \tag{6.2}$$

where $p(x, y, \theta)$ is the scatter distribution obtained with MC with a low number of photons. The term $\tilde{p}^{(k)}(x, y, \theta)$ is the sought low-noise estimate of the scatter projection after k iterations of 3D RL fitting.

In order to determine the standard deviation of the Gaussian kernel of the fit, the interplay between noise reduction and blurring of the genuine projection details has to be taken into account. Small kernels allow to model more precisely the high frequency components of the scatter field, but also increase the transfer of noise from the MC estimate into the RL fit. They are therefore beneficial only for fitting the results of MC simulations based on large number of photon tracks. On the other hand, larger kernels should be used to fit the results of very fast Monte Carlo simulations that contain low number of simulated photons. The number of iterations executed may also have influence on the amount of noise present in the fitting result, as the noise generally increases with the iteration number. For the case of 2D fitting, Colijn & Beekman (2004) contains a detailed study on the choice of optimal number of iterations and optimal value of σ_{xy} depending on the number of photons traced in the initial MC simulation. It also describes an experimental method that determines a minimal width of a point scatter response for a given system geometry. This width sets the lower bound for the value of σ_{xy}. In Zbijewski & Beekman (2004*b*), similar analysis is done for the choice of σ_z in 3D fitting. The values of the fit's parameters used throughout this study are based on the results presented in the two abovementioned papers.

6.2.3 Phantoms

Simulation studies were performed using a digital rat abdomen phantom. The phantom is approx. 25 mm long and thus covers the whole axial range of the detector. An approximate representation of a rat was obtained by scaling up a mouse phantom (Segars et al. 2003) to a width of 58.2 mm and a height of 54.5 mm. The object was segmented into seven types of tissue: soft tissue, bone, lungs, muscle, liver, blood and intestine. Fig. 6.1 shows an axial view of the

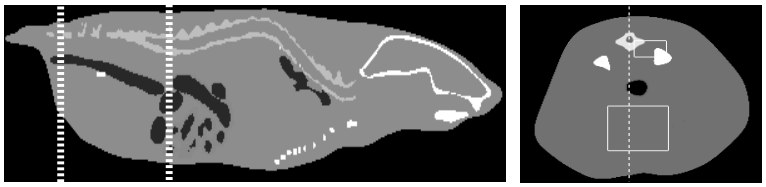

Figure 6.1: Left: central axial slice of a rat phantom with the abdomen section that was used in the simulations delimited with dashed lines. Right: central trans-axial slice of the abdomen section. Dashed line marks the position of an image profile examined in the sequel. Squares mark the ROIs employed for computation of the Mean Error. Gray-scale is 0.7-1.5.

whole phantom (left frame) and a trans-axial slice through the abdomen region that constitutes the simulation phantom (right frame). The borders of this region are delineated with dashed lines in the axial view.

In Fig. 6.2 the phantom used for real data experiments is shown. The phantom consists of a

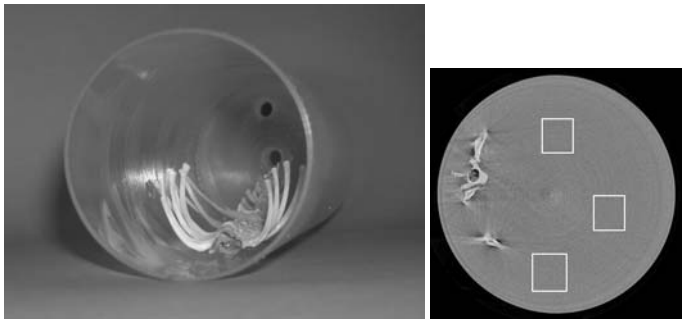

Figure 6.2: The phantom employed in the experimental validation of the scatter correction algorithm. The phantom consists of a rib cage of a rat placed in a PMMA casing. During the measurements the casing is filled with water. In the bottom row, reconstruction of the central slice of the phantom is shown with the location of the regions of interest that are examined in the sequel.

PMMA cylinder (diameter: 48.3 mm, length: 140.1 mm, casing thickness: 0.8 mm) containing the rib cage and the spine of a rat. For the measurements, the cylinder is filled with water. Since the water density is known, the phantom developed here makes it possible to quantitate the reconstruction accuracy. The presence of a rat skeleton ensures a highly realistic shape of

the scatter distribution and an authentic amount of beam hardening.

6.2.4 Assessment of accuracy and acceleration achieved with 3D RL fitting

Scatter projections of the abdomen phantom were obtained using the MC simulator with 10^3, 10^4, $5 \cdot 10^4$, 10^5, 10^6 and 10^7 photons/projection. The object grid was 256x256x90, the voxel size was 0.276 mm.

In addition, six almost noise-free reference scatter projections (at $0\,^\circ$, 42.6°, 84.0°, 126.6°, 171.6° and 212.4°) were computed with 10^9 photons; these projections were thereafter used as a gold standard.

Twenty iterations of three-dimensional Richardson–Lucy fitting with $\sigma_{xy} = 20$ and $\sigma_\theta = 15^\circ$ were executed on each of the scatter projection data sets (except for the gold standard). For comparison, the same data sets were also de-noised using 20 iterations of 2D RL fitting with $\sigma_{xy} = 20$. For each of the fits, a Normalized Mean Squared Error (NMSE) with respect to the reference projections was determined. The acceleration factor was calculated by comparing the number of simulated photon histories required to obtain an equal NMSE (averaged over all reference projections) with a basic Monte Carlo simulator (FD only) and with a Monte Carlo simulation followed by RL fitting.

6.2.5 Statistical reconstruction methods and scatter correction scheme

In all the experiments, the segmentation-free poly-energetic statistical reconstruction algorithm, further denoted as SR-POLY (Elbakri & Fessler 2003), was employed. This algorithm inherently corrects for beam hardening effects. During the reconstruction, iterations of SR-POLY were interleaved with cycles of scatter correction. Each scatter correction cycle consisted of the following steps:

1. MC simulation of the object's scatter based on the latest available reconstruction.
2. De-noising of the scatter estimates by 3D RL fitting.
3. Substitution of the fitting result as a background term in the update equation of SR-POLY and computation of a corrected reconstruction (previous reconstruction serves as a start image).

In order to accelerate the convergence of SR-POLY, it was initialized in each case with a reconstruction obtained by performing four iterations of the monoenergetic Ordered Subsets Convex (OSC) algorithm (Kamphuis & Beekman 1998*a*, Beekman & Kamphuis 2001, Kole & Beekman 2005*a*). To avoid beam hardening-induced cupping, the initial images were computed from water-corrected projection data. The OSC reconstruction was initialized from a start image consisting of a water cylinder having a diameter of 60 mm.

6.2.6 Validation of the scatter correction scheme

Table 6.1 summarizes different object and detector discretizations utilized in this part of the study. The ray-tracing was performed with the Siddon's algorithm (Siddon 1986) during both

	Ray-tracing: primary radiation		MC: scattered radiation	
	Object grid	Detector grid	Object grid	Detector grid
Simulation	512x512x180	500x125, 8x8 rays/pixel	256x256x90	500x125
Reconstr.: simulated data	256x256x90	500x125, 3x3 rays/pixel	256x256x90	500x125
Reconstr.: real data	512x512x180	1000x250, 3x3 rays/pixel	256x256x90	500x125

Table 6.1: Summary of various object and detector discretizations utilized during the validation of the MC-based scatter correction scheme.

the simulation and the reconstruction. In the ray-tracer, the spectral distribution of the X-ray tube and the detector efficiency were accounted for in the same manner as in the Monte Carlo simulator. For reconstruction, the data for the ray tracing in Table 6.1 refer to projection and back-projection steps of the statistical algorithm and the data for the MC simulation - to the scatter estimation steps. Wherever necessary, the detector subsampling has also been cited. The object voxel sizes were as follows: 0.138 mm for the 512x512x180 grid and 0.276 mm for the 256x256x90 grid. The detector pixel sizes were: 0.2 mm for the 500x125 grid and 0.1 mm for the 1000x250 grid. Both for simulated and for real data the reconstruction volumes covered the whole axial range of the detector.

- **Simulation study.** Poly-energetic primary radiation projections of the abdomen phantom were simulated using the ray-tracer described above. Scatter projections were estimated using MC simulation with 10^7 photons/projection. The object discretization used was coarser than the one used for ray–tracing (see Table 6.1), but, due to the predominantly low-frequency nature of scatter distributions, the scatter projections obtained do not differ markedly from the scatter projections of the finely sampled object. The scatter estimates were de-noised using the 3D Richardson–Lucy fit ($\sigma_{xy} = 10, \sigma_\theta = 3^\circ$, number of iterations: 20). Since the initial MC simulation included a relatively large number of traced photons, small RL kernel has been used to avoid over-blurring of the scatter estimates. The noise-free scatter distributions obtained in this way were added together with the scatter-free projections computed with ray-tracing. Poisson noise was generated in the final data set. Based on estimates obtained for the SkyScan1076 micro-CT scanner, it was assumed that the unattenuated photon flux was 1.5×10^6 photons per detector pixel.

  Four different reconstruction schemes were tested using the simulated projection data. All of them consisted of ten iterations of SR-POLY but differed in the number of scatter correction cycles executed: no scatter correction, scatter estimation only after first SR-POLY iteration (the estimate thus obtained was used in all subsequent iterations), scatter estimation after first and second SR-POLY iteration and scatter estimation after first, second and third SR-POLY iteration. The scatter-free projections obtained with ray-tracing were also reconstructed using ten iterations of SR-POLY. The final images obtained for different schemes were compared visually. Image quality was assessed using the Mean Error:

$$\mathrm{ME} = \frac{1}{N} \sum_{k=1}^{N} |(\tilde{\mu}(k) - \mu(k))| \tag{6.3}$$

  where $\mu(k)$ and $\tilde{\mu}(k)$ are the k–th pixel value in the phantom and in the reconstruction, respectively. ME was computed for two Regions of Interest (ROIs) shown as white squares in Fig. 6.1. One of the ROIs contained only soft tissue (ROI-SOFT), the other combined bone and soft tissue areas (ROI-BONE). Mean Errors in both ROIs were computed for the central and the 60th slice of the reconstructions. The 60th slice marks approximately the border of a region free of any obvious cone-beam artefacts.

  During the reconstructions of simulated data, the set of base substances for SR-POLY included bone and soft tissue. Ordered Subsets acceleration was applied (71 subsets of 5 projections). MC simulations used $5 \cdot 10^4$ photons/projection. Scatter estimates were smoothed using 20 iterations of 3D RL fitting with $\sigma_{xy} = 20$ and $\sigma_\theta = 15^\circ$.

- **Experimental study.** The physical phantom was scanned without the scanner's bed. The X-ray high voltage was set to 100 kVp and projections were recorded over a $180\,^{\circ}$+fan angle range in steps of 0.6°. Prior to the scanning of the phantom, dark (collected with the X-ray tube off) and white (with the X-ray tube on) reference fields were acquired. For each projection angle, the dark field frame was subtracted from both the projection data and the white field in order to remove the offset arising from the dark current of the detector. Subsequently, each offset-corrected projection was normalized using the offset-corrected white field.

  On the basis of the results obtained for the simulated data, we chose for real data a scheme with two cycles of scatter estimation. The set of base substances for SR-POLY consisted of bone and water. All other details of the reconstruction work-flow were the same as in the simulation study. Visual comparison was performed between the final images obtained with and without the scatter correction. Reduction in the magnitude of the cupping artefact was also quantified. To this end, the mean density of water was computed for a union of three ROIs depicted in the right panel of Fig. 6.2. The ROIs extended over the central 60 slices of the reconstructions. Image profiles were also examined.

6.3 Results

6.3.1 Validation of Monte Carlo acceleration by means of 3D Richardson-Lucy fitting

The top frame of Fig. 6.3 shows a gold standard, noise-free scatter projection for the projection angle of 0°. It was computed by tracing 10^9 photons with a Monte Carlo simulator accelerated only by Forced Detection. Compared to this reference distribution, the results displayed in the second row of Fig. 6.3, which were obtained by simulating 10^4 and 10^5 photons/projection, are substantially noisier. Application of the 3D Richardson-Lucy fitting to these noisy projections dramatically reduces their variance, allowing the underlying noiseless scatter distribution to be extracted accurately, as depicted in the third row of images. The agreement between reference projection and the result of 3D RL fitting is already very good for the initial simulation with 10^4 photons and almost ideal for 10^5 photons, as demonstrated by image profiles in the bottom row of Fig. 6.3. The Richardson-Lucy fitting provides accurate results even at the edges of the detector, where data truncation occurs. It also copes well with the truncation in the angular direction; this is clear from the projection displayed here, which is the outermost one in the dataset. Fig. 6.4 shows the acceleration factor attained by 3D (dashed line) and 2D (solid line) RL fitting. Circle corresponds to the result from Fig. 6.3 obtained with initial MC with 10^4 photons/projection, diamond corresponds to the result obtained with 10^5 photons/projection. Depending on the required accuracy, 3D RL fitting can accelerate the MC simulation by as much 3-4 orders of magnitude. Over most of the investigated NMSE range, 3D fitting results in acceleration factors at least an order of magnitude larger than those achieved by 2D fitting. Acceleration curves for 2D and 3D fitting converge for the lowest values of NMSE. This region corresponds to the case of accurate initial Monte Carlo simulations, generated with large numbers of traced photons. As already mentioned in Section 6.2.2, smaller kernels (ie. a 2D RL) are beneficial for such

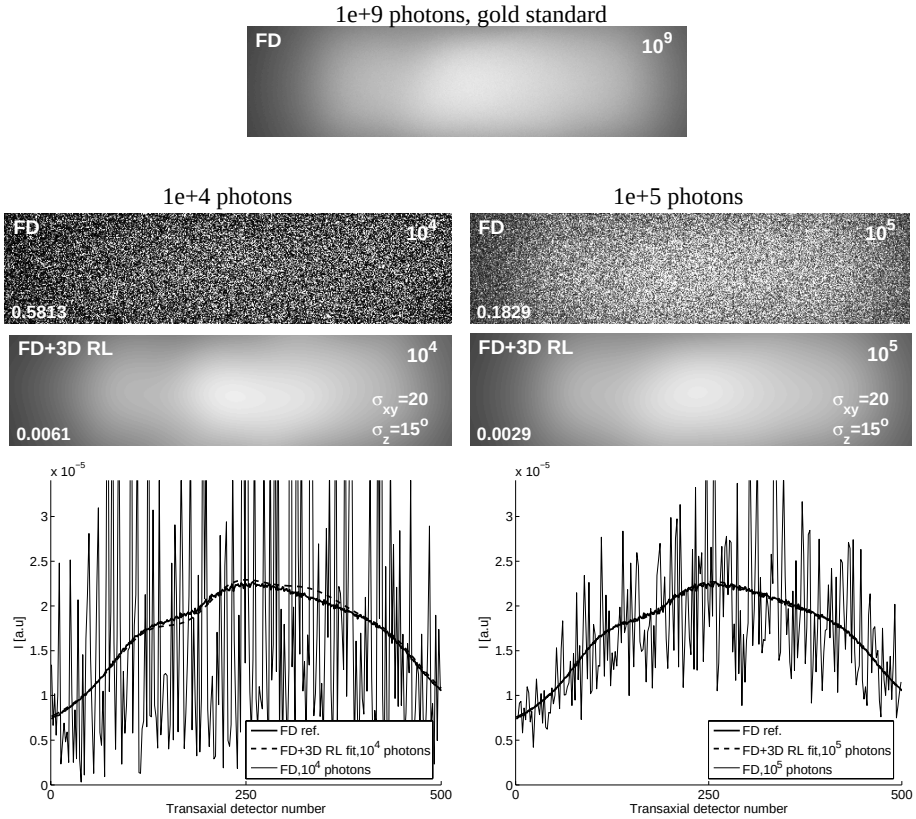

Figure 6.3: By combining fast Monte Carlo (low numbers of photon histories) with 3D Richardson-Lucy fitting, noise-free scatter estimates can be obtained 3-4 orders of magnitude faster than with standard methods. Top frame: reference scatter projection (angle: 0°) obtained with plain MC using 10^9 photons/projection. Left column: results obtained with plain MC (first row) and with MC+3D RL fitting (second row) for MC simulation with 10^4 photons/projection. The fitting accurately extracts the true scatter distribution from the noisy simulation result. Right column: results obtained with and without 3D RL fitting for MC simulation with 10^5 photons/projection.

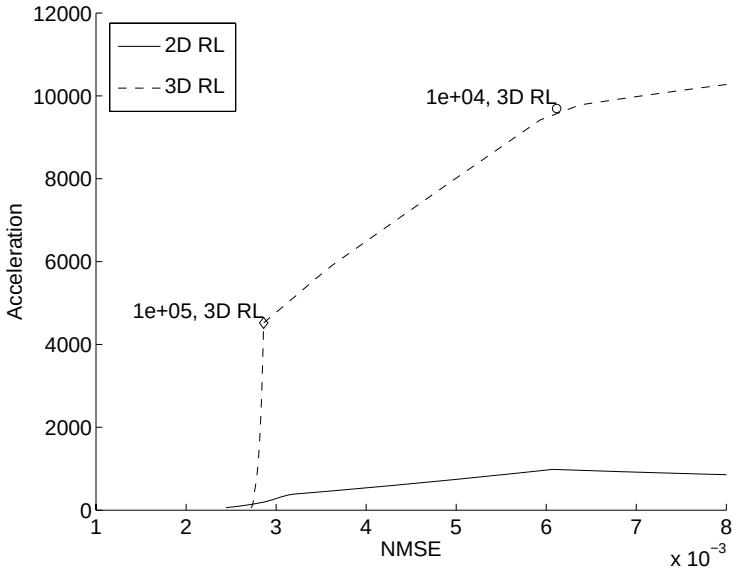

Figure 6.4: Acceleration achieved in MC estimation of scatter projections by using 2D and 3D Richardson–Lucy fitting. Circle corresponds to the result from Fig. 6.3 obtained with initial MC with 10^4 photons/projection, diamond corresponds to the result obtained with 10^5 photons/projection.

low-noise MC estimates because they introduce less blurring and thus provide lower errors of the fit for a given number of photons and a larger acceleration for a fixed NMSE value.

6.3.2 Validation of Monte Carlo based iterative scatter correction scheme.

Fig. 6.5 shows trans-axial slices through various reconstructions of the abdomen phantom. The poly-energetic statistical algorithm effectively removes the cupping caused by beam-hardening, as shown by the reconstruction of the scatter-free projections displayed in frame (a) of Fig. 6.5. When scatter-contaminated projections are reconstructed and only beam-hardening compensation by SR-POLY is included, additional cupping caused by scatter becomes apparent, as demonstrated in frame (b). This artefact is removed accurately by performing MC-based scatter correction (frames (c) and (d)). One cycle of the correction is sufficient to yield a final image that is almost indistinguishable from the reconstruction of the scatter-free data. Fig. 6.6 shows profiles through the slices presented in Fig. 6.5. Frame (a) proves that cupping caused by the scatter leads to a reconstruction error of more than 10% in the center of the phantom. This error is almost completely reduced after only one cycle of the scatter correction is applied, as is demonstrated in frame (b). Table 6.2 compares Mean Errors for the two ROIs selected in the final reconstructions. The central soft tissue region (ROI-SOFT) is most severely degraded by the cupping caused by the scatter. For this area, one cycle of correction reduces ME by more than one orders of magnitude as compared to the case where no correction has been applied. For both the central and the off-center slice the reconstruction errors attained after two cycles of

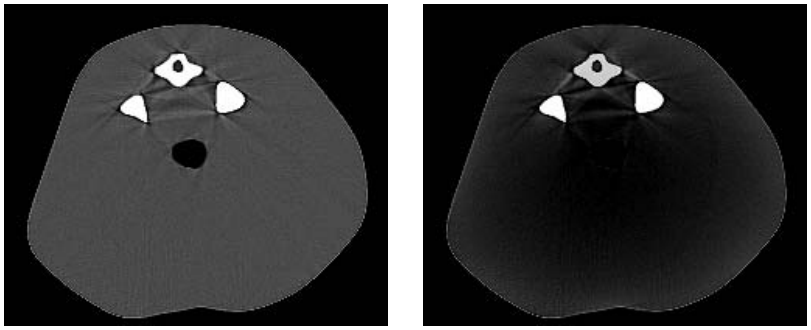

(a) no scatter (b) scatter, no correction

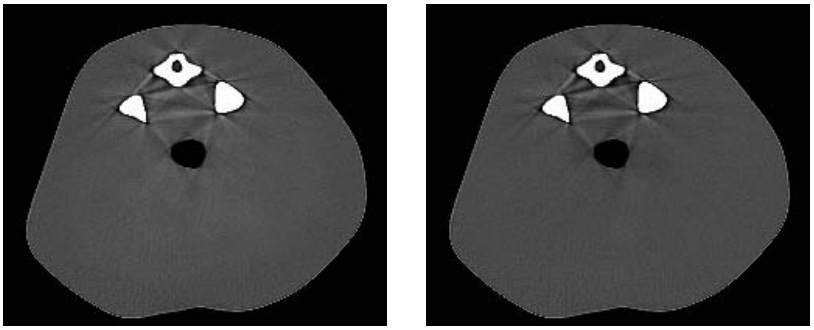

(c) scatter, 1 cycle corr. (d) scatter, 2 cycles corr.

Figure 6.5: Simultaneous scatter and beam-hardening correction can be achieved for X-ray CT data by combining statistical reconstruction methods and fast Monte Carlo simulations. Reconstructed images for simulated projection data: (a) reconstruction of scatter-free projections (gold standard). Subsequent images demonstrate the reconstructions of scatter contaminated projections for the following correction schemes: (b) no scatter correction, (c) scatter estimation after first of ten iterations of SR-POLY and (d) scatter estimation after first, second and third of ten iterations of SR-POLY. Gray-scale is 0.9–1.4 g/cc.

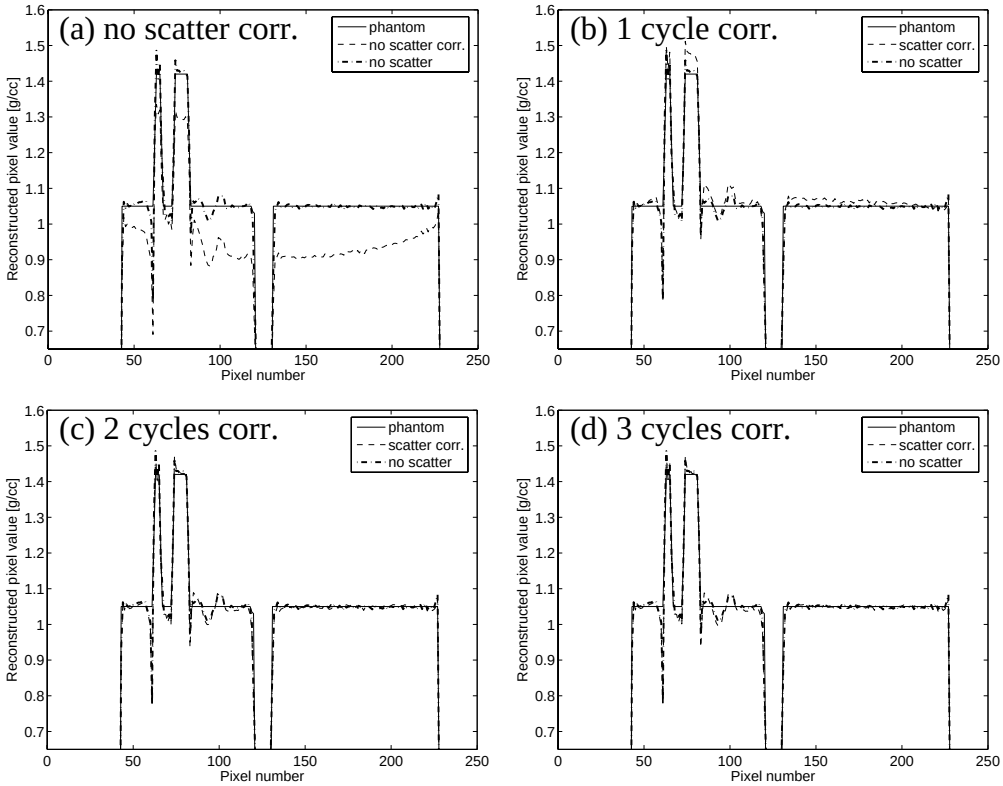

Figure 6.6: Comparison of vertical profiles taken through the images from Fig. 6.5. In each frame profile through the phantom, through a reconstruction of scatter-free projections and through a reconstruction of scatter-contaminated data are compared for different numbers of scatter estimation steps executed during ten iterations of SR-POLY. One cycle of Monte Carlo-based correction is sufficient to remove most of the cupping caused by scatter.

	Central slice				
	No scatter (gold standard)	With scatter			
		No correction	1 cycle corr.	2 cycles corr.	3 cycles corr.
$ME_{ROI-BONE}$	0.034	0.139	0.046	0.040	0.040
$ME_{ROI-SOFT}$	0.006	0.129	0.007	0.006	0.006

	60th slice				
	No scatter (gold standard)	With scatter			
		No correction	1 cycle corr.	2 cycles corr.	3 cycles corr.
$ME_{ROI-BONE}$	0.039	0.143	0.048	0.043	0.043
$ME_{ROI-SOFT}$	0.008	0.124	0.009	0.009	0.009

Table 6.2: Mean Errors for two ROIs selected in the images reconstructed from simulated data. Top table: Mean Error for the central axial image slice. Bottom table: ME for the 60th axial slice through the reconstruction. Application of even one cycle of scatter correction dramatically reduces the errors as compared with the case of no scatter correction. Subsequent correction cycles reduce the error further towards the values obtained for scatter-free data. Adequate correction is achieved both in the center and at the peripheries of the reconstructed volume.

the correction are remarkably close to the errors in the reconstructions of scatter-free data. This proves that the scatter-related artefacts have been removed almost completely. Adding one more cycle of scatter correction leads to only slight further improvement.

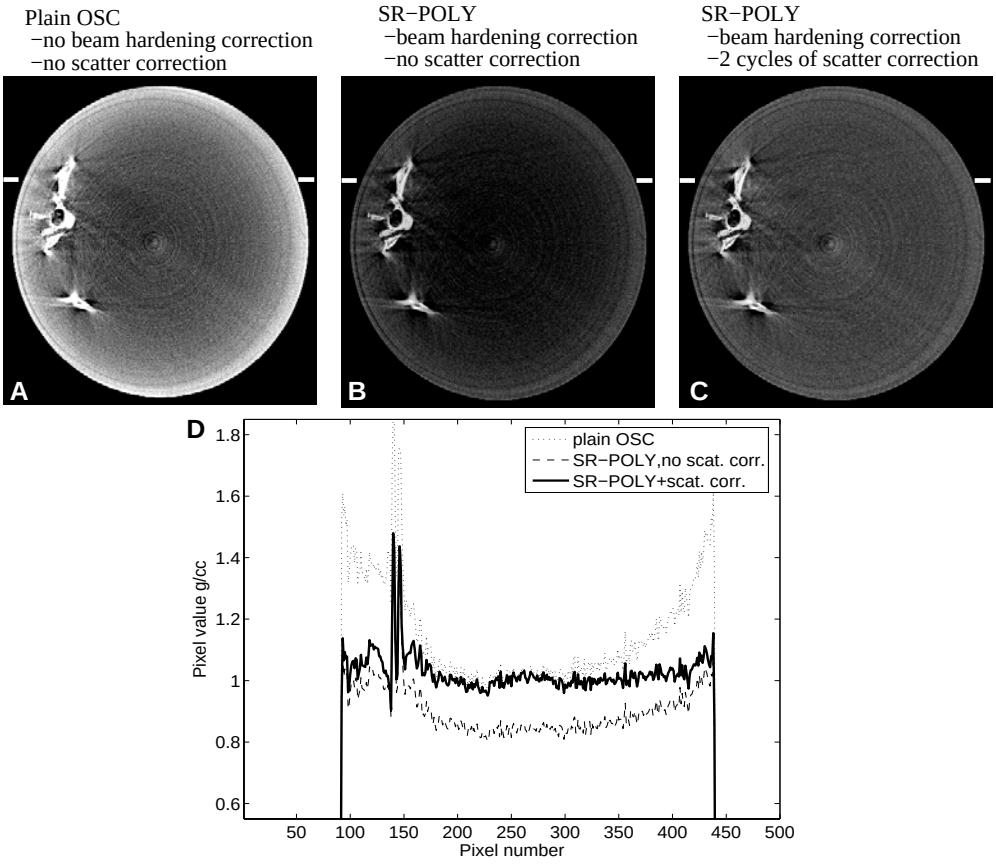

Figure 6.7: Quantitative improvement achieved by simultaneous scatter and beam hardening correction is demonstrated here for real data. Top row: reconstructed trans-axial slices through a water cylinder containing rat's rib cage. Frame A: 10 iterations of plain OSC algorithm with no beam hardening correction and no scatter correction. Frame B: 10 iterations of SR-POLY with no scatter correction. Frame C: 10 iterations of SR-POLY with two cycles of scatter correction embedded. White lines denote the location of image profiles presented in Frame D. Gray-scale is 0.8–1.6 g/cc.

Fig. 6.7 shows trans-axial slices taken through the reconstructions of real data. The left frame displays the reconstruction computed with plain OSC algorithm, ie. with no beam hardening correction and no scatter correction. This image is severely polluted by cupping and streak artefacts. The central frame of Fig. 6.7 shows the reconstruction obtained with SR-POLY algorithm, but with no scatter correction. As the SR-POLY algorithm inherently corrects for the beam-hardening artefacts, all the cupping present in this image can be ascribed solely to scatter.

The right frame of Fig. 6.7 displays the result of SR-POLY with two cycles of MC-based scatter correction embedded. All the cupping is effectively removed from the reconstruction. The attached image profiles prove the uniformity of the resulting reconstruction and the improvement in the quantitative accuracy as compared with the plain OSC reconstruction and with the SR-POLY reconstruction with no scatter correction. For the SR-POLY reconstruction with no scatter correction, the average water density in the three ROIs (see Sec. 6.2.6) was 0.88 $\frac{g}{cm^3}$. After MC-based scatter correction, the mean reconstructed water density was 1.01 $\frac{g}{cm^3}$, close to the true value of 1 $\frac{g}{cm^3}$. When the scatter correction is used, the reconstruction error of water density values is reduced from about 12% to only 1-2%.

The examination of rat-sized objects in the SkyScan1076 scanner requires a broadening of the effective field-of-view above the limit imposed by the size of the CCD camera. This is achieved by performing two separate scans, each of them with the camera shifted to either side of the desired field-of-view. The half-projections obtained are stitched together prior to the reconstruction. This stitching causes the dip-like feature in the center of both reconstructions. Although the system was very precisely calibrated, some source instabilities could not be completely corrected for, resulting in flux differences between the half-projections. These flux differences caused the above-mentioned artefacts. The ROIs for the computation of water density were selected so that there was no interference with the artefact pattern.

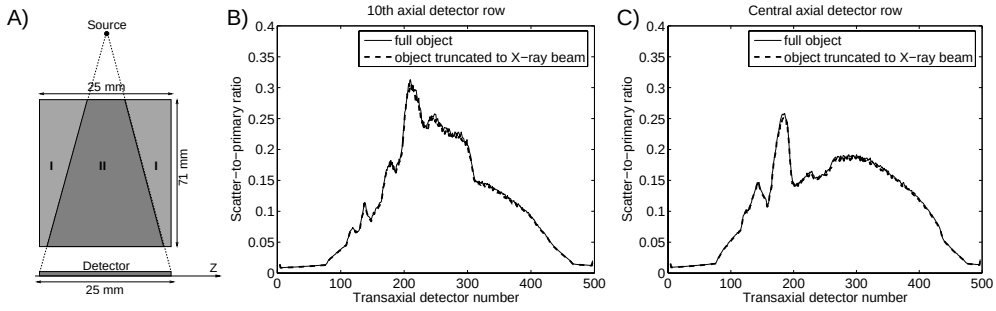

Figure 6.8: Scatter-to-primary ratios (SPRs) comparison between a Monte Carlo simulation with the whole object (I+II) included and a MC simulation with the object truncated to the area covered by the X-ray beam (only II). Single projection at an angle of 0°. Frame A: an axial view of the system setup. The dark area corresponds to the truncated object. Frame B: SPR for the 10th axial detector row. Frame C: SPR for the central axial detector row.

Finally, Fig. 6.8 compares the scatter-to-primary ratio for MC simulation including the whole object volume (default throughout the study) with the SPR computed from MC simulation with photon tracing restricted to the area covered by the primary X-ray beam. In both cases the abdomen phantom discretized on a 256x256x90 grid was used and 10^9 photons were traced to simulate a single projection at an angle of 0°. The SPR estimates obtained from the full and from the truncated volume are almost identical, independent on the axial projection row. This indicates that the contribution of photons scattering from outside the field-of-view to the total scatter field is only minor.

6.4 Discussion

Adding the angular dimension to the RL fitting exploits *a priori* knowledge about the smoothness of noiseless scatter distributions as a function of projection angle. As a result, simulation of $10^4 - 10^5$ photons/projection is now sufficient to arrive at scatter estimates that have the same accuracy as those obtained using $10^7 - 10^9$ photons when MC is supported only by Forced Detection. This corresponds to a three-to-four orders of magnitude reduction in the computation time as compared with a standard Monte Carlo. Moreover, we have shown that the fitting procedure yields accurate results even for the outermost projections in the dataset and for truncated scatter distributions. Finally, if parallelized, both the MC simulation and the RL fitting would scale almost linearly with the increase in the number of available processors. Due to these desirable properties, the proposed combination of rapid MC simulation and 3D Richardson-Lucy fitting is very well suited for efficient and accurate corrective reconstruction in transmission X-ray imaging. Contrary to the other possible approaches to scatter estimation, our method is not based on any simplifying assumptions about the scattering process or the object shape and composition and does not require any modifications of the scanner design.

Thanks to the significant acceleration of MC simulation achieved by the 3D RL fitting, the computation of scatter estimates is no longer a computational bottleneck for the iterative scatter correction scheme proposed in this paper. In the examples presented, only $5 \cdot 10^4$ photons per projection were simulated in each scatter estimation step, which corresponds to computation times of about two minutes per a scatter projection on a dual 2.6 GHz Xeon PC (including the 3D RL fitting). The total time required for two cycles of scatter correction constituted only 10% of the total reconstruction time. Excellent correction results were achieved. For simulated data, only minor differences between the reconstructions of scatter-free and scatter-contaminated projections can be perceived after one cycle of the correction scheme. Two cycles of the scheme are sufficient to achieve almost complete removal of scatter-related artefacts.

For real data, the error in the quantitation of water density is improved from 12% for reconstructions without any scatter correction to only 1% after two iterations of the scatter correction. The uniformity is also significantly improved in the scatter-corrected image; the remaining non-uniformities are mainly caused by the stitching of half-projections performed in SkyScan1076 scanners to broaden the field of view.

Three dimensional Richardson-Lucy fitting allows to extract truthful scatter estimates from noisy results of fast MC simulations. In the current setup the only mechanism used to speed-up the Monte Carlo photon transport was the Forced Detection method. Other possible techniques that might be employed to accelerate the MC scatter simulation include: (i) using of even coarser object voxelizations during the MC simulation, (ii) re-use of photon tracks from the previous scatter estimation cycles (Beekman et al. 2002), (iii) application of a correlated Monte Carlo approach, where photon weights obtained in a MC simulation of an uniform object are transformed to describe the scattering in a non-uniform medium (Beekman et al. 1999); this method requires the knowledge of the object's outline which is usually available in CT imaging, and (iv) the use of a δ-scattering technique (also known as a fictitious cross section method or a Woodcock scheme, Kawrakow (2000)), which allows to neglect tissue boundaries during photon tracing through a voxelized object. Some of those methods can be combined together and especially in this case a further significant reduction in the MC simulation time can be expected.

One of the potential problems for a simulation-based scatter correction is that for cone-beam

acquisitions the projection dataset is incomplete outside the central plane. The resulting cone-beam artefacts obviously lead to errors in the scatter estimates obtained with MC. Our simulation results demonstrate however that these errors have almost no influence on the quality of scatter correction: adequate correction has been achieved also for image slice that was very close to the area polluted by cone-beam artefacts (see Table 6.2). Another possible source of errors in the simulated scatter distributions is that no reconstruction is available for the peripheral regions of the object, which are completely outside the X-ray beam. As however shown in Fig. 6.8, the scattered photons coming from the areas outside the X-ray beam have only minor influence on the SPR. The lack of truthful reconstructions in these areas does therefore not constitute a major problem for the MC-based scatter correction method. In our case the regions where no reconstruction was available were filled in by the start image. The results from Fig. 6.8 indicate, however, that the area where the simulation takes place does not have to be extended outside the scanners field-of-view in order to achieve scatter estimates accurate enough for the correction.

The validation study presented here was restricted to micro-CT imaging. We expect that the proposed method can also be applied to clinical CT, if the MC simulator is adapted to handle the specific detectors, collimation and other design details of the clinical scanners. Scatter is becoming an issue of concern for helical multi-slice scanning, since the current trend there is to increase the number of detector rows. Another modality that may require some form of scatter correction is flat-panel cone-beam CT, where scatter-to-primary ratios in excess of 100% have been reported (Siewerdsen & Jaffray 2001). In general, the relative contribution of scatter component to the projections and its variablity can be expected to be even larger in human imaging than in micro-CT. Highly accurate scatter estimates will therefore be required for scatter correction. Our method, based on rapid but precise Monte Carlo simulation, seems to be perfectly suited for this application.

6.5 Conclusions

This paper introduces a dedicated acceleration technique that allows the Monte Carlo computation of X-ray CT scatter distributions to be speeded up by as much as four orders of magnitude. This means that MC simulations can be included in an image reconstruction and post-processing chain without leading to a dramatic increase in the overall processing time. By combining accelerated Monte Carlo simulations and statistical reconstruction methods, simultaneous and efficient correction of scatter and beam hardening artefacts has been achieved for cone beam X-ray CT imaging. To our knowledge, this is the first time that such a successful correction of all main photon-transport-related image-degrading effects has been experimentally demonstrated for cone-beam CT.

Acknowledgments

We would like to thank Dr. Alexander Sasov from SkyScan for his kind support with the measurements and to him and to Dr. Xuan Liu from SkyScan for many useful discussions.

Chapter 7

Statistical reconstruction for X-ray CT systems with non-continuous detectors

Abstract

We analyse the performance of statistical reconstruction (SR) methods when applied to X-ray projection data collected with non-continuous detectors. Robustness to projection gaps is required in some X-ray CT system designs based on multiple detector modules. In conventional scanners, miscalibrated or faulty detector pixels may also lead to projections that contain discontinuities. In such situations, the advantage of statistical reconstruction is that it simply ignores the missing or faulty projection data and makes optimal use of available line integrals. Here, we assess the performance of SR for circular orbit, cone-beam X-ray CT systems with detector discontinuities. SR is applied to projection data obtained for various configurations of detector gaps and various angular scanning ranges. We show that if the locations of detector discontinuities and the scanning range are chosen in a way ensuring complete object sampling in the central imaging plane, SR results in images free of any noticeable gap-induced artefacts throughout the whole reconstructed volume. SR obviates the need to fill the sinogram discontinuities by interpolation or any other pre-processing techniques.

7.1 Introduction

A large fraction of research and development in tomographic imaging is devoted to increasing the volume coverage and resolution of the images obtained and to decreasing the associated scanning time. One of the approaches that may make it possible to achieve these goals simultaneously is to utilise modular detector setups that will combine into one large-area camera some of the currently available high resolution, high speed, but small field-of-view detectors. The use

of such a design will reduce the need to re-design detectors and their electronics. In PET imaging, the High Resolution Research Tomograph (HRRT, Wienhard et al. (2002), de Jong et al. (2003)) is an example of a system incorporating cost-effective panel detector modules which has helped to achieve breakthroughs with regard to image resolution.

In this article we will focus on transmission tomography systems. One of the modalities that may benefit greatly from the use of modular detector technology is X-ray micro-CT imaging. Most of the currently available micro-CT systems utilise detectors based on cooled CCD cameras coupled to a scintillation screen by means of a fibre-optic taper or plate. This technology has some important advantages, such as very good stability; on the other hand, resolution in such systems is limited because of blurring introduced by fibre optic tapering (Goertzen et al. 2004). The detection efficiency at low exposures is hampered, because phosphor screens have to be kept thin in order to reduce the light spread. Furthermore, light losses occur also in the fibre optic tapers. As a result, large radiation doses are required if high resolution imaging is to be achieved. These problems could be reduced by employing fast, electron-multiplying CCDs (EMCCDs) connected via a fibre-optic plate (straight tapering to reduce blurring) to high resolution, columnar CsI scintillation crystals. Such crystals are characterised by excellent resolution, high capture fraction and light output, which makes them attractive for X-ray imaging (Nagarkar et al. 1996, Nagarkar et al. 2004, de Vree et al. 2005). EMCCDs provide low read-out noise even at high frame rates, which might allow for a reduction of the required radiation dose and create possibilities for dynamic (eg. cardiac) small animal imaging (Jerram et al. 2001, Hynecek 2001, Robbins & Hadwen 2003, Nagarkar et al. 2004, de Vree et al. 2005, Beekman & de Vree 2005). A potential limitation of this technology is that large-area electron multiplying CCDs are difficult to manufacture. EMCCDs providing fields-of-view sufficient for rat imaging are therefore currently unavailable. Moreover, if low read-out noise is required, the achievable frame rate decreases with increasing CCD surface. Building detectors out of many units based on single, small field-of-view EMCCD chips will allow to overcome this size limitation.

One of the many other potential applications of modular detector technology are systems based on the Medipix2 CMOS hybrid pixel detectors (Llopart et al. 2002, Medipix2 Collaboration 2005). These chips make it possible to perform single-photon counting even at high beam intensities and to carry out energy-weighted imaging (Karg et al. 2005). Currently, however, Medipix2 detectors provide active areas of only about 2 cm^2. Fields-of-view required in animal imaging can only be achieved by combining many Medipix2 chips into one modular detector.

In systems based on modular detectors, the interfaces between detector modules can result in discontinuities in the projections recorded. Such gaps in object coverage may pose a serious challenge for reconstruction algorithms. In the case of HRRT, bilinear interpolation of data within the gaps proved to be sufficient to significantly improve image quality when Fourier rebinning and 2D Ordered Subset Expectation Maximization were used for reconstruction (de Jong et al. 2003). A further improvement in quantitative accuracy was achieved when interpolation of missing projection data was followed by reconstruction of an intermediate volume. This volume was later re-projected to produce a better estimate of line integrals corresponding to detector discontinuities. It should be noted that the location of gaps within the sinogram of HRRT is completely different from the configuration investigated in this paper. Moreover, object sampling and requirements regarding image resolution in PET differ significantly from

those encountered in X-ray CT.

The projection discontinuities may be filled by applying consistency conditions satisfied by Radon transforms (Natterer (1986), Kudo & Saito (1991), Chen & Leng (2005), Patch (2002) and references therein), instead of simple interpolation. An example of consistency condition fulfilled by 2D parallel beam projections is that the total attenuation measured in each projection should be a view-independent constant. In 3D, an ultra-hyperbolic integral equation must be satisfied by the measured line integrals (the so-called John's equation, John (1938)). The consistency conditions were applied in the completion of truncated projections (Hsieh et al. 2004) or when projections corrupted by opaque structures in the object were considered (Kudo & Saito 1991). It remains to be seen how well will they perform for the case of non-continuous, modular detectors. Chen & Leng (2005) obtained some results that are directly applicable to this situation. The method proposed by them is limited to fan-beam projection data. Although a significant reduction of gap-induced artefacts was achieved, some noticeable errors were still visible in the images presented.

Statistical reconstruction (SR) methods seem to be perfectly suited for application to systems equipped with modular detectors. Some of the well-known advantages of SR that may find use in wide field-of-view, high resolution, low noise X-ray CT imaging include: (i) greater flexibility with respect to the choice of image acquisition geometries and thus the placement of detector modules, (ii) reduced vulnerability to cone-beam artefacts (Thibault et al. 2005), (iii) the ability to incorporate precise models of photon transport, which allows for suppression of beam-hardening and/or scatter-induced artefacts (De Man et al. 2001, Elbakri & Fessler 2002, Zbijewski & Beekman 2006) and (iv) the potential to reduce the imaging dose required to achieve a given resolution-noise trade-off (Zbijewski & Beekman 2004*a*, Ziegler et al. 2004). Most importantly, since statistical reconstruction is not based on analytical inversion formulas, but on detailed system modelling, SR has shown itself to be more immune than analytical methods to problems arising from insufficient object sampling (Manglos 1992, Michel et al. 2005). This suggests that if SR is applied to non-continuous projections, images with greatly reduced gap-related artefacts can perhaps be reconstructed without any interpolation or other pre-processing in the sinogram domain.

The problem of detector discontinuities is not limited to scanner designs based on modular detectors. In any system configuration, faulty or miscalibrated detector pixels may lead to non-continuous projection images. In 3D cone beam CT, faulty detectors result not only in ring artefacts located in a single image slice, but also in streaks that cross a number of adjacent slices (Tang et al. 2001). Currently, the suppression of these errors is achieved either by pre-processing of the sinograms (Rivers 1998, Tang et al. 2001) or by post-processing of reconstructed images (Sijbers & Postnov 2004, Riess et al. 2004). Both approaches influence the entire reconstructed image, thereby reducing its fidelity. Since a faulty detector pixel may be treated as a special case of detector gap, SR may obviate the need for pre- or post-processing of projections also in this case.

The aim of the present paper is to investigate the efficacy of statistical reconstruction for cone-beam X-ray micro-CT systems containing detector gaps. The circular setup analysed here is particularly challenging, since the reconstruction algorithm has to deal not only with data missing due to detector gaps but also with projection incompleteness inherent to circular cone-beam imaging geometry. In this paper, various configurations of detector discontinuities are

tested and three different angular scanning ranges are considered. In this way datasets with varying amounts of non-recoverable missing data are generated and the performance of SR for each of these cases is assessed. Guidelines regarding the placement of detector discontinuities yielding optimal SR performance are derived from the results obtained.

7.2 Methods

7.2.1 Phantom and simulation

Micro-CT projections of a digital phantom approximating the rat abdomen (Fig. 7.1) were simulated. The phantom was derived from a digital mouse phantom (Segars et al. 2003) by scaling it

(a) Phantom, central slice **(b) Phantom, off-centre slice**

Figure 7.1: The phantom used in the simulations. Panel *a*: central slice. Panel *b*: the outermost slice, located 5.5 mm from the centre. Grey scale range is 0.85-1.6 $\frac{g}{cm^3}$; the range was selected to emphasise the soft-tissue structures. The boxes mark the locations of regions used for Mean Error calculations.

to the size of a rat (width: 58.2 mm, height: 54.5 mm). The densities of the tissues composing the phantom were as follows: body: 1.05 $\frac{g}{cm^3}$, intestines: 1.03 $\frac{g}{cm^3}$, substance filling the intestines: 0.3 $\frac{g}{cm^3}$, spine: 1.42 $\frac{g}{cm^3}$, other bones (the hips): 1.92 $\frac{g}{cm^3}$. The phantom was discretised onto a 1024x1024x160 grid having a voxel size of 0.069 mm. This simulation grid was 64 times denser than the target reconstruction grid; a voxelisation this fine was previously found more than sufficient to make an adequate estimate of real density distributions (Goertzen et al. 2002). The phantom was completely contained within the X-ray beam of the simulated micro-CT system. The projections were computed by ray-tracing based on Siddon's algorithm (Siddon 1986). A mono-energetic X-ray beam with energy of 38 keV was assumed; detector efficiency was not included in the simulation. System dimensions were as follows: source-to-detector distance equal to 172 mm, source-to-centre-of-rotation distance equal to 121 mm. The detector consisted of 500x125 elements, the pixel size being 0.2 mm. Sub-sampling of 6 rays per detector element was used during the simulation. Six hundred projections were computed over a full circle. After the simulation, Poisson noise was generated in the projections; $1.5 \cdot 10^6$ photons/detector pixel in an unattenuated X-ray beam were assumed.

The cone-angle of the centre of the outermost slice of the phantom was $2.6\,^\circ$. For statistical reconstruction, this axial location corresponds approximately to the outer border of a region free of any visible cone-beam artefacts.

7.2.2 Gap configurations

Three detector configurations were tested: (i) a continuous detector with no gaps, (ii) a non-continuous detector with two 4 mm long gaps placed symmetrically around the central ray and (iii) a detector with two 4 mm gaps placed asymmetrically around the central ray. In the latter case, both discontinuities were shifted by 2 mm with respect to their placement in the symmetric configuration. In this way, it was assured that there was no overlap between one gap and a mirror image of the other gap computed with respect to detector centre. In the case of both non-continuous detectors, the distance between the gaps was 35 mm. The trans-axial location of each gap was the same for every detector row. Fig. 7.2 shows sinograms for the central detector row for the two non-continuous detector configurations. The locations of the gaps were selected such

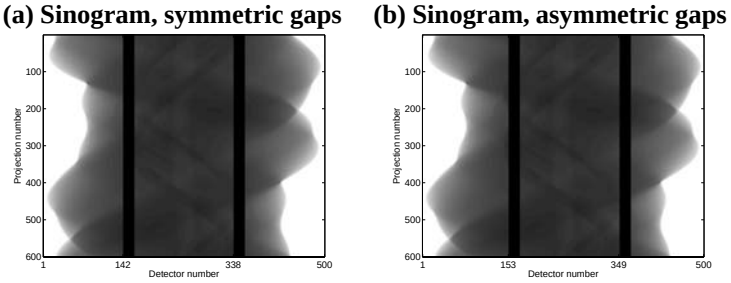

Figure 7.2: Panel *a*: sinogram of the phantom for the symmetric configuration of the gaps, central detector row. Panel *b*: sinogram for the asymmetric configuration of gaps, central detector row.

that they partially coincided with the projections of bony structures of the digital rat abdomen phantom.

7.2.3 Image reconstruction

The performance of statistical reconstruction in the presence of detector gaps was tested by applying to the simulated projections the Ordered Subsets Convex (OSC) algorithm (Kamphuis & Beekman 1998*a*, Erdoğan & Fessler 1999, Beekman & Kamphuis 2001, Kole & Beekman 2005*a*). OSC combines the Convex algorithm (Lange 1990) with acceleration strategy based on the concept of Ordered Subsets (OS) (Hudson & Larkin 1994). In OS reconstructions, only one subset of projections at a time is used for updating the image estimate, and this update together with a different subset of projections is then used to calculate the next update. By definition, *an entire iteration n of OSC is completed when all subsets have been processed once*; this takes roughly the same processing time as one iteration with the standard Convex algorithm.

Three different angular ranges of scanning were considered: (i) a full-scan, comprising 600 projections and taken over a 360° range, (ii) an over-scan, comprising 480 projections and covering a range of 288° and (iii) a short-scan, comprising 360 projections and covering a range of 216°. In the latter case, the scan contained five more projections than required by the short-scan condition of 180°+fan angle. By slightly increasing the angular range, greater flexibility was

achieved with respect to the possible subset choices. For each projection dataset, 60 subsets were used and 50 iterations of reconstruction were executed.

The reconstruction grid used in SR consisted of 512x512x80 voxels. As in the simulation, ray-tracing through the grid was performed with Siddon's algorithm; a sub-sampling of 4 rays per detector pixel was utilised. The reconstructions obtained were subsequently folded onto a 256x256x40 grid (voxel size: 0.276 mm) by averaging assemblies of eight voxels. Reconstructing on a fine grid followed by rebinning removes edge artefacts that would occur if the reconstruction was performed directly on a 256x256x40 grid (Zbijewski & Beekman 2004*a*).

Feldkamp reconstructions (Feldkamp et al. 1984) of the simulated full-scan projections were also obtained. A 256x256x40 grid was used and a Hamming filter was employed for noise apodisation (cut-off: 0.9 of the Nyquist frequency). For detector areas corresponding to the gaps, missing line integrals were filled in by linear interpolation. The interpolation was performed within each detector row separately.

As will be discussed later, it will most probably be necessary to combine much more sophisticated interpolation schemes with projection rebinning and the use of consistency conditions in order to achieve optimal performance of analytical methods for non-continuous projection data. No solution to this problem has so far been presented in the literature. The primary goal of this paper is however to assess the efficacy of SR for non-continuous projection data, not to make a detailed comparison of the two reconstruction methods. Feldkamp results presented here are meant to give the reader a feeling about the severity of gap-induced artifacts in the case when only the simplest protective measures are taken.

7.2.4 Assessment of artefact strength

Noisy reconstructions were inspected visually. Since error values computed directly from these reconstructions would include a contribution from image noise, quantitative assessment of artifact strength was performed using a set of reconstructions of noise-free projections. Mean Error was computed for each of the noiseless images:

$$\mathrm{ME} = \frac{1}{N}\sum_{k=1}^{N} |(\tilde{\mu}(k) - \mu(k))| \tag{7.1}$$

where $\mu(k)$ and $\tilde{\mu}(k)$ are the k–th pixel value in the phantom and in the reconstruction, respectively. ME was computed over a union of four image regions belonging to areas most severely polluted by gap-induced artefacts. These regions are shown as white squares in Fig. 7.1.

7.3 Results

Fig. 7.3 shows the results of Feldkamp reconstruction obtained for different configurations of detector gaps. The off-centre slices shown in the bottom row correspond to the outermost cross-section of the phantom, located 5.5 mm away from the centre. Disturbing artefacts are present in the images both for symmetric and asymmetric placement of detector discontinuities. In the latter case, the artefact strength is somewhat lower than in the symmetric setup. Of importance is also the apparent intensity drop present in the reconstructions of the outermost slice of the

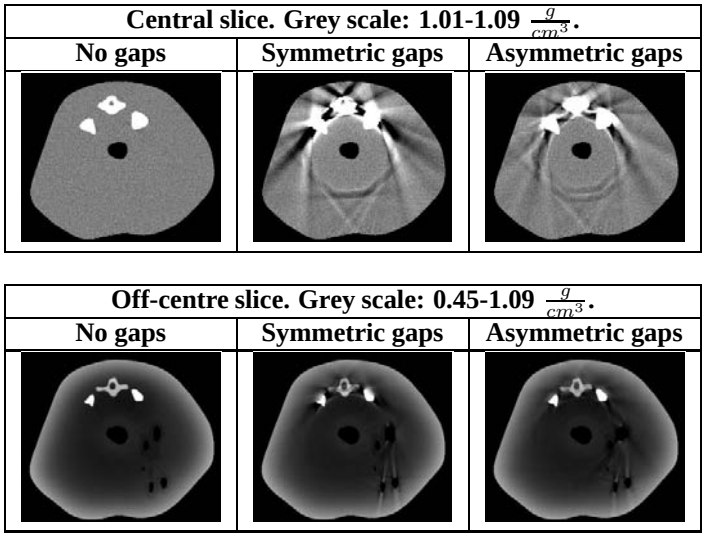

Figure 7.3: Feldkamp reconstructions of the phantom from Fig. 7.1 obtained for various gap configurations and a full scan range. The grey scale was selected to emphasise the artefacts. Gap-related artefacts are apparent for both symmetric and asymmetric gap placement. Note the change in grey scale required to display the results for the off-centre slice, where a significant intensity drop occurs as a result of cone-beam geometry.

volume. This artefact is caused by the incompleteness of the circular cone-beam geometry (Kak & Slaney 1988).

Fig. 7.4 shows the results of OSC reconstruction for the symmetric configuration of gaps and various angular acquisition ranges. Only the central slice of the volume is depicted. Even for

Central slice. Grey scale: 1.01-1.09 $\frac{g}{cm^3}$.			
	Short-scan. Angular range: $216°$	**Over-scan. Angular range:** $288°$	**Full-scan. Angular range:** $360°$
Symmetric gaps 50 iter.		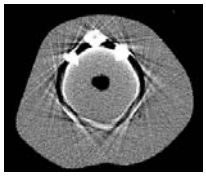	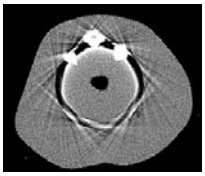

Figure 7.4: OSC reconstructions of projections with symmetrically located gaps. For every angular range tested, the incompleteness of projection data caused by gaps leads to significant artefacts in the images obtained.

the full scan, obvious gap-induced artefacts are visible in the reconstruction; their appearance did not change significantly for other angular ranges tested.

Fig. 7.5 shows central slices of OSC reconstructions obtained for the asymmetric placement of gaps. Fig. 7.6 depicts the outermost slices of the same reconstructions. When asymmetrical configuration of gaps is combined with a full-scan acquisition, statistical reconstruction results in images that are hard to distinguish from the reconstructions of continuous projections. The artefacts are removed almost completely both from the central slice and from the off-centre slices of the reconstructed volume. When the acquisition arc is reduced below the full scan, streak artefacts start to emerge even for the asymmetric configuration of detector gaps. The extent and the strength of these disturbances appears larger for the short-scan than for the over-scan. In both cases the magnitude of the gap-induced inaccuracies reduces with the number of iterations.

Finally, it should be noted that in volumes reconstructed with SR there is no obvious drop in intensity in the outermost slice. Such a drop is however present in Feldkamp results shown in Fig. 7.3.

In Fig. 7.7, the Mean Error of OSC reconstructions is plotted for different angular scanning ranges. In all cases the error attained for symmetric configuration of gaps is almost one order of magnitude larger than the error attained for the reconstruction of continuous projection data. Asymmetric placement of gaps reduces the artefacts to a level significantly lower than in the symmetric configuration. The closer one gets to a full-scan, the smaller the difference in mean error values between the asymmetric gap configuration and the gap-free detector. For the case of a full scan, the ME for the asymmetric setup follows very closely the ME obtained for the continuous detector. This artifact rejection can be observed both for the central and for the off-centre (outermost) slice of the reconstructed volume, as demonstrated in the bottom row of Fig. 7.7. With increasing iteration number, some decrease in the ME value can be observed for every configuration of gaps and every angular range tested, confirming the trend visible in

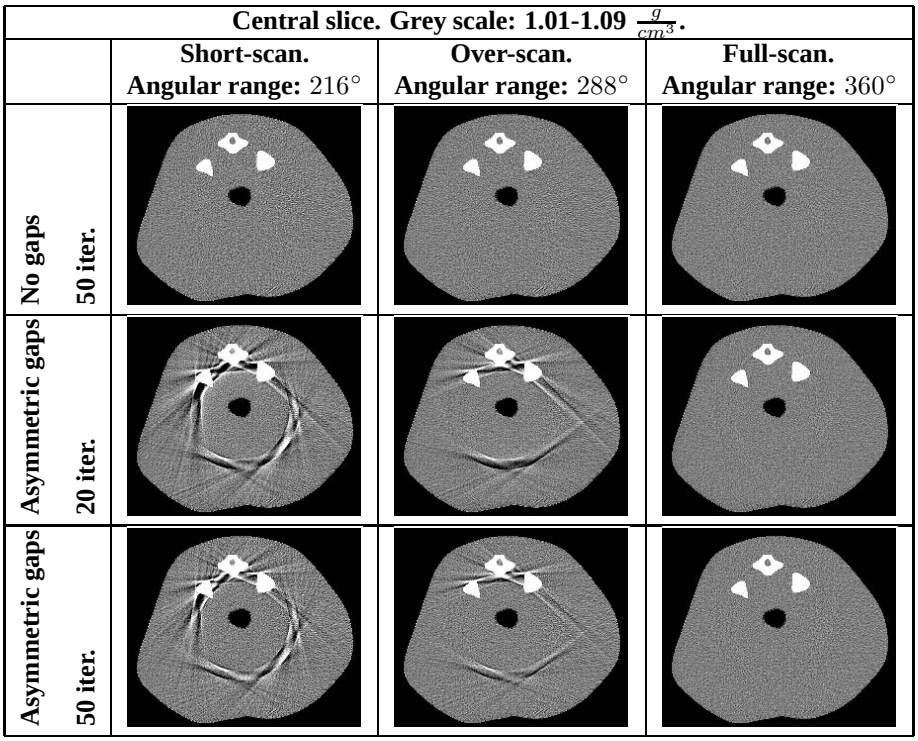

Figure 7.5: Reconstructions obtained with OSC for continuous projections and for asymmetric gaps configuration. Central slices are shown. When a full scan is executed in the asymmetric gaps configuration, the resulting OSC reconstruction is almost identical to the one obtained for continuous projection.

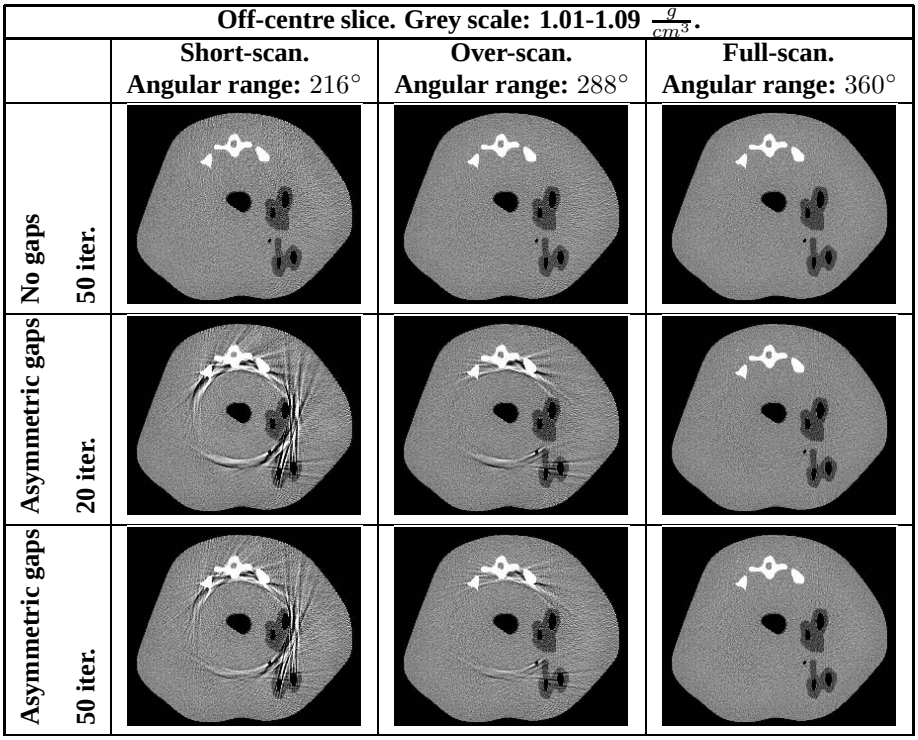

Figure 7.6: Like Fig. 7.5, but an off-centre slice (located 5.5 mm away from the centre) is shown. Despite the incompleteness of projection data inherent to cone-beam geometry, effective removal of gap-induced artefacts is achieved for a full scan and asymmetric placement of gaps. Note also the lack of any apparent cone-beam artefacts in the slices presented.

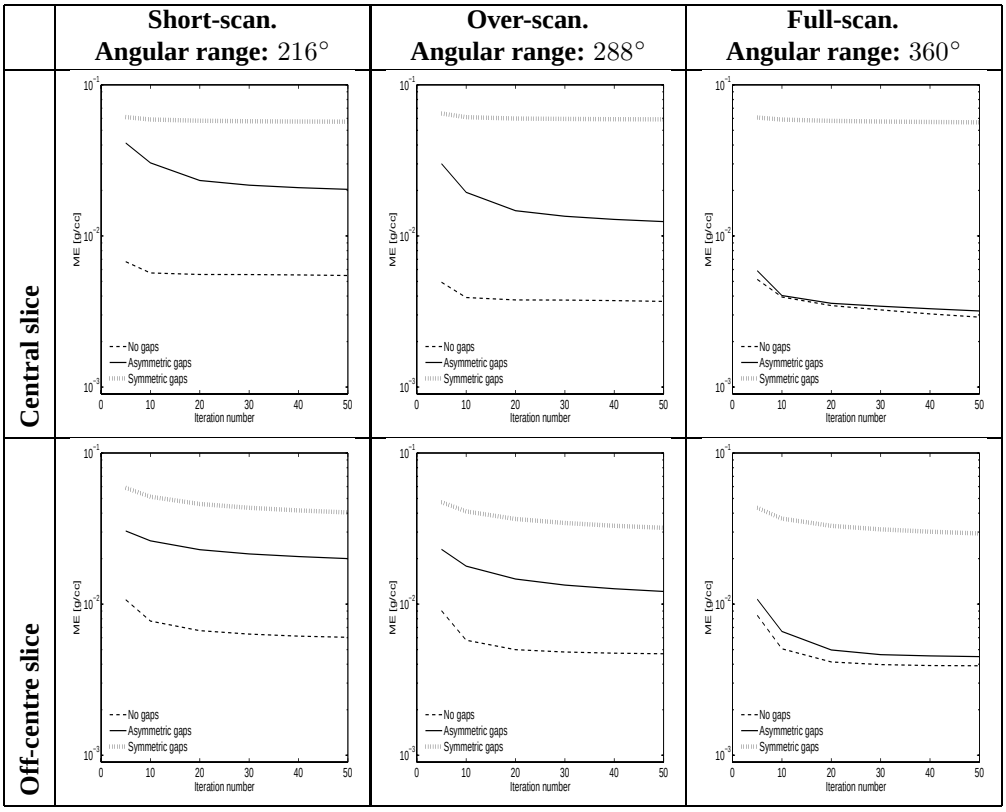

Figure 7.7: Mean Error of the reconstruction as a function of iteration number for OSC. For a full scan (rightmost panels in both rows), the ME curve for the asymmetric placement of gaps is close to the ME curve for continuous detector, indicating effective removal of gap-induced artefacts for this detector configuration. The artefacts are almost completely suppressed both in the central and in the off-centre slice. For scan ranges shorter than a full circle, full removal of reconstruction errors caused by the gaps cannot be achieved even for high iteration numbers. Nevertheless, the asymmetric configuration of gaps results in the ME being almost one order of magnitude lower than the symmetric configuration.

Fig. 7.5 and Fig. 7.6.

7.4 Discussion

Fig. 7.8 compares the symmetric and asymmetric gap configurations. The situation in the central

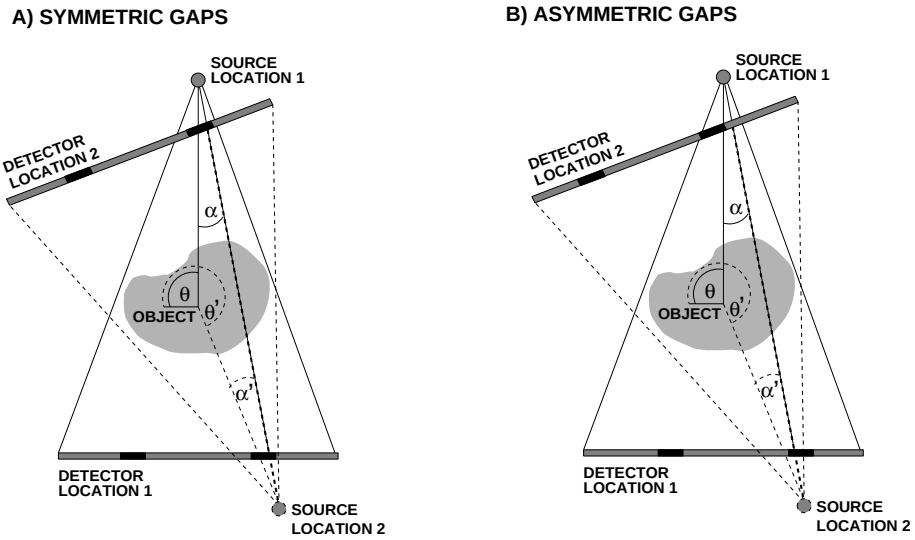

Figure 7.8: Comparison between symmetric and asymmetric placements of detector gaps. In the symmetric configuration (panel *a*), both rays from a conjugate pair are missing due to a gap. For the asymmetric configuration (panel *b*) and a full scan, even if a given ray is missing due to a gap (continuous line, source and detector location 1), its conjugate ray (dashed line, source and detector location 2) is still recorded.

imaging plane is depicted. The two overlapping rays drawn with continuous and dashed lines belong to a so-called *conjugate pair*. For a projection angle θ and a line integral recorded at a fan angle α, the detector location of its *conjugate (or complementary) ray* is given by:

$$\theta' = \theta - 2\alpha - 180^o \tag{7.2}$$

$$\alpha' = -\alpha \tag{7.3}$$

where θ' determines the projection containing the conjugate ray and α' is the fan angle of this ray (Kak & Slaney 1988). If the gaps are placed symmetrically with respect to the detector centre, both rays from a conjugate pair are missing for every integration line belonging to a detector gap. This results in an obviously incomplete projection dataset, regardless of the angular range of the acquisition. Even though statistical methods are usually more immune to data insufficiencies than analytical algorithms, in this case SR is directed away from the true, artefact-free solution towards an erroneous reconstruction containing a localised ring artefact.

In the other configuration analysed in this paper, the gaps were placed asymmetrically with respect to the detector centre in such a way that there was no overlap between the mirror image

of one gap and the other discontinuity. The case is illustrated in Fig. 7.8 *b*. For a full-scan acquisition, even if one ray is missing due to a gap, its conjugate ray is still present in the dataset. A complete set of projections is therefore collected in the central imaging plane. SR utilises this information correctly and produces reconstructions that have central slices free of any significant artefacts. Outside the central imaging plane, no rays conveying exactly the projection information missing due to a gap can be found in the dataset even in the case of the asymmetric gap configuration. This is because every conjugate pair of rays that traverses through a given image voxel contains integration lines differing in the cone angle (Tang et al. 2005). The gaps therefore cause an irrecoverable loss of projection data in the out-of-centre volume slices. Despite this, SR images obtained for the asymmetric gaps configuration and a full scan acquisition are practically free of any gap-related artefacts even in the out-of-centre slices. No significant disturbances have been observed for cone-beam angles up to approx. $2.6\,^{\circ}$. At this distance from the volume centre, severe cone-beam artefacts are present in Feldkamp reconstructions. This shows that once complete sampling has been achieved in the central imaging plane, SR can handle the combined effects of detector discontinuities and cone-beam geometry over a range of axial locations. If however complete sampling cannot be guaranteed in the central plane, the reconstructions of the whole volume will be polluted by gap-related artefacts.

The set of projections collected in the central imaging plane in the asymmetric gap configuration becomes incomplete as the angular range of the acquisition is reduced to less than a full scan. In this situation the conjugate projection lines for some of the gap detectors are no longer recorded. As a result, streak artefacts emerge in SR for the missing projection rays. Once the projection dataset collected in the central imaging plane becomes incomplete, similar artefact patterns start to appear in all image slices; no significant strengthening or spreading of the artefacts occurs for the out-of-centre axial locations.

The findings reported in this paper are expected to be applicable to the case of conventional CT systems with faulty or miscalibrated detector pixels. A statistical reconstruction algorithm can simply ignore the data from the faulty pixels and treat them as detector gaps. Even if an extended cluster of defective cells is present in a detector, the projection dataset may still be complete in the central imaging plane. SR will therefore be able to yield artefact-free images without any additional pre-processing of projections. The only required additional operation will be to locate the defective detector pixels.

Some observations can be made with regard to the use of the analytical methods in systems containing detector discontinuities. In this article, simple linear interpolation was used to fill the detector gaps. Results presented by other authors (Glover & Pelc 1981) suggest that no significant improvement can be achieved by going for higher order interpolation schemes. It is likely that the main problem here is that interpolation introduces inconsistencies into the the set of projection views. Such inconsistencies have a global influence on Feldkamp reconstruction and result in streak artefacts that extend over the whole field-of-view (Glover & Pelc 1981). Most probably interpolation alone is not sufficient to yield optimal Feldkamp performance. In the case of asymmetric configuration of gaps, the projection data in the central imaging plane could be re-binned into a complete 180° parallel beam set and then reconstructed analytically. The resulting images would be free of any gap-related artefacts. However, as mentioned above, outside the central imaging plane the projection rays impinging on the detector discontinuities are irrecoverably missing from the dataset. Much more sophisticated projection completion

schemes would then have to be used in order to produce an artefact-free analytical reconstruction. With SR, no pre-processing was necessary to arrive at a reconstruction that appears free of errors caused by the presence of detector gaps.

A consistency condition, similar to the one proposed in Chen & Leng (2005), but extended to three dimensions, could also be utilised instead of simple interpolation to fill in the projection gaps. It should be noted, however, that even for a single gap covering about 5% of the detector area and for a 360° scan some artefacts were still visible in the images reconstructed using this consistency condition (Chen & Leng 2005). Since a configuration with a single gap and a full scan provides a complete projection set, our results indicate that in this case SR with no gap filling would result in artefact-free images.

Another solution that may potentially be helpful in reducing gap-induced artifacts in analytically reconstructed images is to preceed the reconstruction with penalised-likelihood smoothing of the sinogram (Rivière & Pan 2000, Rivière 2005). Such a sinogram smoothing seeks a set of line integrals maximising the likelihood of obtaining the measured intensity values; the maximisation is performed based on some model of noise in the projections. So far, this approach was successfully used to reduce noise-induced artifacts in low-dose CT data. It may be possible to extend the smoothing to incorporate modelling of projection discontinuities, so that the gaps would be filled in a smooth way and the gap-induced streaks in the reconstructions would be minimised.

Algorithms developed for recovery of missing areas in images and video frames can also be used to fill the detector gaps prior to analytical reconstruction. Recently proposed methods, such as the adaptive sparse reconstruction technique (Guleryuz 2006*a*, Guleryuz 2006*b*) result in robust estimates of image data even for cases when the missing areas are relatively large and contain complicated transitions. It remains to be seen whether by filling the projection discontinuities with such signal-processing techniques one will be able to significantly reduce gap-induced artifacts in analytically reconstructed images.

7.5 Conclusions

Statistical reconstruction has been shown to render images almost free of gap-induced artefacts in systems with discontinuities covering as much as 10% of detector area. No sophisticated interpolation, rebinning or projection completion schemes were necessary. The only condition which must be fulfilled is that the configuration of gaps and the scanning protocol guarantee complete object sampling in the central imaging plane. For the configuration studied in our simulation, fulfilment of this requirement was sufficient to obtain practically artefact-free reconstruction also for off-centre image slices, where the projection dataset was no longer complete. Images free of any noticeable gap-induced or cone-beam artefacts have been achieved even at axial locations where significant cone-beam artefacts were visible in Feldkamp reconstructions.

SR not only allows for the removal of gap-related artefacts without any pre-processing of projection data, it also provides great flexibility with respect to the system geometry, allowing for arbitrary placement of detector segments. Both these properties make SR the best currently available potential candidate for use in X-ray CT systems based on modular detector configurations.

The robustness of statistical reconstruction to projection discontinuities may be useful in

dealing with miscalibrated or faulty detector pixels in conventional transmission CT systems. Our results indicate that in this case too, significant reduction of artefacts can be achieved with SR without the need for pre-processing of projections (except for the detection of defective detector pixels) or post-processing of reconstructed images.

Acknowledgments

We thank dr. M. Rentmeester for fruitful technical discussions and B. Vastenhouw for ongoing computer support.

Summary

Recent years brought about a significant renewal of interest in the application of iterative reconstruction methods to X-ray computed tomography. Papers presented at recent conferences on image reconstruction show that almost all main manufacturers of CT equipment are nowadays involved in the development and validation of iterative X-ray CT reconstruction algorithms. One obvious reason behind this trend is the ongoing, tremendous increase in the processing power of modern computers. Despite relatively large computational demands of iterative algorithms, the speed of currently available computational electronics makes their clinical use more and more feasible. Another important factor spurring the research on iterative X-ray CT reconstruction is a growing realisation that improvements in scanner hardware alone may not be enough to allow a competitive edge in terms of achievable image quality. Out of many available iterative algorithms, statistical methods seem to be the most attractive. Since such algorithms allow for improved modelling of system geometry and photon transport, they may be tailored to reduce image artefacts caused by various physical factors. Moreover, statistical reconstruction (SR) methods take into account the characteristics of noise in projection data. They may therefore facilitate a reduction of radiation exposure during a CT scan. This potential benefit of using SR in X-ray tomography cannot be underestimated, as CT is inherently a high-dose technique: it accounts for only 4-10% of the total number of X-ray examinations performed in the western world, but is responsible for 40-50% of the total cumulative dose delivered during such examinations (Shrimpton & Edyvean 1998, Hidajat et al. 2001, Lewis 2005).

Since X-ray CT is a relatively new application field for statistical reconstruction methods, there is still a need for in-depth research on this subject. The thesis contributes to this effort by tackling a variety of issues related to system modelling in SR. The first chapters deal with fundamental aspects of modelling: object discretisation and algorithm initialisation. In **Chapter 2** we show that artefacts may emerge in reconstructions if overly coarse image grids are used. Only by reconstructing on a finer grid than would be used in an analytical algorithm can one retain the main advantage of SR over analytical methods: the improved resolution-noise trade-off. **Chapter 3** demonstrates that the emergence of artefacts is more related to the density of object discretisation than to the selection of image basis function: for coarse grids, artefacts emerge both for voxel- and blob-based image representations. Another important finding of this thesis, reported in **Chapter 4**, is that the use of an analytically reconstructed image as initial guess for SR may result in significant acceleration of SR's convergence around small, high-contrast structures. Speed-ups of up to one order of magnitude are achievable. Most importantly, the noise injected with this initial estimate is promptly removed by SR, so the acceleration is

obtained without any penalty in terms of resolution-noise trade-off.

The second part of the thesis deals with potential benefits achievable by introducing detailed system models into the iterative reconstruction process. **Chapters 5 and 6** introduce an efficient and accurate Monte Carlo-based scatter correction scheme. As cone-beam imaging geometries and high-resolution detectors are becoming commonplace in clinical imaging, the issue of scatter reduction grows in importance. The research on scatter modelling and correction presented in this thesis has been focused on micro-CT systems. We have developed and validated a dedicated Monte Carlo simulator of X-ray CT scanners. The results of its validation are presented in **Chapter 6**. With the simulator, the scale of scatter contamination of micro-CT projections has been investigated. It has been found that scatter is responsible for as much as 50% of the strength of cupping artefacts present in the reconstructions of rat-sized objects. The proposed MC simulator uses an advanced fitting scheme to significantly reduce the computational time needed to obtain an accurate estimate of object scatter. Acceleration factors of three to four orders of magnitude are attainable. Such a rapid scatter simulation is no longer a computational bottleneck during image reconstruction. In **Chapter 6** we show how it can be combined with a poly-energetic statistical reconstruction algorithm in order to yield micro-CT images free of any scatter and beam hardening artefacts. Strong reduction of artefacts is demonstrated both for real and simulated micro-CT data.

Finally, **Chapter 7** shows how SR can benefit the design of novel CT systems. We investigate a micro-CT configuration based on modular detectors, where many fast, high-resolution but small field-of-view X-ray cameras are combined to form a single large area detector. In such a design, appearance of gaps between the modules seems inevitable. We show that by using SR one may obtain volumetric reconstructions free of any gap-induced artefacts even for systems where discontinuities cover as much as 10% of the detector area. It has, however, to be ascertained that the projection data collected with the modular detector is complete in the central imaging plane. The main advantage over analytical methods is that no projection pre-processing is necessary in SR. In contrast, for analytical methods advanced projection completion schemes would be needed. Simple *ad hoc* solutions such as interpolation inside the gaps would lead to strong artefacts in analytically reconstructed images. The findings of Chapter 7 may also find use in dealing with malfunctioning detector cells in conventional CT systems.

Samenvatting

De afgelopen jaren is er een grote hernieuwde belangstelling ontstaan voor het toepassen van iteratieve reconstructie methoden in Röntgen computed tomografie (CT). Materiaal dat gepresenteerd is op recente conferenties over beeldreconstructie laat zien dat alle grote fabrikanten van CT systemen momenteel betrokken zijn bij de ontwikkeling en validatie van iteratieve Röntgen CT reconstructie algoritmen. Eén duidelijk oorzaak voor deze trend is de niet aflatende groei van het rekenvermogen van computers. Ondanks de relatief grote eisen die iterative reconstructie methoden aan de rekenkracht van computers stellen is de snelheid van moderne computers dusdanig dat het gebruik van iteratieve methoden in klinische systemen steeds realistischer wordt. Een andere belangrijke factor die het onderzoek naar iteratieve Röntgen CT reconstructie aanspoort is de groeiende gewaarwording dat verbetering in scanner apparatuur alleen niet voldoende is om wezenlijke verbetering in de beeldkwaliteit tot stand te brengen. Van de vele iteratieve reconstructie algoritmen is statistische reconstructie (SR) de meest aantrekkelijke. Daar deze algoritmen een verbeterde modellering van fotontransport en van de geometrie van het systeem toestaan kunnen ze op maat aangepast worden om beeldartefacten te reduceren die veroorzaakt zijn door verschillende fysische factoren. Bovendien kunnen met statistische reconstructie methoden de eigenschappen van ruis in projectiedata meegenomen worden. Dit zou kunnen leiden tot een vermindering van de blootstelling aan straling tijdens CT scans. Dit mogelijke voordeel van het gebruik van SR in Röntgen tomografie mag niet onderschat worden: CT is inherent een techniek met hoge stralings doses. Hoewel CT slechts 4–10 % van de totale hoeveelheid Röntgen onderzoeken in de westerse wereld behelst is CT verantwoordelijk voor 40–50 % van de cumulatieve stralings dosis tijdens dergelijke onderzoeken (Shrimpton & Edyvean 1998, Hidajat *et al.* 2001, Lewis 2005).

Daar Röntgen CT een relatief nieuw toepassingsveld is voor statistische reconstructie (SR) methoden is er nog steeds een behoefte aan verder diepgaand onderzoek. Dit proefschrift draagt hieraan bij door een aantal onderwerpen aan te snijden die betrekking hebben op de systeem modellering in SR. In de eerste drie hoofdstukken worden twee fundamentele aspecten van de modellering behandeld: object discretisatie en de initialisatie van algoritmen. In hoofdstuk 1 laten we zien dat artefacten kunnen ontstaan tijdens reconstructies als te grove roosters worden gebruikt. Alleen als de reconstructies worden gedaan op een fijner rooster dan gebruikt zou worden voor analytische algoritmen kan het belangrijkste voordeel van SR op analytische algoritmen behouden blijven: de verbeterde resolutie–ruis verhouding. Hoofdstuk 2 laat zien dat de verschijning van artefacten meer gerelateerd is aan de dichtheid van de object discretisatie dan aan de keuze van de basis functies van het beeld: bij het gebruik van grovere roosters verschijnen

artefacten in zowel voxel als blob gebaseerde beeld representaties. Een ander belangrijk resultaat in dit proefschrift, in hoofdstuk 3, is dat het gebruik van een analytisch gereconstrueerd beeld als start oplossing voor statistische reconstructie kan resulteren in een significante versnelling van de SR convergentie van het beeld in de buurt van kleine structuren met hoog contrast. Versnellingen tot op één grootteorde zijn bereikbaar. Belangrijker echter is dat de ruis die toegevoegd wordt aan de keuze van de start oplossing door SR efficient verwijderd wordt zodat de versnelling verkregen wordt zonder nadelige gevolgen voor de resolutie-ruis verhouding.

Het tweede deel van het proefschrift behandelt de mogelijke voordelen die verkregen kunnen worden door gedetailleerde systeem modellen in te voeren in het iteratieve beeld reconstructie proces. In de hoofdstukken 5 en 6 introduceren we een efficient en accuraat verstrooiingscorrectie schema gebaseerd op Monte Carlo (MC). Naarmate cone-beam opstellingen en hoge-resolutie detectoren meer gewoon worden in klinische beeldverwerking zullen verstrooiings correcties zeker een grotere rol gaan spelen. Het onderzoek naar het modelleren en corrigeren van verstrooiing, zoals in dit proefschrift beschreven, richtte zich op micro-CT systemen. We hebben speciaal voor dit doel een Monte Carlo simulator voor Röntgen CT systemen ontwikkeld en gevalideerd. De resulaten van de validatie staan beschreven in hoofdstuk 6. Met de simulator is de schaal van verstrooiings contaminatie van micro-CT projecties onderzocht. We vonden dat verstrooiing verantwoordelijk is voor tot 50% van de sterkte van cupping artefacten zoals die ontstaan in de reconstructie van objecten ter grootte van een rat. De voorgestelde MC simulator gebruikt een geavanceerd fit schema die de rekentijd die benodigd is voor het maken van een accurate schatting van verstrooiing significant verkort. Versnellingen van 3 à 4 grootte ordes liggen binnen bereik. Zo'n snelle verstrooiings simulatie is geen computationele horde meer voor beeldreconstructie. In hoofdstuk 6 demonstreren we hoe het gecombineerd kan worden met poly-energetische statistische reconstructie algorithmen om micro-CT beelden te verkrijgen zonder verstrooiings- of beam-hardening artefacten. We laten een sterke reductie van artefacten zien in zowel reele als gesimuleerde micro-CT data.

Tenslotte laten we in hoofdstuk 7 zien hoe SR nuttig kan zijn bij het ontwerpen van nieuwe CT systemen. We bestuderen een micro-CT configuratie gebaseerd op modulaire detectoren waar vele snelle hoge-resolutie Röntgen camera's met een klein field-of-view gecombineerd worden teneinde samen één grote detector te vormen. In dergelijke ontwerpen zijn uitsparingen tussen de modules onvermijdelijk. We laten zien dat met SR volumetrische reconstructies gedaan kunnen worden zonder beeld artefacten die ontstaan door de aanwezigheid van uitsparingen, zelfs voor systemen waar de discontinuiteiten tot 10% van het detector oppervlak beslaan. Men moet er zich dan echter wel van verzekeren dat de projectie data die verkregen is met de modulaire detector in het central imaging plane volledig is. Het belangrijkste voordeel boven analytische methoden is dat geen projectie pre-processing nodig is in SR. Voor analytische reconstructie methoden daarentegen zouden geavanceerde projectie aanvullingsschema's nodig zijn; eenvoudige ad-hoc oplossingen zoals interpolatie binnen de uitsparingen zou leiden tot sterke artefacten in analytisch gereconstueerde beelden. De resultaten uit hoofdstuk 7 kunnen ook gebruikt worden als in conventionele CT systemen uitsparingen ontstaan doordat, bijvoorbeeld, detector cellen niet werken.

Bibliography

Andersen, A. H. & Kak, A. C. (1984), 'Simultaneous algebraic reconstruction technique (SART): A superior implementation of the ART algorithm', *Ultrason. Imaging* **6**, 81–94.

Beekman, F. J., de Jong, H. W. A. M. & Slijpen, E. T. P. (1999), 'Efficient SPECT scatter response estimation in non-uniform media using correlated Monte Carlo simulations', *Phys.Med.Biol.* **44**, N183–N192.

Beekman, F. J., de Jong, H. W. A. M. & van Geloven, S. (2002), 'Efficient fully 3D iterative SPECT reconstruction with Monte Carlo based scatter compensation', *IEEE Trans. Med. Im.* **21**, 867–877.

Beekman, F. J. & de Vree, G. A. (2005), 'Photon-counting versus an integrating CCD-based gamma-camera: important consequences for spatial resolution', *Phys. Med. Biol.* **50**, N109–N119.

Beekman, F. J. & Kamphuis, C. (2001), 'Ordered subset reconstruction for X-ray CT reconstruction', *Phys. Med. Biol.* **46**, 1835–1844.

Beekman, F. J., Kamphuis, C., Hutton, B. F. & van Rijk, P. P. (1998), 'Half-fan-beam collimators combined with scanning point sources for simultaneous emission transmission imaging', *J. Nucl. Med.* **39**, 1996–2003.

Berger, M., Hubbell, J., Seltzer, S., Coursey, J. & Zucker, D. (1999), XCOM: Photon cross sections database, Technical report, National Institute of Standards and Technology.
URL: *http://physics.nist.gov/PhysRefData/Xcom/Text/XCOM.html*

Bertram, M., Wiegert, J. & Rose, G. (2005), 'Potential of software-based scatter corrections in cone-beam volume CT', *Proceedings of SPIE* **5745**, 259–270.

Black, N. & Gregor, J. (2005), 'Monte Carlo simulation of scatter in a cone-beam micro-CT scanner', *Proceedings of the 8th International Meeting on Fully Three-Dimensional Image Reconstruction in Radiology and Nuclear Medicine* pp. 207–210.

Boone, J. & Seibert, J. (1988), 'Monte Carlo simulation of the scattered radiation distribution in diagnostic radiology', *Med. Phys.* **15**(5), 713–720.

Boone, J. & Seibert, J. (1998), 'An analytical model of the scattered radiation distribution in diagnostic radiology', *Med. Phys.* **15**(5), 721–725.

Bowsher, J. E., Tornai, M. P., Peter, J., Gonzales-Trotter, D. E., Krol, A., Gilland, D. R. & Jaszczak, R. J. (2002), 'Modeling the axial extension of a transmission line source within iterative reconstruction via multiple transmission sources', *IEEE Trans. Med. Im.* **21**, 200–215.

Chan, H. & Doi, K. (1983), 'The validity of Monte Carlo simulations in studies of scattered radiation in daignostic radiology', *Phys.Med.Biol.* **28**(2), 109–129.

Chen, G.-H. & Leng, S. (2005), 'A new data consistency condition for fan-beam projection data', *Medical Physics* **32**(4), 961–967.

Colijn, A. P. & Beekman, F. J. (2004), 'Accelerated simulation of cone beam X-ray scatter projections', *IEEE Trans.Med.Im.* **23**(5), 584–590.

Colijn, A. P., Zbijewski, W., Sasov, A. & Beekman, F. J. (2004), 'Experimental validation of a rapid Monte Carlo based Micro-CT simulator', *Phys.Med.Biol.* **49**(18), 4321–4333.

Crawford, C. R. & King, K. F. (1990), 'Computed tomography scanning with simultaneous patient translation', *Med. Phys.* **17**(6), 967–982.

de Jong, H. W. A. M., Boellaard, R., Knoess, C., Lenox, M., Michel, C., Casey, M. & Lammertsma, A. A. (2003), 'Correction methods for missing data in sinograms of the HRRT PET scanner', *IEEE Trans. Nucl. Sci.* **50**(5), 1452–1456.

de Vree, G. A., Westra, A. H., Moody, I., van der Have, F., Ligtvoet, C. M. & Beekman, F. J. (2005), 'Photon-counting gamma camera based on an electron-multiplying CCD', *IEEE Trans. Nucl. Sci.* **52**(3), 580 – 588.

Elbakri, I. A. (2003), Statistical reconstruction algorithms for polyenergetic X-ray computed tomography, PhD thesis, University of Michigan.

Elbakri, I. A. & Fessler, J. A. (2002), 'Statistical image reconstruction for polyenergetic X–ray computed tomography', *IEEE Trans. Med. Im.* **21**(2), 89–99.

Elbakri, I. A. & Fessler, J. A. (2003), 'Segmentation-free statistical image reconstruction for polyenergetic X–ray computed tomography with experimental validation', *Phys. Med. Biol.* **48**, 2453–2477.

Endo, M., Tsunoo, T., Nakamori, N. & Yoshida, K. (2001), 'Effect of scattered radiation on image noise in cone beam CT', *Med. Phys.* **28**(4), 469–474.

Erdoğan, H. & Fessler, J. A. (1999), 'Ordered subsets algorithms for transmission tomography', *Phys. Med. Biol.* **44**, 2835–2851.

Feldkamp, L. A., Davis, L. C. & Kress, J. W. (1984), 'Practical cone-beam algorithm', *J.Opt.Soc.Am.* **A1**, 612–619.

Fessler, J. A. (2001), *SPIE Handbook of Medical Imaging*, SPIE Press, Bellingham, Washington USA, chapter Statistical Image Reconstruction Methods for Transmission Tomography, pp. 207–219.

Gilland, D. R., Jaszczak, R. J. & Coleman, R. E. (2000), 'Transmission CT reconstruction for offset fan beam collimation', *IEEE Trans. Nucl. Sci.* **47**, 1602–1606.

Gilland, D. R., Wang, H., Coleman, R. E. & Jaszczak, R. J. (1997), 'Long focal length, asymmetric fan beam collimation for transmission acquisition with a triple camera SPECT system', *IEEE Trans.Nucl.Sci.* **44**, 1191–1196.

Glover, G. H. (1982), 'Compton scatter effects in CT reconstructions', *Med, Phys.* **9**(6), 860–867.

Glover, G. H. & Pelc, N. J. (1981), 'An algorithm for the reduction of metal clip artifacts in CT reconstructions', *Medical Physics* **8**(6), 800–807.

Goertzen, A., Beekman, F. J. & Cherry, S. R. (2002), 'Effect of phantom voxelization in CT simulation', *Medical Physics* **29**(4), 492–498.

Goertzen, A., Nagarkar, V., Street, R. A., Paulus, M. J., Boone, J. M. & Cherry, S. R. (2004), 'A comparison of x-ray detectors for mouse CT imaging', *Phys. Med. Biol.* **49**, 5251–5265.

Gordon, R., Bender, R. & Herman, G. T. (1970), 'Algbraic reconstruction techniques (ART) for three-dimensional electron microscopy and X-ray photography', *J.Theor.Biol.* **29**, 471–481.

Guan, H. & Gordon, R. (1996), 'Computed tomography using algebraic reconstruction techniques (ARTs) with different projection access schemes: a comparison study under practical situations.', *Phys. Med. Biol.* **41**, 1727–1743.

Guleryuz, O. G. (2006*a*), 'Nonlinear approximation based image recovery using adaptive sparse reconstructions and iterated denoising–part I: Theory', *IEEE Trans. Im. Proc.* **15**(3), 539–554.

Guleryuz, O. G. (2006*b*), 'Nonlinear approximation based image recovery using adaptive sparse reconstructions and iterated denoising–part II: Adaptive algorithms', *IEEE Trans. Im. Proc.* **15**(3), 555–571.

Herman, G. T. (1980), *Image Reconstruction from Projections*, Academic Press, New York.

Hidajat, N., Wolf, M., Nunnemann, A., Liersch, P., Gebauer, B., Teichgraber, U., Schroder, R. & Felix, R. (2001), 'Survey of conventional and spiral CT doses', *Radiology* **218**, 395–401.

Honda, M., Kikuchi, K. & Komatsu, K. (1991), 'Method for estimating the intensity of scattered radiation using a scatter generation model', *Med. Phys.* **18**(2), 219–226.

Hsieh, J. (1998), 'Adaptive streak artifact reduction in computed tomography resulting from excessive X-ray photon noise', *Medical Physics* **25**(11), 2134–2147.

Hsieh, J. (2003), *Computed Tomography. Principles, Design, Artifacts and Recent Advances*, SPIE Press, Bellingham, Washington USA.

Hsieh, J., Chao, E., Thibault, J.-B., Grekowicz, B., Horst, A., McOlash, S. & Myers, T. J. (2004), 'A novel reconstruction algorithm to extend the CT scan field-of-view', *Medical Physics* **31**(9), 2385–2391.

Hu, H. (1999), 'Multi-slice helical CT: Scan and reconstruction', *Med. Phys.* **26**(1), 5–18.

Hubbell, J. & Overbo, I. (1979), 'Relativistic atomic form factors and photon coherent scattering cross sections', *J. Phys. Ref. Data* **9**, 69–106.

Hudson, H. M., Hutton, B. F. & Larkin, R. (1991), 'Accelerated EM reconstruction using ordered subsets', *J.Nucl.Med.* **33**, 960.

Hudson, H. M. & Larkin, R. S. (1994), 'Accelerated image reconstruction using ordered subsets of projection data', *IEEE Trans.Med.Im.* **13**, 601–609.

Hynecek, J. (2001), 'Impactron - a new solid state image intensifier', *IEEE Trans. on Electron. Devices* **48**(10), 2238–2241.

Jerram, P., Pool, P. J., Bell, R., Burt, D. J., Bowring, S., Spencer, S., Hazelwood, M., Moody, I., Catlett, N. & Heyes, P. S. (2001), 'The LLLCCD: Low light imaging without the need for an intensifier', *Proc. SPIE* **4306**, 178–186.

John, F. (1938), 'The ultrahyperbolic equation with 4 independent variables', *Duke Math J.* **4**, 300–322.

Johns, P. & Yaffe, M. (1982), 'Scattered radiation in fan beam imaging systems', *Med. Phys.* **9**(2), 231–239.

Joseph, P. & Spital, R. (1982), 'The effects of scatter in X-ray computed tomography', *Med. Phys.* **9**(4), 464–472.

Joseph, T. M. (1987), 'An improved algorithm for reprojecting rays through pixel images', *IEEE Trans. Med. Im.* **MI-1**, 192–201.

Kak, A. C. & Slaney, M. (1988), *Priciples of Computerized Tomographic Imaging*, IEEE Press, Piscataway.

Kalender, W. (1981), 'Monte Carlo calculations of X-ray scatter data for diagnostic radiology', *Phys. Med. Biol.* **Vol.26**(5), 835–849.

Kalender, W. A. (2000), *Computed tomography*, Publicis MCD Verlag, Erlangen and Muenchen, Germany.

Kalender, W. A., Seissler, W., Klotz, E. & Vock, P. (1990), 'Spiral volumetric CT with single-breathhold technique, continuous transport, and continuous scanner rotation', *Radiology* **176**(1), 181–183.

Kalos, M. (1963), 'On the estimation of flux at a point', *Nucl. Sci. Eng.* **16**(6), 111–117.

Kamphuis, C. & Beekman, F. J. (1998*a*), 'Accelerated iterative transmission CT reconstruction using an ordered subset convex algorithm', *IEEE Trans.Med.Im.* **17**, 1101–1105.

Kamphuis, C. & Beekman, F. J. (1998*b*), 'A feasibility study of offset cone-beam collimators for combined emission transmission brain SPECT on a dual-head system', *IEEE Trans.Nucl.Sci.* **45**, 1250–1254.

Kamphuis, C., Beekman, F. J., Viergever, M. A. & van Rijk, P. P. (1998), 'Dual matrix ordered subset reconstruction for accelerated 3D scatter correction in SPECT', *Eur. J. Nucl. Med.* **25**, 8–18.

Kanamori, H., Nakamori, N., Inoue, K. & Takenaka, E. (1985), 'Effects of scattered X-rays on CT images', *Phys. Med. Biol.* **30**(3), 239–249.

Karg, J., Niederloehner, D., Giersch, J. & Anton, G. (2005), 'Using the Medipix2 detector for energy weighting', *Nuclear Instruments and Methods in Physics Research A* **546**, 306–311.

Katsevich, A. (2002), 'Analysis of an exact inversion algorithm for spiral cone-beam CT', *Phys. Med. Biol.* **47**, 2583–2598.

Kawrakow, I. (2000), 'Accurate condensed history Monte Carlo simulation of electron transport. I. EGSnrc, the new EGS4 version', *Med. Phys.* **27**, 485–498.

Kole, S. & Beekman, F. J. (2005*a*), 'Evaluation of the ordered subset convex algorithm for cone-beam X-ray CT', *Phys. Med. Biol.* **50**(4), 613–625.

Kole, S. & Beekman, F. J. (2005*b*), 'Parallel statistical image reconstruction for cone-beam X-ray CT on a shared memory computation platform', *Phys. Med. Biol.* **50**(6), 1265–1272.

Kole, S. & Beekman, F. J. (2006), 'Evaluation of accelerated iterative X-ray CT image reconstruction using floating point graphics hardware', *Phys. Med. Biol.* **51**(4), 875–889.

Kudo, H. & Saito, T. (1991), 'Sinogram recovery with the method of convex projections for limited-data reconstruction in computed tomography', *J.Opt.Soc.Am. A* **8**(7), 1148–1160.

Kunze, H., Stierstorfer, K. & Haerer, W. (2005), 'Pre-processing of projections for iterative reconstruction', *Proceedings of the 8th International Meeting on Fully Three-Dimensional Image Reconstruction in Radiology and Nuclear Medicine* pp. 84–87.

Lange, K. (1990), 'Convergence of EM image reconstruction algorithms with Gibbs smoothing', *IEEE Trans.Med.Im* **9**(4), 439–446.

Lange, K. & Carson, R. (1984), 'E.M. reconstruction algorithms for emission and transmission tomography', *J.Comput.Assist.Tomog.* **8**, 306–316.

Leahy, R. M. & Byrne, C. L. (2000), 'Recent developments in iterative image reconstruction in PET and SPECT', *IEEE Trans. Med. Im.* **19**, 257–260.

Leliveld, C., Maas, J., Bom, V. & van Eijk, C. (1996), 'Monte Carlo modeling of coherent scattering: influence of interference', *IEEE Trans. Nucl. Science* **43**(6), 3315–3321.

Lewis, M. (2005), 'Principles of CT dosimetry', *Presentation from ImPACT course* .
URL: *http://www.impactscan.org/slides/impactcourse/principles of ct dosimetry/index.html*

Lewitt, R. M. (1990), 'Multidimensional image representations using generalized Kaiser-Bessel window functions', *J. Opt.Soc. Amer. A* **7**(10), 1834–1846.

Li, J., Jaszczak, R. J., Greer, K. L. & Coleman, R. E. (1994), 'Implementation of an accelerated iterative algorithm for cone beam SPECT', *Phys.Med.Biol.* **39**, 643–653.

Llopart, X., Campbell, M., Dinapoli, R., Segundo, D. S. & Pemigotti, E. (2002), 'Medipix2: a 64-k pixel readout chip with 55-μm square elements working in single photon counting mode', *IEEE Trans. Nucl. Sci.* **49**(5), 2279–2283.

Love, L. A. & Kruger, R. A. (1987), 'Scatter estimation for a digital radiographic system using convolution filtering', *Medical Physics* **14**(2), 178–185.

Lucy, L. B. (1974), 'An iterative technique for the rectification of observed distributions', *Astron. J.* **79**, 745–754.

Manglos, S. H. (1992), 'Truncation artifact suppression in cone-beam radionuclide transmission CT using maximum likelihood techniques: evaluation with human subjects.', *Phys. Med. Biol.* **37**, 549–562.

Manglos, S. H., Bassano, D. A., Thomas, F. D. & Grossman, Z. D. (1992), 'Imaging of the human torso using cone-beam transmission CT implemented on a rotating gamma camera', *J. Nucl. Med.* **33**, 150–156.

Manglos, S. H., Gagne, G. M., Thomas, F. D. & Narayanaswamy, R. (1995), 'Transmission maximum-likelihood reconstruction with ordered subsets for cone beam CT', *Phys. Med. Biol.* **40**, 1225–1241.

Matej, S. & Lewitt, R. M. (1996), 'Practical considerations for 3-D image reconstruction using spherically symmetric volume elements', *IEEE Trans.Med.Im.* **15**(1), 68–78.

De Man, B. & Basu, S. (2004), 'Distance-driven projection and backprojection in three dimensions', *Phys. Med. Biol.* **49**, 2463–2475.

De Man, B., Nuyts, J., Dupont, P., Marchal, G. & Suetens, P. (2000), 'Reduction of metal streak artefacts in X-ray computed tomography using a transmission maximum *a posteriori* algorithm', *IEEE Trans. Nucl. Sci* **47**, 977–981.

De Man, B., Nuyts, J., Dupont, P., Marchal, G. & Suetens, P. (2001), 'An iterative maximum–likelihood polychromatic algorithm for CT', *IEEE Trans. Med. Im.* **20**(10), 999–1008.

Medipix2 Collaboration (2005), Technical report.
URL: *http://medipix.web.cern.ch/MEDIPIX/*

Michel, C., Noo, F., Sibomana, M. & Faul, D. (2005), 'An iterative method for creating attenuation maps from highly truncated CT data', *Proceedings of the 8th International Meeting on Fully Three-Dimensional Image Reconstruction in Radiology and Nuclear Medicine* pp. 88–92.

Mueller, K. & Yagel, R. (1998), 'Rapid 3D cone-beam reconstruction with the Algebraic Reconstruction Technique (ART) by utilizing texture mapping graphics hardware', *Conference Record of the 1997 IEEE Nuclear Science Symposium and Medical Imaging Conference, Toronto* pp. 1552–1559.

Mueller, K. & Yagel, R. (2000), 'Rapid 3–D cone beam reconstruction with the simultaneous algebraic reconstruction technique SART using 2–D texture mapping hardware', *IEEE Trans. Med. Im.* **19**(12), 1227–1236.

Mueller, K., Yagel, R. & Wheeler, J. J. (1999*a*), 'Anti-aliased three–dimensional cone–beam reconstruction of low–contrast objects with algebraic methods', *IEEE Trans. Med. Im.* **18**(6), 519–537.

Mueller, K., Yagel, R. & Wheeler, J. J. (1999*b*), 'Fast implementation of algebraic methods for three–dimensional reconstruction for cone–beam data', *IEEE Trans. Med. Im.* **18**(6), 538–547.

Nagarkar, V. V., Gordon, J. S., Vasile, S., Gothoskar, P. & Hopkins, F. (1996), 'High resolution X-ray sensor for non destructive evaluation', *IEEE Trans. Nucl. Sci.* **43**(3), 1559–1563.

Nagarkar, V. V., Tipnis, S. V., Shestakova, I., Gaysinskiy, V., Singh, B., Paulus, M. J. & Entine, G. (2004), 'A high speed functional MicroCT detector for small animal studies', *Proceedings of IEEE NSS-MIC Conference* .

Natterer, F. (1986), *The mathematics of computerized tomography*, Tuebner-Wiley, New York.

Ning, R. & Tang, X. (2004), 'X-ray scatter correction algorithm for cone-beam CT imaging', *Med. Phys.* **31**, 1195–1202.

Noo, F., Defrise, M., Clackdoyle, R. & Kudo, H. (2002), 'Image reconstruction from fan-beam projections on less than a short scan', *Phys.Med.Biol.* **47**, 2525–2546.

Noo, F., Pack, J. & Heuscher, D. (2003), 'Exact helical reconstruction using native cone-beam geometries', *Phys. Med. Biol.* **48**, 3787–3818.

Nuyts, J., Man, B. D., Dupont, P., Defrise, M., Suetens, P. & Mortelmans, L. (1998), 'Iterative reconstruction for helical CT: a simulation study', *Phys. Med. Biol.* **43**, 729–737.

Ohnesorge, B., Flohr, T. & Klingenbeck-Regn, K. (1999), 'Efficient object scatter correction algorithm for third and fourth generation ct scanners', *Eur. J. Radiol.* **9**, 563–72.

Patch, S. K. (2002), 'Consistency conditions upon 3D CT data and the wave equation', *Phys. Med. Biol.* **47**, 2637–2650.

Peplow, D. & Verghese, K. (1998), 'Measured molecular coherent scattering form factors of animal tissues, plastics and human breast tissue', *Phys. Med. Biol.* **43**, 2431–2452.

Platten, D., Keat, N., Lewis, M. & Edyvean, S. (2005), 32 to 64 slice CT scanner comparison report version 13, Technical report, NHS Purchasing and Supply Agency and ImPACT.
URL: *http://www.pasa.nhs.uk/evaluation/publications/dier/details.asp?id=1196*

Radon, J. (1917), 'Ueber die Bestimmung von Functionen durch ihre Integralwaerte laengs Gewissen Maenigfaltigkeiten', *Ber. Verk. Saechs. Akad.* **69**, 262–277.

Richardson, W. B. (1972), 'Bayesian-based iterative method of image restoration', *J.Opt.Soc.Am.* **62**, 55–59.

Riess, T., Fuchs, T. & Kalender, W. (2004), 'A new method to identify and to correct circular artifacts in X-ray CT images', *Physica Medica* **XX**(2), 43–57.

Rivers, M. (1998), Tutorial introduction to X-ray computed microtomography data processing, Technical report.
URL: *http://www-fp.mcs.anl.gov/xray-cmt/rivers/tutorial.html*

Rivière, P. J. L. (2005), 'Penalized-likelihood sinogram smoothing for low-dose CT', *Medical Physics* **32**(6), 1676–1683.

Rivière, P. J. L. & Pan, X. (2000), 'Nonparametric regression sinogram smoothing using a roughness-penalized poisson likelihood objective function', *IEEE Trans.Med.Im.* **19**(8), 773–786.

Robbins, M. S. & Hadwen, B. J. (2003), 'The noise performance of electron multiplying charge-coupled devices', *IEEE Trans. Electron. Devices* **50**(5), 1227–1232.

Rosenberg, K. (2002), CTSim - the open source computed tomography simulator, Technical report.
URL: *http://www.ctsim.org*

Ruth, C. & Joseph, P. (1997), 'Estimation of a photon energy spectrum for a computed tomography scanner', *Med. Phys.* **24**(5), 695–702.

Sabo-Napadensky, I. & Amir, O. (2005), 'Reduction of scattering artifact in multi-slice CT', *Proceedings of SPIE* **5745**, 983–991.

Sasov, A. & Dewaele, D. (2002), 'High-Resolution In-Vivo Micro-CT Scanner for Small Animals', *Proc. SPIE* **4503**, 256–264.

Schaller, S. (1999), Abdomen phantom, Technical report.
URL: *http://www.imp.uni-erlangen.de/phantoms/*

Segars, W. P., Tsui, B. M. W., Frey, E. C., Johnson, G. A. & Berr, S. S. (2003), 'Development of a 4D digital mouse phantom for molecular imaging research', *Molecular Imaging and Biology* **5**(3), 126–127.

Shepp, L. A. & Vardi, Y. (1982), 'Maximum likelihood reconstruction for emission tomography', *IEEE Trans.Med.Im.* **1**, 113–122.

Shrimpton, P. C. & Edyvean, S. (1998), 'CT scanner dosimetry', *Bristish Journal of Radiology* **71**, 1–3.

Siddon, R. (1986), 'Fast calculation of the exact radiological path for a three dimensional CT array', *Med. Phys.* **12**, 252–255.

Siewardsen, J. H., Waese, A. M., Moseley, D. J., Richard, S. & Jaffray, D. A. (2004), 'Spektr: A computational tool for x-ray spectral analysis and imaging system optimization', *Medical Physics* **31**(11), 3057–3067.

Siewerdsen, J. H., Moseley, D. J., Burch, S., Bisland, S. K., Bogaards, A., Wilson, B. C. & Jaffray, D. A. (2005), 'Volume CT with a flat-panel detector on a mobile, isocentric C-arm: Pre-clinical investigation in guidance of minimally invasive surgery', *Med. Phys.* **32**(1), 241–254.

Siewerdsen, J. & Jaffray, D. (2000), 'Optimization of X-ray imaging geometry (with specific application to flat-panel cone-beam computed tomography)', *Med. Phys* **27**(8), 1903–1914.

Siewerdsen, J. & Jaffray, D. (2001), 'Cone beam computed tomography with a flat panel imager: Magnitude and effects of X–ray scatter', *Med. Phys.* **28**(2), 220–231.

Sijbers, J. & Postnov, A. (2004), 'Reduction of ring artefacts in high resolution micro-CT reconstructions', *Phys. Med. Biol.* **49**, N247–N253.

Smith, B. D. (1985), 'Image reconstruction from cone-beam projections: Necessary and sufficient conditions and reconstruction methods', *IEEE Trans.Med.Im.* **4**, 14–28.

Snyder, D. L., Miller, M. I., Thomas, L. J. & Politte, D. G. (1987), 'Noise and edge artifacts in Maximum-Likelihood reconstruction for Emission Tomography', *IEEE Trans.Med.Im.* **6**, 228–238.

Spies, L., Ebert, M., Groh, B., Hesse, B. & Bortfeld, T. (2001), 'Correction of scatter in megavoltage cone-beam CT', *Phys. Med. Biol.* **46**, 821–833.

Spyrou, G., Tzanaka, G., Bakas, A. & Panayiotakis, G. (1998), 'Monte Carlo generated mammographs: development and validation', *Phys.Med.Biol.* **43**, 3341–3357.

Taguchi, K. & Aradate, H. (1998), 'Algorithm for image reconstruction in multi-slice helical CT', *Med. Phys.* **25**(4), 550–561.

Tang, X., Hsieh, J., Hagiwara, A., Nilsen, R. A., Thibault, J.-B. & Drapkin, E. (2005), 'A three-dimensional weighted cone beam filtered backprojection (CB-FBp) algorithm for image reconstruction in volumetric CT under a circular source trajectory', *Phys. Med. Biol.* **50**, 3889–3905.

Tang, X., Ning, R., Yu, R. & Conover, D. (2001), 'Cone beam volume CT image artifacts caused by defective cells in X-ray flat panel imagers and the artifact removal using a wavelet-analysis-based algorithm', *Med. Phys.* **28**(5), 812–825.

Thibault, J.-B., Sauer, K., Bouman, C. & Hsieh, J. (2005), 'Three-dimensional statistical modeling for image quality improvements in multi-slice helical CT', *Proceedings of the 8th International Meeting on Fully Three-Dimensional Image Reconstruction in Radiology and Nuclear Medicine* pp. 271–274.

Tuy, H. K. (1983), 'An inversion formula for cone-beam reconstruction', *SIAM J. Appl. Math.* **43**, 546–552.

Wang, G., Crawford, C. R. & Kalender, W. A. (2000), 'Guest editorial: Multirow detector and cone-beam spiral/helical CT', *IEEE Trans.Med.Im.* **19**, 817–821.

Wang, G., Schweiger, G. & Vannier, M. (1998), 'An iterative algorithm for X-ray CT fluoroscopy', *IEEE Trans.Med.Im.* **17**, 853–858.

Webb, S. (1990), *From the watching of the shadows. The origins of radiological tomography*, IOP and Adam Hilger, Bristol, England and New York, USA.

Whiting, B. R. (2002), 'Signal statistics of X-ray computed tomography', *Proceedings SPIE:Med. Im. 2002* pp. 53–60.

Wiegert, J., Bertram, M., Rose, G. & Aach, T. (2005), 'Model based scatter correction for cone-beam computed tomography', *Proceedings of SPIE* **5745**, 271–282.

Wienhard, K., Schmand, M., Casey, M. E., Baker, K., Bao, J., Eriksson, L., Jones, W. F., Knoess, C., Lenox, M., Lercher, M., Luk, P., Michel, C., Reed, J. H., Richerzhagen, N., Trefferta, J., Vollmar, S., Young, J. W., Heiss, W. D. & Nutt, R. (2002), 'The ECAT HRRT: Performance and first clinical application of the new high resolution research tomograph', *IEEE Trans. Nucl. Sci.* **49**(1), 104–110.

Wiesent, K., Barth, K., Navab, N., Durlak, P., Brunner, T., Schuetz, O. & Seissler, W. (2000), 'Enhanced 3-D-reconstruction algorithm for C-Arm systems suitable for interventional procedures', *IEEE Trans.Med.Im.* **19**, 391–404.

Williamson, J. (1987), 'Monte Carlo calculation of kerma at a point', *Med. Phys.* **14**(4), 567–576.

Zbijewski, W. & Beekman, F. J. (2004*a*), 'Characterization and suppression of edge and aliasing artefacts in iterative X-ray CT reconstruction', *Phys. Med. Biol.* **49**(1), 145–157.

Zbijewski, W. & Beekman, F. J. (2004*b*), Fast scatter estimation for cone-beam X-ray CT by combined Monte Carlo tracking and Richardson-Lucy fitting, *in* '2004 NSS-MIC Conference Record'.

Zbijewski, W. & Beekman, F. J. (2004*c*), 'Suppression of intensity transition artifacts in statistical X-ray computer tomography through Radon inversion initialization', *Med. Phys.* **31**(1), 62–69.

Zbijewski, W. & Beekman, F. J. (2006), 'Efficient Monte Carlo based scatter artifact reduction in cone-beam micro-CT', *IEEE Trans.Med.Im., in press* .

Zeng, G. L. & Gullberg, G. T. (1992), 'Frequency domain implementation of the three-dimensional geometric point source correction in SPECT imaging', *IEEE Trans. Nucl. Sci.* **39**(5), 1444–1453.

Zeng, G. L. & Gullberg, G. T. (2000), 'Unmatched projector/backprojector pairs in an iterative reconstruction algorithm', *IEEE Trans. Med. Im.* **19**.

Zhu, L., Strobel, N. & Fahrig, R. (2005), 'X-ray scatter correction for cone-beam CT using moving blocker array', *Proceedings of SPIE* **5745**, 251–258.

Ziegler, A., Heuscher, D., Koehler, T., Nielsen, T., Proksa, R. & Utrup, S. (2004), 'Systematic investigation of the reconstruction of images from transmission tomography using a filtered backprojection and an iterative OSML reconstruction algorithm', *Proceedings of IEEE NSS-MIC Conference* .

Curriculum Vitae

Wojciech Zbijewski was born on December 10th, 1976 in Warsaw, Poland. In 1995, he enrolled the Department of Physics of Warsaw University. During the third year of his studies he spent one semester at the Uppsala University in Sweden. When the time came for selecting the subject of his graduation work, he first opted for theoretical (astro)physics. After a short research project in this area, he realised that he would prefer to stay closer to issues of everyday life and switched to medical physics. He obtained his Master's degree on the Valentine's Day of 2001 with a thesis about the use of Finite Element Method in modelling the electric field of the brain. After his graduation, he had a half-year spell at the Dutch Epilepsy Clinics Foundation in Heemstede, the Netherlands. This was not only where he got his first true experience at a scientific job, but also where he learned about all the niceties of life in Holland. He came back to the Netherlands in April 2002 to pursue a Doctoral degree at the Image Sciences Institute of the University of Utrecht. This thesis summarises four years of research that he has carried out at this institution.

Publications

Articles in international journals:

- Zbijewski, W. & Beekman, F. J. (2004), 'Characterization and suppression of edge and aliasing artefacts in iterative X-ray CT reconstruction', *Phys. Med. Biol.* **49**(1), 145–157.
- Zbijewski, W. & Beekman, F. J. (2004), 'Suppression of intensity transition artefacts in statistical X-ray computer tomography through Radon inversion initialization', *Med. Phys.* **31**(1), 62–69.
- Colijn, A. P., Zbijewski, W., Sasov, A. & Beekman, F. J. (2004), 'Experimental validation of a rapid Monte Carlo based Micro-CT simulator', *Phys.Med.Biol.* **49**(18), 4321–4333.
- Zbijewski, W. & Beekman, F. J. (2006), 'Comparison of methods for suppressing edge and aliasing artefacts in iterative X–ray CT reconstruction', *Phys. Med. Biol.* **51**(7), 1877–1889.
- Zbijewski, W. & Beekman, F. J. (2006), 'Efficient Monte Carlo based scatter artefact reduction in cone-beam micro-CT', *IEEE Trans.Med.Im.*, in press.
- Zbijewski, W., Defrise, M., Viergever, M. A. & Beekman, F. J., 'Statistical reconstruction for X-ray CT systems with non-continuous detectors', submitted.

Acknowledgements

First words of gratitude have to go to all the people who helped me carry out the research described in this thesis. Among all of them, the first one to mention is, of course, my direct supervisor and the person behind this whole project, Freek Beekman. Dear Freek, thanks for pushing me, whenever I needed a push, coming up with ideas whenever I had none, giving me numerous opportunities to present my work internationally and keeping the excitement levels high enough to ensure that I would never feel even slightly bored at work. Finally, many thanks for your willingness to keep me in the group as a post-doc. Hopefully, the next year of our cooperation will be as fruitful (or maybe even more...) as the previous four.

The next person to mention is my promotor, Max Viergever. Although in daily work I relied mostly on Freek's supervision, I greatly appreciated your contributions to my last paper and your careful reading of this thesis' introduction. Moreover, I would like to thank you here for keeping the whole machinery of Image Sciences Institute working so smoothly. I found the atmosphere at ISI very pleasant and stimulating and I think that it was largely due to your excellent management.

During the four years of my PhD research I had an opportunity to see the rapid growth of Freek's Physics of Molecular Imaging and Nuclear Medicine group. Here I would like to thank all the past and present members of our group for the nice time we had together - during lunches, dinners, group meetings, conferences and everyday coffee breaks. I would especially like to mention here Brendan Vastenhouw for his computer support and Tim de Wit for sharing with me the enjoyment (and struggle) of teaching. Special place is reserved for all the post-docs who were involved at some stage in my research project. Auke-Pieter and Sebastiaan, I would like to thank you both not only for all the work we did together, but also for the fact that we remained friends even after you had left the group for other jobs. Mart, many thanks for transforming my English Summary into a Dutch Samenvatting.

Outside the group (but still within the domain of science), I would like to thank Fred Noo for providing us with his FBP reconstruction codes (and some extra explanations), Michel Defrise for his cooperation on my last paper and Johan Nuyts for careful reading of this thesis and many insightful comments. All the member's of the STW steering committee deserve my gratitude for keeping a close eye on our research and making sure that the commercial perspective was never completely lost. I would especially like to thank Michael Grass for sharing with us some essential scanner parameters and answering my numerous technical questions, and Harrie Weinans for allowing us to do some scanning at his laboratory in Rotterdam. Finally, I would like to express my gratitude to the SkyScan people: Alexander Sasov, Xuan Liu, Elke van de Casteele

and Phil Salmon, for their assistance with the measurements that were the basis for a lage part of this thesis, the nice atmosphere that I always experienced while visiting SkyScan, and finally patience in addressing my technical doubts.

Last but not least form the scientific world to be mentioned here is Stiliyan Kalitzin from the Dutch Epilepsy Clinics Foundation. Stiliyan, it was during my stay at SEIN that I learned what it really means to be a scientist. It was also your recommendation that helped me get my PhD position in Utrecht. I think it is the right place to thank you both for the excellent time I had while working with you and for supporting my job application at ISI.

Outside science, the first to mention are my paranymphs, Kinga Sznee and Jianbin Xiao. First of all, I thank you for your willingness to take those supportive roles and join me during my defense. Since you both are also getting closer and closer to the ends of your PhD studies, I wish you lots of luck and very smooth final months of work.

Kinga, to end up doing a PhD in the same country as one of my best university friends was a sort of good luck for me. Another lucky coincidence was that we share the same hobby, slightly out-of-place in the Netherlands: climbing. To make things even better, this country turned out to be small enough to allow for frequent climbing-and-whatever-else events at its numerous indoor gyms. All in all, it was always great fun - but I wanted also to thank you and your family for this one Christmas dinner at the time when not everything looked really bright in my life...

Jianbin, thanks a lot for all the coffee breaks and lunches together at UMC, all the discussions about politics, economy, history, culture, the US and numerous other subjects totally unrelated to our PhD projects. Having you around for all those chats was a great way to relieve the stress of work and clean up my brain circuits from too much medical imaging. Thanks also for serving as my mailbox for a short while!

Two of my friends helped me with the preparation of this thesis: Emma, who did a great job correcting my English, wherever it needed correction, and Aart, who took a second look at the Samenvatting. Thanks a lot!

Now the time comes for all other friends of mine, here in Utrecht and back in Poland. What would be life without you, guys? All those climbing trips, mountain-biking rides, parties, pub meetings, dinners and email exchanges, but also all the support and help I got from you, when I truly needed it - I simply consider myself lucky to have met you on my way through life. Ziemek, Agata, Dorota, Magda, Michał Kacprzak, Michał Król, Monika and Marcin, Marta and Paweł, Michał and Irena, Piotr Pysiak, Krzyś, Wiesiek, Michał Bluj, Gosia Suwińska, Ewa Ziółkowska, Piotr Suffczyński, Reza, Eyk, Maike, Daniel and Sofia, Maggie and Niels, Martijn, Alexiey, Olga, Fernando (and the list is by no means complete): thanks for being around! I can only hope you had as many good moments with me, as I had with you...

I would also like to thank here Elżbieta and Sherwin Wilk for all the care and help I have received from them, especially during the last year, and for the great time I had while visiting them in New York.

The final paragraph of this thesis is reserved for someone very special. Mamuś Najukochańsza, my Dearest Mom, I miss you so much... Saying so is as much of an understatement as saying simply "Thank You" is not enough to truly thank you for all that you have given to me. For all your unconditional love, care, all the trust in my abilities, for giving me the strength to never give up and for making my childhood happy against all odds - my hope is that not only this thesis, but my whole life, will simply make you proud, wherever you are. And I know one place,

where you will always be - my heart…